The Dissertation Committee for Chad Allen Greene
certifies that this is the approved version of the following dissertation:

Drivers of change in East Antarctic ice shelves

Committee:

Donald D. Blankenship, Supervisor

Robert E. Dickinson

Patrick Heimbach

Charles S. Jackson

Clark R. Wilson

Duncan A. Young

Drivers of change in East Antarctic ice shelves

by

Chad Allen Greene

DISSERTATION
Presented to the Faculty of the Graduate School of
The University of Texas at Austin
in Partial Fulfillment
of the Requirements
for the Degree of

DOCTOR OF PHILOSOPHY

THE UNIVERSITY OF TEXAS AT AUSTIN
December 2017

“ ”

– Marcel Marceau

Acknowledgments

This work was supported by NASA grant NNX11AH89G, NSF grants CDI-0941678, PLR-1543452, and PLR-1143843, the University of Texas at Austin's Jackson School of Geosciences, and the G. Unger Vetlesen Foundation. Thanks to Duncan Young for endless patience in answering my many naïve questions. Thanks to David Gwyther for years of engaging scientific discussions and thanks to my friends and colleagues, Marie Cavitte, Gail Muldoon, and Enrica Quartini, for their ongoing help and support throughout this work.

And to my parents, thank you.

Drivers of change in East Antarctic ice shelves

Chad Allen Greene, Ph.D.
The University of Texas at Austin, 2017

Supervisor: Donald D. Blankenship

Antarctica holds enough landlocked ice to raise the global sea level by nearly 60 m in the event of wholesale ice sheet collapse. In East Antarctica, the Aurora Subglacial Basin is drained by Totten Glacier and is one of the world's largest and most rapidly-changing ice catchment systems. In recent decades, Totten Glacier has exhibited variability in its flow rate, mass balance, and ice thickness, each led by changes at the ice sheet margin. Totten Glacier dynamics are linked to processes in the Totten Ice Shelf, which buttresses the flow of grounded ice while being subjected to variable ocean forcing from below. Understanding the stability of the Aurora Subglacial Basin in a changing climate requires an understanding of how Totten Ice Shelf responds to changes in its environment. This dissertation investigates ice shelf processes on spatial scales of 1 km to 100 km, that act on sub-annual to decadal time scales. The independent roles of channelized basal melt and large-scale basal melt resulting from a variable supply of oceanic heat content are examined using surface elevation changes measured by airborne laser altimetry, satellite laser altimetry, and a new method of photometry applied to satellite images.

A new method of satellite image template matching is also developed to understand ice shelf velocity response to several environmental forcing mechanisms. On the interannual time scale, Totten Ice Shelf is seen accelerating in response to nearby upwelling of warm circumpolar deep water that enhances basal melt rates. On the subannual time scale, Totten Ice Shelf exhibits winter slowdown as buttressing from seasonal landfast sea ice at the ice shelf front slows the flow of the glacier. These findings show that the Totten Glacier catchment is sensitive to changes in its environment, and may be susceptible to changes in the coastal wind stress projected for the 21st century.

Table of Contents

List of Tables

List of Figures

Chapter 1

Introduction

A complete collapse of the Antarctic Ice Sheet would raise the global sea level by 58 m (Fretwell et al., 2013), putting many of the world's major cities and vast regions of agricultural lands under water. Such a catastrophic event is unrealistic on the hundred-year timescale, but even centimeter-level changes in sea level are likely to cost billions of dollars for infrastructure adaptations (Hinkel et al., 2014) and have untold human costs (Ericson et al., 2006; Marzeion and Levermann, 2014). Sea level rise is underway and will continue throughout the next hundred years, but uncertainty remains in its rate and magnitude, due primarily to a poor understanding of ice sheet sensitivity to climate change (Stocker et al., 2013; Bamber and Aspinall, 2013). To better constrain projections, this work focuses on the climate sensitivity of the Totten Glacier catchment in East Antarctica, which holds enough ice to raise the global sea level by at least 3.5 m (Greenbaum et al., 2015).

1.1 Ice shelves in Antarctica

The $\sim$2 km thick ice sheet resting on the Antarctic continent is fed by snowfall and continuously spreads toward the sea, driven by gravity as it deforms under its own weight. Where the ice sheet spills into the ocean, sections the size of U.S.

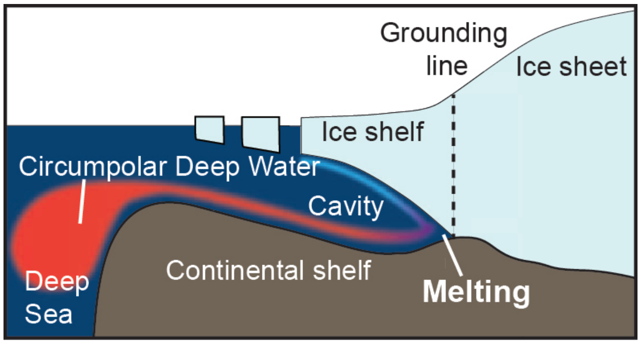

Figure 1.1: Profile diagram of an ice shelf, cavity, and landward-sloping continental shelf that allows warm, dense circumpolar deep water to flow toward the ice shelf base. Source: British Antarctic Survey.

states form ice shelves that go afloat while remaining attached to the grounded ice inland (c.f. Figures 1.1 and 2.2). Most of Antarctica's glaciers terminate in ice shelves, and these large floating features act as plugs in the drain to slow the flow of ice from land to sea. Ice shelves also play a role in coupling the ice sheet to thermal forcing from the ocean (Walker et al., 2009; Joughin et al., 2010, 2012; Hattermann et al., 2012; Pritchard et al., 2012; Rignot et al., 2013; Depoorter et al., 2013; Holland et al., 2008b; Jacobs et al., 2011). With a primary focus on Totten Glacier, this work is aimed at understanding how ice shelves respond to oceanic and other forcing mechanisms.

1.1.1 Ice shelf buttressing

Antarctic ice shelves lose mass partly by calving icebergs into the ocean, but a majority of ice shelf mass is lost through ocean-driven melting from below (Rignot et al., 2013; Depoorter et al., 2013). When basal melt thins an ice shelf sufficiently to affect is ability to buttress the seaward flow of ice, the ice shelf speeds up, and the thinning and acceleration can propagate inland (Scambos et al., 2004; Dupont and Alley, 2005, 2006; Felikson et al., 2017). Where inland ice is grounded below sea level, such as in the Aurora Subglacial Basin, which is drained by Totten Glacier (Young et al., 2011), glacier thinning can lead to large-scale destabilization of the ice basin (Weertman, 1974; Schoof, 2007). Thus, understanding the basal mass balance of ice shelves is of critical importance for understanding the stability of the Antarctic Ice Sheet.

1.1.2 The ice pump mechanism

Figure 1.1 shows a profile of a typical landward-sloping continental shelf that has deformed under the weight of the Antarctic Ice Sheet. Melt is often concentrated near the deep grounding line[1], where the in situ melting temperature of ice is suppressed below -3°C due to the overlying pressure of $\sim$2000 m of seawater (McDougall and Barker, 2011). At the grounding line, the ice sheet loses basal traction and quickly spreads and thins, resulting in a basal elevation profile that has a characteristic exponential decay as seen in Figure 1.1. Steep basal slopes near the grounding line allow buoyant, fresh meltwater to rise along the ice shelf base, and the rising plume of water has an effect of further increasing basal melt by contributing convective heat transfer to the process. Concentrated melt at the deep grounding line and the rising plume of meltwater are the first steps in a cycle known as the ice

---

[1] The grounding line represents a boundary between ice resting on bedrock and ice floating as an ice shelf. In some cases, this thesis uses the generalized term *grounding zone*, referring to the hinge-like area between the seawardmost line along which ice exhibits no effects of tidal flexure to the landwardmost line along which the ice shelf is in hydrostatic equilibrium.

pump (Lewis and Perkin, 1986; Jenkins and Doake, 1991).

Latter steps of the ice pump cycle vary depending on the temperature, salinity, and pressure regime of the ice shelf cavity. The cold cavities of the Ross Ice Shelf and Amery Ice Shelf favor accretion of basal marine ice near their ice fronts, where, after rising to shallow depths, cold, fresh meltwater can refreeze due to reduced hydrostatic presssure (Neal, 1979; Fricker et al., 2001). Warmer cavities such as the ice shelves of the Amundsen Sea in West Antarctica are unlikely to support large-scale refreezing (Rignot et al., 2013). In warm cavities, rising plume water may follow the ice shelf base fully to the glacier terminus and can create regions of open water (polynyas) where sea ice would otherwise be present (Mankoff et al., 2012). Alternatively, rising plume water may follow the ice shelf base until reaching a density equilibrium, at which point the meltwater detrains mid-depth in the water column and cannot be detected from the ocean surface. By focusing melt near the grounding line and in some cases redistributing ice closer to the ice front, the ice pump mechanism has a complex influence on the structural stability and longevity of ice shelves.

1.1.3 Ice shelf fracture

A changing ice shelf can affect the flow of the grounded ice it restrains either by broad-scale thinning (or thickening) and associated small changes in buttressing, or by wholesale fracture or disintegration of the ice shelf. Large-scale disintegration events have been observed around the Antarctic Peninsula and have been attributed to hydrofracture from surface water that accumulates in response to atmospheric warming (Doake and Vaughan, 1991; Scambos et al., 2009; Banwell et al., 2013). Ice tongues are vulnerable to other processes. In 2010, Mertz Glacier Tongue lost half its length as a result of shear-induced fracture from interaction with the sea bed and collisions with passing icebergs (Massom et al., 2015). A similar-sized calving event occurred at Drygalski Ice Tongue in ca. 1957, which is suspected to have resulted from a violent winter storm (Frezzotti and Mabin, 1994) that propagated bottom crevasses to the point of failure.

Ice shelf fractures tend to initiate where stress is concentrated and where ice is thinner than its surroundings. For example, Vaughan et al. (2012) found that bottom crevasses in Pine Island Ice Shelf initiate at the centers of basal channels (see Chapter 3) and surface crevasses align over keels between basal crevasses. Ice shelf crevasses can extend hundreds of meters through an ice shelf and have a significant effect on the overall stability of an ice shelf (Hughes, 1983). Notably, it has been found that the ice pump mechanism described above can operate within the confines of a deep basal crevasse and can have the effect of structurally repairing the ice shelf (Khazendar and Jenkins, 2003). Mechanisms for crevasse formation and the effects that crevasses may have on the structural integrity of an ice shelf vary, but their presence must be considered in assessments of ice shelf stability.

1.2 Totten Ice Shelf

Totten Glacier is located along the Sabrina Coast in East Antarctica at (67°S,116°E) (Fig 1.2). It drains a 550,000 km^2 region (Mouginot et al., 2016) of the Aurora Subglacial Basin, is grounded primarily below sea level (Young et al.,

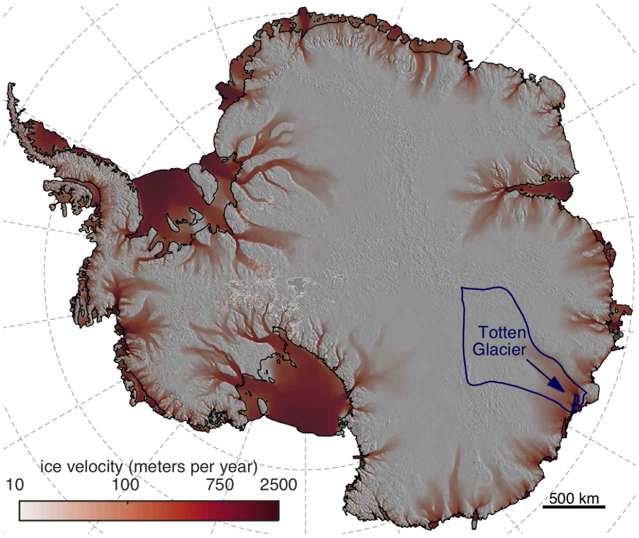

Figure 1.2: Totten Glacier drains a 550,000 km^2 region of grounded ice that has a mean thickness of 3240 m. The IMBIE refined ice basin outline of the Totten catchment from Mouginot et al. (2016) is shown in dark blue. Surface velocities are from Rignot et al. (2011c) version 2. The background image is from the MODIS Mosaic of Antarctica (Haran et al., 2014b).

2011), and holds enough ice to raise global sea level by at least 3.5 m (Greenbaum et al., 2015). Just south of Law Dome, Totten Glacier goes afloat to form a ∼140 km long, 6200 km^2 ice shelf that has exhibited considerable interannual variability in recent decades (Paolo et al., 2015; Li et al., 2016; Roberts et al., 2017).

1.2.1 Circumpolar deep water

The water column thickness beneath Totten Ice Shelf is known from airborne surveys which have measured ice thickness using ice-penetrating radar and the underlying seafloor bathymetry has been estimated from airborne gravimeter data. Gravity inversion does not provide a direct measurement of seafloor topography and estimates are inherently spatially lowpass filtered, but the available gravimetry has been sufficient to resolve deep submarine troughs leading into the Totten Ice Shelf cavity (Greenbaum et al., 2015). Due to ocean dynamics in a rotating Earth, continental shelf bathymetry can be critical in throttling water circulation into an ice shelf cavity (Kämpf, 2005; Klinck and Dinniman; St-Laurent et al., 2013), so until a 2015 shipborne survey it was unclear what water masses have the ability to reach the Totten Ice Shelf front. In that survey, a stratified water column was observed in the troughs close to the ice shelf front, containing warm modified circumpolar deep water (MCDW) at depths below ∼600 m (Rintoul et al., 2016). The MCDW found at the Totten Ice Shelf front likely has a significant impact on basal melt rates, as it exceeds the local freezing point at the grounding line by 3.2°C.

Circumpolar Deep Water is sourced in the deep ocean beyond the continental shelf break, and it is a warm, salty blend of water masses including North Atlantic Deep Water and Antarctic Bottom Water. It has been detected on the continental shelf break near the Sabrina Coast (Wakatsuchi et al., 1994; Bindoff et al., 2000; Williams et al., 2011) and on the continental shelf near Totten Ice Shelf (Silvano et al., 2017) but its delivery mechanisms and pathways to the Totten Ice Shelf front have not been well understood. Chapter 6 describes wind-driven upwelling as a cause of variability in the supply of MCDW to the Totten Ice Shelf cavity.

1.2.2 Polynyas

Antarctica is fringed by a seasonally varying halo of sea ice, which forms directly from freezing the ocean's surface waters, and the presence or absence of sea ice has been linked to ice shelf stability. Recent work has brought attention to polynyas for their role in sub-ice-shelf circulation and their possible link to ice shelf basal melt (Galton-Fenzi et al., 2012; Mankoff et al., 2012; Gwyther et al., 2014; Khazendar et al., 2013). From a Russian term for "ice hole", polynyas are locations of recurring open water within sea ice that can exceed 100,000 km^2 in area, and can result from focused outflow of subglacial meltwater (Motyka et al., 2011; Alley et al., 2016) or by topographically-focused katabatic winds (Massom et al., 1998; Williams et al., 2007; Barber and Massom, 2007). Where cold winds scour the surface of the coastal ocean, heat is lost to the atmosphere and sea ice production increases. Newly-formed sea ice is exported northward by the strong winds, while the dense, briny, cooled seawater rejected in the ice formation process sinks to the seafloor. This dense water may spill over the continental shelf to form Antarctic Bottom Water or it may flow down a landward-sloping continental shelf toward nearby ice shelf grounding lines. Ice-ocean-atmosphere modeling simulations suggest that increased activity of the Dalton polynya (66°S,120°E) could produce enough cold, dense water to displace MCDW and have a significant impact on the basal melt rate of Totten Ice Shelf (Gwyther et al., 2014; Khazendar et al., 2013); however, oceanographic observations within the polynya have not confirmed high rates of cold, dense water production (Silvano et al., 2017).

1.2.3 Seasonal effects

Sub-annual variability in dynamics of Totten Ice Shelf is not well understood. Short-term increases or decreases in ice discharge may result from variations in driving stress linked to seasonal snow accumulation and/or ablation; the seasonal cycle of firn compaction as snow solidifies into ice (Munneke et al., 2014); or ice shelf weakening due to effects of percolating surface melt (Doake and Vaughan, 1991). Chapter 6 of this thesis links longer timescales of ice shelf thinning to loss of lateral shear stress and subsequent acceleration in Totten Ice Shelf, but this process has not been seen on subannual timescales. Chapter 5 discusses the possible role of seasonal rigid landfast sea ice in contributing to Totten Ice Shelf velocity variability by providing temporary buttressing over the winter months.

1.3 Wind-driven ocean circulation

Ocean circulation near the Sabrina Coast is characterized by two primary wind-driven systems. North of the continental shelf break, strong eastward winds drive the eastward-flowing Antarctic Circumpolar Current (ACC; Orsi et al., 1995). Along the continental shelf break and close to the coast, westward winds drive the westward-flowing Antarctic Coastal Current[2] (ACoC). The impacts of the interplay of these two wind-driven systems is the focus of Chapter 6 of this thesis.

1.3.1 Southern Annular Mode

The Southern Annular Mode (SAM) is a climate index which can be defined as a difference in normalized mean zonal pressure between 40°S and 65°S (Marshall, 2003). This simple metric describes the primary driver of climate variability in the southern hemisphere, where the SAM accounts for about 35% of climate variability (Marshall, 2007). Most notably, a high SAM index is associated with an intensification and southward migration of the westerly surface winds which drive the ACC (McLandress et al., 2011). This intensification pushes surface waters northward through Ekman transport[3], resulting in compensatory upwelling of warm CDW south of the ACC (Hall and Visbeck, 2002; Thompson et al., 2011). A high SAM index is associated with weakened easterly winds close to the East Antarctic coast, and thus a weakening of the ACoC (Heil et al., 2009; Mathiot et al., 2011). When strong, the ACoC depresses isopycnals (surfaces of constant potential density) and thereby acts as a dynamic barrier to the influx of CDW onto

---

[2] Deacon (1937) identified an *East Wind Drift* as the wind-driven westward flow along the coast of Antarctica. This current has more recently been termed the *Antarctic Slope Current* (ASC), which is often indistinguishable from the ACoC due to coincidence (Mathiot et al., 2011). Following Årthun et al. (2012), this thesis refers to the ASC/ACoC system collectively as the ACoC.

[3] Ekman (1905) described an effect of Earth's rotation whereby the net transport of surface water is 90° to the left of surface wind direction in the southern hemisphere.

the continental shelf (Jacobs, 1991; Núñez-Riboni and Fahrbach, 2009; Wang et al., 2012; Årthun et al., 2012; Hayakawa et al., 2012), whereas an ACoC weakened by a sustained high-index SAM could lead to a relaxation of this effect. In short, a sustained high-index SAM could enhance delivery of CDW onto the continental shelf through a combination of upwelling (Ekman pumping) and simultaneous relaxation of the dynamic barrier along the continental slope.

In recent decades, the SAM has trended toward high values in the spring and early summer due to a depletion of stratospheric ozone over Antarctica (Thompson et al., 2011). As a result of a global reduction in use of ozone-depleting substances, the spring and summer bias has already begun to wane; however, greenhouse gases are expected to bias the SAM to record highs by the middle of this century (Thompson et al., 2000; Arblaster and Meehl, 2006; Fyfe et al., 2007; McLandress et al., 2011; Sigmond et al., 2011). The SAM is likely to trend positive throughout the coming century, so understanding how the SAM affects the Southern Ocean, and understanding how these oceanographic changes may propagate to Antarctica's floating ice shelves are essential steps toward accurate projections of Antarctica's grounded ice response to changes in atmospheric greenhouse gas.

In the Amundsen Sea region of Antarctica, it has been suggested that the SAM is positively correlated with upwelling of relatively warm, dense CDW onto the continental shelf (Jacobs, 2006). Nearby in the eastern sector of Getz Ice Shelf, however, no such link was found between the SAM and CDW layer thickness (Jacobs et al., 2013). In the neighboring trough leading to Pine Island Embayment, Assmann et al. (2013) found intrusions of unmodified CDW were driven by zonal wind stress, and these winds have been linked to tropical forcing (Steig et al., 2012; Dutrieux et al., 2014). Melt variability may be driven by changes in CDW delivery resulting from a fluctuating SAM, by changes in polynya activity linked to local meridional winds, or by redirection of coastal currents driven by longer-term changes in oceanic wind stress (Hellmer et al., 2012; Timmermann and Hellmer, 2013). The common thread among these mechanisms is the wind that drives them, and this work seeks to elucidate the link between changing wind fields and changing ice shelf dynamics.

1.4 Structure of the dissertation

This dissertation is organized into a series of separate investigations, the results of which have been published, are in review, or are in preparation for publication in peer-reviewed journals.

The focus of this dissertation is on the interplay of environmental forces acting on a wide range of spatial and temporal scales. Understanding how such processes work together first required the development of a standard computational framework for pairing modeled and observed geospatial data collected by various shipborne, airborne, and satellite platforms. Chapter 2 describes Antarctic Mapping Tools for MATLAB (Greene et al., 2017b), which is a toolbox for analyzing, comparing, exploring, and displaying Antarctic geospatial data. The toolbox has gained widespread use among the polar research community and the paper describing it, published in the journal *Computers and Geosciences*, is presented in Chapter 2.

Chapter 3 describes ice shelf basal channels, how they form, and their role in the stability of ice shelves. It includes a review of literature on basal channels and my contribution to a paper titled “Basal channels drive active surface hydrology and transverse ice-shelf fracture,” which is currently in review (Dow et al., in review).

Given the importance of basal channels to the stability of ice shelves, detecting small-scale surface elevation changes linked to channelized basal melt is a critical part of understanding ice sheet dynamics and Antarctica’s sensitivity to environmental changes. Chapter 4 uses the computational tools developed for Antarctic Mapping Tools and borrows some of the DEM (digital elevation model) development techniques described in Chapter 3 to develop a new method of satellite image analysis for detecting small-scale surface elevation change. The new method of repeat photoclinometry finds signals of channelized surface elevation change by taking advantage of hundreds of satellite images that have until now been considered of insufficient resolution or quality for scientific use. The paper presented in Chapter 4 titled “A method of repeat photoclinometry for detecting kilometer-scale ice sheet surface evolution” has been accepted to the journal *IEEE Transactions on Geoscience and Remote Sensing* (Greene and Blankenship, in press).

Chapter 5 continues analysis of the MODIS satellite image dataset described in Chapter 4, but focuses on short-term velocity variability of the Totten Ice Shelf. As in Chapter 4, this work makes use of the long record and superior temporal resolution of the MODIS image dataset to develop a subannual surface velocity record assessed by feature tracking applied to hundreds of image pairs. Springtime acceleration is observed within 50 km of the glacier terminus, and is attributable to breakup of landfast sea ice at the ice shelf front. Chapter 5 is in preparation for publication in a peer-reviewed journal.

This dissertation has been primarily motivated by a need to understand the Antarctic Ice Sheet's sensitivity to a changing climate. Chapter 6 of this thesis presents a paper titled "Wind causes Totten Ice Shelf melt and acceleration" (Greene et al., 2017a), which finds interannual variability of Totten Ice Shelf linked to wind-driven upwelling of warm water from the deep ocean north of the continental shelf break. Velocity variability is assessed using techniques of MODIS image analysis developed in Chapters 4 and 5. The paper presented in Chapter 6 has been accepted to the journal *Science Advances*.

Concluding remarks and directions of future work are provided in Chapter 7.

Chapter 2

Antarctic Mapping Tools for MATLAB

This chapter describes Antarctic Mapping Tools package, an open-source MATLAB toolbox for analysis and plotting of Antarctic geospatial datasets. This toolbox is designed to streamline scientific workflow and maximize repeatability through functions which allow fully scripted data analysis and mapping. Data access is facilitated by several dataset-specific plugins which are freely available online. An open architecture has been chosen to encourage users to develop and share plugins for future Antarctic geospatial datasets. This toolbox includes functions for coordinate transformations, flight line or ship track analysis, and data mapping in georeferenced or projected coordinates. Each function is thoroughly documented with clear descriptions of function syntax alongside examples of data analysis or display using Antarctic geospatial data. The Antarctic Mapping Tools package is designed for ease of use and allows users to perform each step of data processing including raw data import, data analysis, and creation of publication-quality maps,

---

The contents of this chapter have been published as C. A. Greene, D. E. Gwyther, and D. D. Blankenship. Antarctic Mapping Tools for MATLAB. *Computers & Geosciences*, 104:151–157, 2017b. doi: 10.1016/j.cageo.2016.08.003. URL `http://www.sciencedirect.com/science/article/pii/S0098300416302163`. The work presented here was conceived of and carried out primarily by the author of this dissertation.

wholly within the numerical environment of MATLAB.

2.1 The need for development of AMT

MATLAB is a powerful numerical analysis program which is widely used in the Antarctic research community, but its mapmaking capabilities are rarely exercised due to lack of accessibility and a common perception that MATLAB cannot produce high-quality graphics. MATLAB offers an add-on Mapping Toolbox, but it lacks many of the mapping capabilities and functions necessary for common Antarctic geospatial analyses. Mapping programs such as ArcMap and Generic Mapping Tools (GMT, Wessel and Smith (1991); Wessel et al. (2013)) excel at the task of generating high-quality graphical displays of geospatial data, but their numerical analysis capabilities are limited and difficult to access. Recent development of the Quantarctica mapping program (www.quantarctica.org) has addressed a need for user-friendly Antarctic mapping software, but most users continue to rely on separate programs such as MATLAB for numerical analysis. Thus, a workflow gap exists between data analysis and data display. This gap introduces room for error in transferring data between programs and reduces scientific repeatability by increasing the number of manual steps users must take to present their data. In this paper we present the Antarctic Mapping Tools (AMT) package for MATLAB, designed for a streamlined workflow, ease of use, production-quality graphics, thorough documentation, and expandability through new plugins.

Geospatial data analysis and mapmaking in MATLAB are hindered by a shortage of intuitive, useful data analysis tools, by an absence of many common mapping features, and by the difficulty users experience when attempting to import and properly georeference public datasets found in myriad formats. MATLAB lacks essential mapping features such as the ability to simply zoom a map to a region of interest, or the ability to create inset maps for geospatial context. Seemingly trivial tasks such as the placement of a graticule or graphical reference scale using inbuilt functions involves multiple convoluted and time-consuming steps. Problems associated with map generation in MATLAB are particularly acute for maps of Antarctica because inbuilt coordinate transformation libraries do not readily support the standard southern hemisphere polar stereographic projection. MATLAB's inbuilt documentation offers little guidance to users who wish to use Mapping Toolbox functions for geospatial data analysis, and documented examples of data mapping are not readily adaptable to polar datasets. Moreover, most publicly-available polar datasets provide little guidance to users who wish to import data into MATLAB. AMT fills MATLAB's usability gaps with a set of well-documented functions tailored for analysis and display of Antarctic geospatial data. AMT consists of a set of core data analysis and mapmaking functions and utility of the toolbox is extended by data-specific plugins which are developed to handle data import on a per-dataset basis.

The intent of AMT is to streamline the scientific process by letting simple, intuitive commands perform common types of Antarctic data analysis and mapping. AMT is designed to reduce peripheral analytical steps, increase readability of code, increase scientific clarity of thought, enable fully repeatable scientific analysis, and encourage user development of new data-specific plugins as datasets are released.

This paper provides an overview of the AMT architecture, a summary of AMT core functions, and a description of plugins currently available for AMT.

2.2 AMT architecture

The AMT package is an open-architecture collection of MATLAB functions designed to enable simple, computationally-efficient, repeatable analysis of common Antarctic glaciology, oceanography, and climatology datasets. Data analysis and plotting functions in the AMT package are generic by nature, allowing them to be employed by a wide array of dataset-specific plugins. Coordinate transformation functions allow seamless transitions between georeferenced and projected coordinates. A `crossovers` function is also included in AMT to assist in analysis of data collected along intersecting ship-, satellite-, airborne-, or ground tracks.

2.2.1 Coordinate transformations

Data analysis tools in the AMT package include coordinate transformation functions, an arbitrary path distance calculator, feature location database lookup functions, and a robust, computationally-efficient path crossover location solver. Functions described in this section are summarized in Table 2.1. In keeping with the design philosophy of the AMT package, data analysis functions require minimal inputs, yet allow a variety of optional inputs to increase flexibility of the functions. An example of the easy-to-use nature of AMT is seen in the coordinate transform functions `ll2ps` and `ps2ll`, which convert between georeferenced coordinates and polar stereographic coordinates. By default, `ll2ps` and `ps2ll` use the formula

Function name	Description
`ll2ps`	converts geographic coordinates to polar stereographic meters
`ps2ll`	converts polar stereographic meters to geographic coordinates
`uv2vxvy`	converts zonal and meridional vector components to polar stereographic vector components
`vxvy2uv`	converts polar stereographic vector components to zonal and meridional vector components
`wgs2gl04c`	converts elevations from WGS84 to EIGEN-GL04C geoid reference (Förste et al., 2008)
`gl04c2wgs`	converts elevations from EIGEN-GL04C geoid reference to WGS84 ellipsoid reference
`psgrid`	returns gridded coordinates in equal polar stereographic spacing
`inpsquad`	returns `true` for points within a polar stereographic quadrangle
`pathdist`	returns cumulative distance traveled along a track
`pathcrossingsps71`	finds intersections of two separate tracks
`crossovers`	finds self intersections and interpolates values at crossovers
`islatlon`	input parsing function returns `true` for likely geographic coordinates
`scarloc`	returns coordinates of features identified in the SCAR database

Table 2.1: AMT's core functions provide coordinate transformations, lookup functions, and simple tools for geospatial data analysis.

given by Snyder (1987) for coordinate transformation with the IceBridge (Center, 2015) and Scientific Committee on Antarctic Research (SCAR; SCAR Secretariat, 1992, updated 2015) standard 71°S as the latitude of true scale and the prime meridian in the grid north location. To convert georeferenced coordinates to polar stereographic eastings (`x`) and northings (`y`) in meters using default settings, syntax is simply

```
[x,y] = ll2ps(lat,lon);
```

where `lat` and `lon` can be any point, line, grid, or *N*-dimensional arrays of equal-size georeferenced coordinates. For non-standard polar stereographic coordinate transformations of user-specified Earth radius, eccentricity, meridian longitude, or latitude of true scale, optional input arguments may be included in the `ll2ps` and `ps2ll` function calls as property name-value pairs. For example, to transform georeferenced coordinates to polar stereographic coordinates with 70°S as the latitude of true scale and 45°E as the meridian longitude, syntax is

```
[x,y] = ll2ps(lat,lon,'TrueLat',-70,'Meridian',45).
```

2.2.2 Crossover analysis

Crossover analysis is a technique in which geophysical measurements collected from a moving platform are compared at the intersections of survey tracks. In Antarctica, crossover methods have been applied to a variety of altimetry and potential field measurements collected from several types of moving platforms (e.g., Spikes et al. (2003); Davis and Ferguson (2004); Young et al. (2015); Diehl et al. (2008); Catalán et al. (2006); Shuman et al. (2006); Holt et al. (2006); Muñoz Martín et al. (2005)). For each of the two tracks which constitute a crossover, measurements are one-dimensionally interpolated to the location of intersection. If the elapsed time between two intersecting tracks is small relative to the natural rate of change of the physical quantity under investigation, the difference between measurements at the crossover location may be used to assess measurement precision. If time separating two intersecting tracks is large, measured differences at the crossover location may be taken as measure of change in the physical quantity under investigation.

The mathematics of crossover analysis are not complex, but manual implementations can be time intensive for large datasets and scripted implementations are difficult to write in a generalized, robust, computationally-efficient manner. Whether solutions are automated or calculated manually per intersection, the task of finding crossover locations, interpolating, and winnowing results based on criteria such as interpolation distance or temporal separations can become an unwieldy exercise in bookkeeping. AMT offers a `crossovers` function which lets users enter a simple array of measurements and returns intersection locations along with interpolated values for both legs of each intersection. The user may specify a preferred interpolation method, maximum interpolation distance, and minimum or maximum temporal separation between intersecting tracks. To find intersection locations, `crossovers` takes advantage of MATLAB's left divide operator to solve the system of equations which describes endpoints and intersections of each line-segment pair. For very large datasets which may overload the memory of some workstations, `crossovers` splits the domain into tiles, solves for the intersections within each tile, and then combines solutions from all tiles into a final solution for the full domain.

2.2.3 Data mapping tools

Table 2.2 lists AMT functions which have been developed to support plotting with or without MATLAB's Mapping Toolbox. When using only the functions provided in MATLAB's Mapping Toolbox, simply initializing a standard-orientation map of the southern hemisphere is an unintuitive, multi-step process. AMT solves this problem with the `antmap` function, which initializes a georeferenced south polar stereographic projection map and places the prime meridian oriented at the standard twelve o'clock position. Nonstandard orientations may be achieved manually by setting desired rotation with MATLAB's `view` command.

To plot georeferenced data without MATLAB's Mapping Toolbox or to pair data with other datasets plotted in polar stereographic eastings and northings, AMT provides `plotps`, `pcolorps`, `surfps`, `plot3ps`, `patchps`, `scatterps`, `contourps`, and `textps`. Plotting functions with the `ps` suffix are equivalent to their corresponding standard MATLAB plotting functions, but perform coordinate transformations before plotting in Cartesian coordinates. For example,

```
plotps(lat,lon,'rp')
```

places red pentagrams at the georeferenced locations given by `lat,lon` on Cartesian axes after polar stereographic coordinate transformation. The `plotps` call

Function name	Description
`antmap`†	initializes an Antarctic map and can be used to create a graticule
`mapzoom`†	calls `antmap`, zooms a map to any location identified by its name or coordinates, and can be used to create inset maps
`scalebar`†	places a graphical reference scale on a map
`quivermc`†	depicts color-scaled vector fields on a map
`scarclick`†	returns SCAR-identified feature names by clicking on a map
`scarlabel`	labels features identified in the SCAR database
`shadem`	applies topographic relief shading to maps
`coord`	returns geographic or polar stereographic coordinates from mouse clicks on any map
`mapzoomps`	zooms a polar stereographic map to any location identified by name or coordinates, and creates inset maps
`plotps`	mimics MATLAB's `plot` but with transformation from geographic to polar stereographic coordinates
`plot3ps`	mimics MATLAB's `plot3` but with transformation from geographic to polar stereographic coordinates
`pcolorps`	mimics MATLAB's `pcolor` but with transformation from geographic to polar stereographic coordinates
`surfps`	mimics MATLAB's `surf` but with transformation from geographic to polar stereographic coordinates
`patchps`	mimics MATLAB's `patch` but with transformation from geographic to polar stereographic coordinates
`scatterps`	mimics MATLAB's `scatter` but with transformation from geographic to polar stereographic coordinates
`contourps`	mimics MATLAB's `contour` but with transformation from geographic to polar stereographic coordinates
`textps`	mimics MATLAB's `text` but with transformation from geographic to polar stereographic coordinates
`graticuleps`	places a georeferenced grid or graticule on a polar stereographic Cartesian grid
`scalebarps`	places a graphical reference scale on a polar stereographic Cartesian plot

Table 2.2: AMT provides functions for mapping with or without MATLAB's Mapping Toolbox. Functions which require MATLAB's Mapping Toolbox are denoted with a dagger (†).

above is equivalent to

```
[x,y] = ll2ps(lat,lon);
plot(x,y,'rp').
```

To plot georeferenced data in a nonstandard polar stereographic projection, simply pair the `ll2ps` function with any standard MATLAB plotting function.

To plot vector fields such as wind, ocean currents, or ice flow in georeferenced coordinates, AMT offers `quivermc`. MATLAB's `quiverm` function produces erroneous vector scaling in such a manner that a uniform velocity field is represented by arrows which shrink to zero length near the poles. The AMT function `quivermc` produces appropriately-sized arrows and also offers color scaling, reference size arrows, and automatic field densification or thinning for legibility.

AMT is intended to allow users to easily plot data in a proper geospatial reference frame and in context of complementary geospatial datasets. To help contextualize data, `mapzoom` centers maps of user-specified width on any location. Locations may be given by georeferenced coordinates, or by any of the more than 25,000 feature names listed in the SCAR database (SCAR Secretariat, 1992, updated 2015). A `mapzoom` function allows customizable map insets for spatial reference. To refine the appearance of maps and further provide context, `scarlabel` may be used to label any feature listed in the SCAR database. The `scalebar` function places a simple, customizable graphical reference scale on maps, and the `shadem` applies topographic relief shading.

2.2.4 Documentation

AMT has been developed with a focus on thorough documentation. Each function header contains descriptions of syntax and examples of usage. A function header may be viewed within the MATLAB environment by opening the function or by typing `help` followed by the function name in the command window. Expanded documentation with step-by-step tutorials and inline figures is provided for each function as a formatted HTML file and can be viewed online or by typing `showdemo` followed by the function name and `_documentation`, e.g.,

```
showdemo plotps_documentation.
```

Similarly, a list of core functions and plugins with links to formatted documentation may be viewed by typing

```
showdemo List_of_Functions
```

into the `Matlab` command window.

2.3 Plugins

The open architecture of AMT is designed to encourage user development and sharing of data-specific plugins. Plugins are intended to enable direct comparison of various datasets and multilayered data plotting. Several plugins have been developed to facilitate data access and allow easy plotting of various data types including digital elevation models, satellite images, grounding zone structures, sea ice concentrations, and hydrographic data. Most plugins include automated data download and installation. A selection of plugins currently available is given in Table 2.3.

2.3.1 Data access and interpolation functions

Importing various geospatial products and data types into MATLAB can often be a time-consuming and difficult task. TIFF, GeoTIFF, GeoJP2, shapefiles, HDF, NetCDF, GRD, binary files, and specially-formatted text data files each present their own unique challenges when importing into MATLAB. Data import is further complicated by the host of georeferencing and gridding algorithms currently in use by various data providers. Minor issues such as whether a raster dataset is referenced to pixel centers or pixel corners can cause errors, and quite often users are given no method to verify whether they have properly georeferenced a dataset. As part of the design of AMT, data import and georeferencing issues are addressed per dataset by thoroughly-tested plugin functions designed to efficiently operate on each native data type. To date, plugins have been designed to facilitate access to bed elevation, surface elevation, and ice thickness data from Bedmap2; ice velocity components from MEaSUREs; bed elevations from International Bathymetric Chart of the Southern Ocean (IBCSO); station data and gridded hydrographic data from the Southern Ocean Database; and near-real-time daily sea ice concentration grids.

For gridded datasets, source data may be accessed as raw gridded data with corresponding latitude and longitude grids or polar stereographic easting and northing grids. Alternatively, values may be interpolated to an arbitrary point, ar-

Plugin	Data types	References
Bamber et al. DEM	1 km raster surface elevation DEM	Bamber et al. (2009)
Bedmap2 Toolbox	1 km raster DEMs & masks, inferred grounding line & coastline polygons	Fretwell et al. (2013)
CryoSat-2 DEM	1 km raster DEM and uncertainty	Helm et al. (2014)
IBCSO Toolbox	500 m raster bathymetric DEM	Arndt et al. (2013)
MEaSUREs	450 m InSAR-derived raster ice velocity & vector landward limits of flexure	Rignot et al. (2011b,c,d,a)
RAMP	200 m Radarsat image mosaic	Liu et al. (2001)
LIMA	15 m true color raster satellite image mosaic	Bindschadler et al. (2008)
MODIS MOA	125 m raster satellite image mosaic, break-in-slope & coastline polygons	Scambos et al. (2007)
ASAID	15 m resolution break-in-slope and hydrostatic line polygons	Bindschadler et al. (2011a)
ICESat grounding zone	ICESat-derived break-in-slope, & limits of flexure	Brunt et al. (2010, 2011)
ICESat active lakes	ICESat-derived active subglacial lake polygons	Smith et al. (2009, 2012)
Basins	ICESat-derived ice drainage system boundaries	Zwally et al.
Sea ice concentration	25 km raster SMMR, SSM/I, & SSMIS-derived daily sea ice concentrations	Cavalieri et al. (1996)
SODB	24 km raster gridded Southern Ocean Database hydrographic & station locations	Orsi and Whitworth (1998)
ACC fronts	Antarctic Circumpolar Current front polygons	Orsi et al. (1995)
Post-glacial rebound	1 degree raster glacial isostatic adjustment model data	A et al. (2013)
Antarctic gravity	10 km raster free-air and Bouguer anomalies	Scheinert et al. (2016)
Geothermal heat flux	5 km raster satellite-derived heat flux from magnetism	Maule et al. (2005)

Table 2.3: A selection of plugins currently available for AMT. Plugins are developed per dataset to provide plotting capabilities and easy access to raw or interpolated data.

ray, or grid. Function names for raw data access take the form `bedmap2_data`, `ibcso_data`, etc., and these functions allow partial loading of large datasets, which can be downsized by resolution or by regional data loading. Function names for data interpolation take the form `bedmap2_interp`, `ibcso_interp`, etc., and interpolation methods may be specified by the user. A simple method of comparing two datasets of differing resolution or grids is to interpolate values of one dataset to the grid of another. For example, the Bedmap2 bed elevation dataset may be compared to the IBCSO DEM by interpolating the IBCSO DEM to the Bedmap2 grid. This can be accomplished in two steps—First, Bedmap2 bed elevation data are loaded with corresponding geographic coordinates of each pixel center, then IBCSO data are interpolated to the Bedmap2 grid:

```
[lat,lon,z_bedmap2] = bedmap2_data('bed','res','5 km');
z_ibcso = ibcso_interp(lat,lon);
```

With `z_bedmap2` and `z_ibcso` the two datasets may then be compared by simple subtraction or histogram, as shown in Figure 2.1.

2.3.2 Data plotting functions

All of the AMT plugins listed in Table 2.3 offer simple data plotting commands. For example, calling `modismoa`, `lima`, or `ramp` without any arguments plot mosaic images of Antarctica. The `bedmap2` function plots pseudocolor gridded elevation data, contoured elevation data, or inferred grounding lines or coastlines. The `measures` function plots ice surface speed as pseudocolor data or ice surface velocity as formatted vector fields via the `quivermc` function. A `seaice`

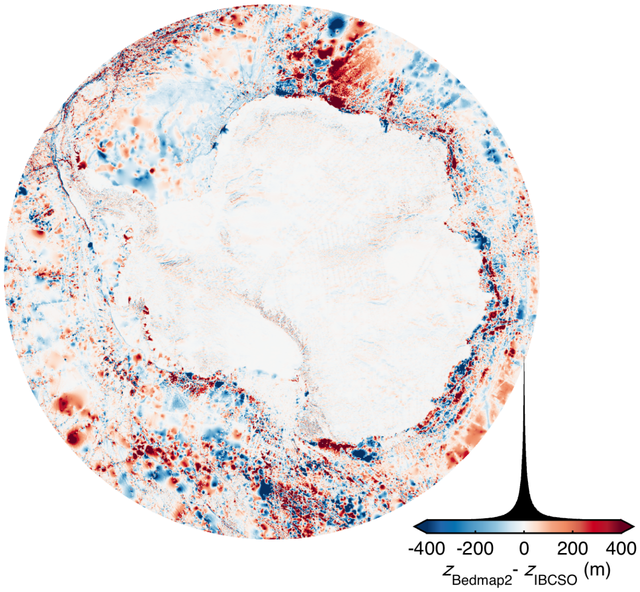

Figure 2.1: Despite differences in grids, a comparison of Bedmap2 and IBCSO bed elevations is easily obtained with `bedmap2_data` and `ibcso_interp`. DEMs are compared here with a `pcolorm` map and a histogram of differences.

function plots daily sea ice concentration grids for any user-specified date in the satellite era. Plugins are also available to plot polygons such as grounding lines, hydrostatic lines, coastlines, and ice drainage basin boundaries. The SODB plugin allows mapping of the Southern Ocean Database (SODB; Orsi and Whitworth, 1998) by plotting hydrographic station locations, gridded fields of oceanographic variables, and vertical profiles along any user-specified transect. This SODB plugin also contains an `sodb_inpolygon` function which enables easy production of θ-S diagrams for SODB stations within any user-specified polygon.

2.3.3 Methods employed by plugins

Several AMT plugins share methods for data loading and plotting. Among these methods are automatic determination of plotting coordinate systems, local data loading, and automatic map zooming to locations by feature name. Before data are plotted, each plugin determines whether the user holds a license for MATLAB's Mapping Toolbox and whether map axes are open and current. To take full advantage of features offered by MATLAB's Mapping Toolbox, plugins use geographical coordinates by default. If no Mapping Toolbox license is found, if polar stereographic Cartesian coordinates are current, or if the user requests data plotting in Cartesian coordinates, data coordinates are automatically transformed to polar stereographic Cartesian coordinates via the `ll2ps` function before plotting.

Performing numerical analysis on a digital elevation model (DEM) dataset which represents an entire continent and surrounding ocean can be computationally expensive and unnecessary for researchers who are interested in a specific geographic region. Plugins with data loading functions are designed to load only the data necessary to encompass the user's region of interest. For example, users who are interested in the Thwaites Glacier catchment may wish to load and operate on only DEM data surrounding basin 21 identified by Zwally et al.. To load only the data of interest, users may enter georeferenced arrays of an arbitrarily-shaped perimeter of interest, and a rectangular grid surrounding the region will be loaded into MATLAB. That is,

```
[~,lat,lon] = basins('grounded',21);
```

loads georeferenced arrays `lat` and `lon` which define the perimeter of ice drainage basin 21, then

```
[latgrid,longrid,z] = ibcso_data(lat,lon)
```

loads only a 1343×1119 DEM grid—just 0.8% of the datapoints found in the full ∼178-million-point IBCSO dataset. Similarly, users may specify a buffer in kilometers of extra data to load surrounding coordinates of interest. Therefore, a centerpoint may be entered with a buffer region to load a dataset of specified half-width centered on any arbitrary location. To load a 500-km-wide grid of DEM data surrounding Thwaites Glacier (75.5°S,106.75°W), the user may specify

```
[latgrid,longrid,zgrid] = ibcso_data(-75.5,-106.75,250).
```

Benefits of regional data loading are twofold: First, manual steps required of the user are minimized, thus reducing chances of human error. Second, AMT data-loading functions do not internally load then cull large datasets. Rather, pixel regions are determined before data are loaded and MATLAB's `imread` function is called with the `'PixelRegion'` option. Thus, data loading is expedited and memory usage is minimized. Data interpolation functions exploit this capability by only loading data sufficient to interpolate to user-specified points and data plotting functions only load data sufficient to fill the extents of a current map. Therefore, users are advised to zoom to a region of interest before calling any functions which plot large gridded datasets.

To streamline workflow and enable easy data exploration, some AMT plugins call the AMT core function `mapzoom` before loading or plotting data. The `mapzoom` function accepts geocoordinates or feature name strings as inputs, so viewing a MODIS Mosaic of Antarctica image of Recovery Glacier is as simple as

```
modismoa 'recovery glacier'.
```

A similar syntax is seen in the `modismoa` call used to create Figure 2.2.

2.4 Examples

Two examples of data plotting with AMT are provided below. The first example shows a labeled map of ice surface motion and surface elevation contours overlain on a satellite image of Recovery Glacier and surrounding area. The second example combines IBCSO, Bedmap2, and SODB data to generate a map and a hydrographic profile of a transect near Getz Ice Shelf.

2.4.1 Layered data map

AMT is designed to allow layering of multiple datasets in a single map. For example, ice motion can be shown in the context of visible surface features and surface elevation contours along with extents of a grounding zone. The commands

```
modismoa('recovery glacier','contrast','lc')
measures('speed','recovery glacier',...
    'colormap',brewermap(256,'blues'),...
    'facealpha',0.2,'colorbar','off')
measures('vel','recovery glacier',...
   'color',[0.03 0.19 0.42],...
   'arrowdensity',3,...
   'inset','se')
bedmap2('surfc');
asaid('gl','color',[0.90 0.33 0.05],'linewidth',3)
asaid('hl','color',[0.99 0.75 0.52],'linewidth',3)
scalebar
scarlabel({'Bailey Ice Stream',...
    'Recovery Glacier','Slessor Glacier'})
```

begin by creating a low-contrast MODIS Mosaic of Antarctica image centered on Recovery Glacier. Semitransparent ice speed is overlain with the `measures` function. The `measures` function is called again to create ice motion vectors of specified color and density and to place an inset map in the lower right-hand corner of the figure. The `asaid` function is called twice to show the span of the grounding zone from break-in-slope to the hydrostatic line. A graphical reference scale is placed with `scalebar` and features of interest are labeled with `scarlabel`. The resulting layered-data map is shown in Figure 2.2[1].

---

[1] Some examples in this paper use the `brewermap` function (Cobeldick, 2015) to generate colormaps developed by Brewer (2015).

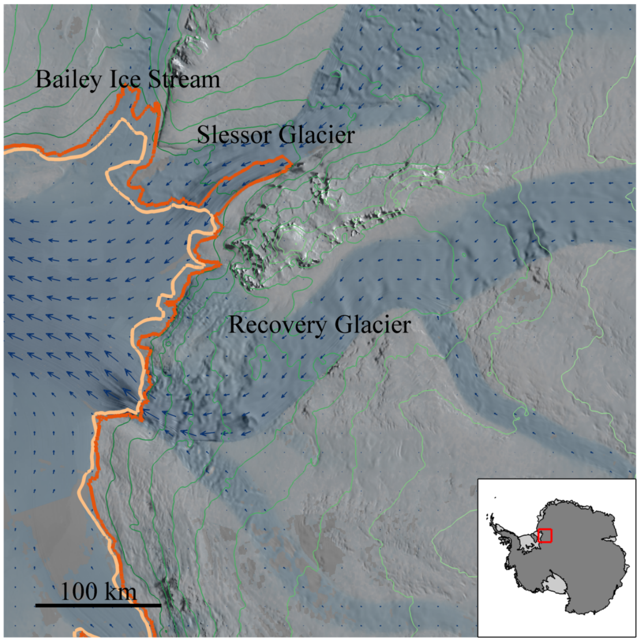

Figure 2.2: Example of a layered data map. MEaSUREs ice motion data, Bedmap2 surface elevation contours, and orange ASAID grounding zone extents are overlain on a MODIS Mosaic of Antarctica image. Features of interest are labeled with the `scarlabel` function which queries the SCAR Composite Gazetteer of Antarctica. The code to produce this figure is described in Section 2.4.1.

2.4.2 Hydrographic profile

Hydrographic profiles of SODB data are easily obtained with the `sodb_profile` function included in the SODB Toolbox plugin for AMT. The following sections of code plot the hydrographic profile near Getz Ice Shelf shown in Figure 2.3. A map of the area is created by

```
mapzoom('getz ice shelf',1000,'inset','ne')
ibcso
sodb('stations','r.','MarkerSize',12)
bedmap2 'patchshelves'
bedmap2 'patchgl'
scalebar('location','se')
scarlabel('Getz Ice Shelf','fontangle','italic',...
   'fontweight','bold'),
```

which calls `mapzoom` to center a 1000 km wide map on Getz Ice Shelf and place an inset map in the upper right-hand corner of the map. The `ibcso` function plots bathymetry and the `sodb` function shows hydrographic station locations as red dots. The `bedmap2` function is called to overlay ice shelves and grounded ice as patch objects and the `scalebar` function places a graphical reference scale in the lower right-hand corner of the map. With a map open, coordinates for a hydrographic transect may be defined by calling `sodb_profile` and using mouse clicks to define a path. Alternatively, a transect may be defined with vector arrays of georeferenced or polar stereographic coordinates. For the purposes of this example, a transect is defined by 400 equally-spaced polar stereographic eastings from -1604 km to -1263 km and northings from -1411 km to -978 km:

```
x = 1000*linspace(-1604,-1263,400);
```

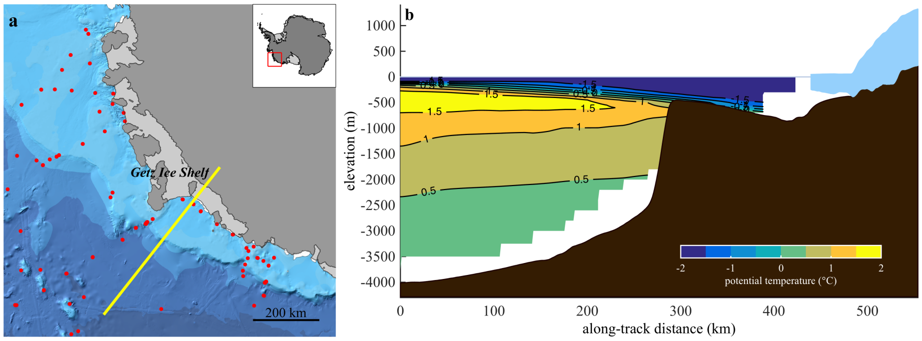

Figure 2.3: Example of a hydrographic profile. Panel **a** shows a map view of the region surrounding Getz Ice Shelf, West Antarctica. Bathymetry from the IBCSO DEM is shown in blue tones; ice shelf and grounded ice extents from Bedmap2 are shown as light and dark gray, respectively; red filled circles indicate SODB hydrographic station locations; a yellow line defines the transect of the potential temperature profile in panel **b**. Panel **b** is created with the `sodb_profile` function which plots SODB hydrographic data in context with Bedmap2 bed and ice surface elevations. The code to create this figure is described in Section 2.4.2.

```
y = 1000*linspace(-1411,-978,400);
```

The transect defined by `x` and `y` is shown on a georeferenced map by transforming coordinates with the AMT core function `ps2ll` before plotting with the MATLAB function `plotm`. The following places the yellow line which defines the transect in Figure 2.3a:

```
[lat,lon] = ps2ll(x,y);
plotm(lat,lon,'y-','linewidth',3)
```

With a transect defined in polar stereographic or georeferenced coordinates, the profile of potential temperature seen in Figure 2.3b is created by

```
sodb_profile('ptm',lat,lon,'contourf','label').
```

2.5 Conclusions

AMT provides simple geospatial data analysis functions and mapping tools along with a host of documentation files containing thorough, Antarctica-specific examples. A distance calculation function easily determines distance along transects such as flight lines or ship tracks given by geographic coordinates or polar stereographic eastings and northings. A crossover function efficiently finds locations and times of flight or ship track crossovers while allowing the user to specify conditions for crossover calculation. A feature name database lookup function returns geographic or polar stereographic coordinates of any feature identified in the SCAR Composite Gazetteer of Antarctica. The tools in AMT provide a common platform for plugins to import multiple datasets and allow direct comparison, regardless of native data format.

The AMT package provides thoroughly-documented, open-source, open-architecture tools for analysis and display of Antarctic geospatial data. AMT streamlines workflow and enables direct comparison of multiple datasets through common commands and syntax. AMT and several plugins are available free of charge on the Mathworks File Exchange website. Users are encouraged to develop and share dataset-specific plugins for the AMT package.

Chapter 3

A review of ice shelf basal channels

The cold, dark environment beneath Antarctica's floating ice shelves is where the Earth's largest ice sheet meets the global ocean in a complex, constantly-evolving balance of forces. Under ice shelves, broad-scale changes in water temperature driven by ocean warming or cooling can alter circulation and melt patterns (Gwyther et al., 2015); localized outflow of buoyant subglacial meltwater can create areas of intense circulation and increased thermal exchange (Gladish et al., 2012); and changes in water cavity geometry due to melt, freeze, grounding line migration, or changes in ice flow can affect water circulation and heat exchange under an ice shelf (Jenkins et al., 2010; Jacobs et al., 2011). Ice shelves weakened by melt can result in speedup of nearby grounded ice through lost backstress (Dupont and Alley, 2005; Fürst et al., 2016), which can destabilize vast marine-based areas of the ice sheet (Weertman, 1974; Goldberg et al., 2009) and lead to global sea level rise (Alley et al., 2005; Joughin et al., 2012). The processes governing energy exchange at the ice/ocean interface beneath Antarctica's ice shelves impact the global climate

---

Section 3.6 of this chapter contains my contribution to C. Dow, W. Lee, J. Greenbaum, C. Greene, D. Blankenship, K. Poiner, A. Forrest, D. Young, and C. Zappa. Basal channels drive active surface hydrology and transverse ice-shelf fracture. in review.

system, so we must understand these processes to understand how Antarctica will respond to a changing climate.

3.1 Impact of basal channels on ice shelves

Basal channels form beneath ice shelves where rising plumes of water cause melt by convective heat transfer. Basal channels are found primarily under the most rapidly-changing ice shelves in Antarctica (Alley et al., 2016), and are of interest for their ability to focus melt, transport heat, and perhaps weaken (Vaughan et al., 2012; Münchow et al., 2014; Alley et al., 2016; Gourmelen et al., 2017; Dow et al., in review) or strengthen (Gladish et al., 2012; Millgate et al., 2013) ice shelves. Basal channels can be thought of as upside-down, underwater rivers which are carved into the underside of ice shelves and carry buoyant meltwater-laden waters from the deep ice shelf base toward the open ocean. It is difficult to access or directly measure processes within ice shelf basal channels, but their presence can be inferred from altimetry or satellite imagery by characteristic lineations where the ice shelf surface slumps toward hydrostatic equilibrium (Fahnestock et al., 2000; Fricker et al., 2009; Alley et al., 2016).

In a number of recent publications, the impact of basal channels on ice shelves has been framed as an outstanding controversy, whereby we do not currently understand whether basal channels have a net effect of strengthening or weakening ice shelves. However, this adversarial approach tends to neglect specific physical processes in favor of simplification toward a single resolution of whether basal channels may be deemed to have a net positive or negative impact on ice shelf stability. Rather, the evidence shows nuance regarding how different ice shelves are affected by their basal channels.

Channelized basal melt was first observed on the floating portion of Petermann Glacier in Greenland by Rignot and Steffen (2008), who speculated that the formation of channels should mechanically weaken the ice shelf. Later, an airborne survey of Petermann Glacier provided evidence that channelized thinning indeed structurally weakened the ice shelf and led to a series of major calving events (Münchow et al., 2014). Elsewhere in Greenland, Motyka et al. (2011) found that increased availability of warm deep water from the Irminger Current (Holland et al., 2008a) led to enhanced buoyancy-driven convection beneath the ice tongue of Jakobshavn Isbræ, which formed a single basal channel where thinning rates exceeded 200 $\mathrm{m\,yr^{-1}}$, and this enhanced channelized melt has likely contributed to ongoing speedup and retreat of the glacier.

Around Antarctica, ice shelf basal channels are most densely concentrated in regions where warm Circumpolar Deep Water (CDW) has at least intermittent access to ice shelf bases, particularly in the Amundsen and Bellingshausen Sea sectors of West Antarctica where ice shelves are currently undergoing rapid change (Alley et al., 2016; Pritchard et al., 2012; Rignot et al., 2013; Depoorter et al., 2013; Paolo et al., 2015). The correlation between the presence of basal channels and ice shelf thinning is not an indication that basal channels lead to high rates of thinning; however, observations do suggest that the presence of basal channels can encourage mechanical failure within an ice shelf. Vaughan et al. (2012) found that the nonuniform ice thickness associated with basal channels in Pine Island Ice Shelf sets up

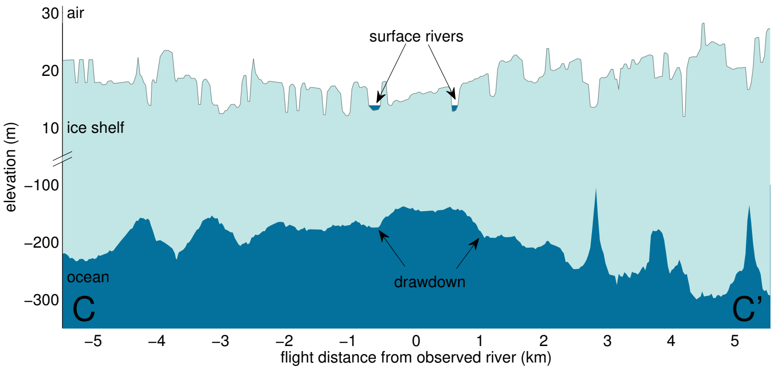

Figure 3.1: Profile view of laser surface elevation and radar basal elevation data collected by NASA IceBridge at Nansen Ice Shelf, Terra Nova Bay, East Antarctica. Note the difference in scales of surface and basal elevation axes. The large, kilometers-wide basal channel creates a large-scale surface depression, where water collects into one to two rivers. The water mass of the rivers causes local drawdown at the ice shelf base.

local hydrostatic imbalances, bridging stresses within the ice, and a resulting tensile stress field that creates basal crevasses in the crests of basal channels and surface crevasses between channels. A similar crevasse pattern was reported at Larsen C Ice Shelf by McGrath et al. (2012a). Basal crevasses can break through a third of the ice thickness, suggesting mechanical stability may be compromised particularly within channels, where ice is already thinner than its surroundings. In support of the idea that basal channels may be preferential paths for mechanical failure, Alley et al. (2016) showed that Roi Baudouin Ice Shelf has clearly split along the path of a basal channel. Meanwhile, Dow et al. (in review) link a major calving event at Nansen Ice Shelf to hydrofracture driven by surface rivers which formed over a basal channel (Figure 3.1) similar to the surface rivers which form over basal channels at Amery Ice Shelf (Phillips, 1998; Fricker et al., 2009). As the basal channel at Nansen Ice Shelf provided a preferred path for the surface river which led to the 2016 calving event, it is reasonable to assume a similar process may take place on other ice shelves around Antarctica which may see increased surface melt in a warming climate. An alternative hypothesis is put forth by Bell et al. (2017), who suggest that at Nansen and other ice shelves throughout Antarctica where surface water systems have been observed (Kingslake et al., 2017), the hydrological systems may play a role in protecting the ice shelves from hydrofracture by exporting water from the surface.

Further arguments that basal channels strengthen ice shelves come from two ocean modeling studies by Gladish et al. (2012) and Millgate et al. (2013). In each study, an idealized ice shelf geometry similar to Petermann Glacier or Pine Island Glacier was used to investigate parameters that affect channelized melt. Both studies found that increasing the total number of longitudinal channels in a 20 km wide ice shelf domain prevented the formation of major plumes and thereby reduced overall ice shelf melt. However, two points are worth noting: First, neither study attempted to model ice mechanics, and instead used total ice shelf melt as a proxy for overall ice shelf weakening; yet, ice shelves fail due to concentrated stress such as the elevated stress observed within channels—ice shelves do not fail simply from area-averaged thinning. Second, both studies concluded that increasing the number of channels protects an ice shelf by preventing the formation of fewer, larger channels which are associated with elevated melt rates. Using overall melt as a proxy for ice shelf stability, one could argue that large channels have an overall effect of weakening ice shelves. Indeed, when Gladish et al. (2012) attempted to model an ice shelf without any channels, a single jet formed and created a megachannel which melted through the entire thickness of the ice shelf. Gladish et al. (2012) concluded that Petermann's many narrow channels protect the ice shelf by preventing the formation of a single, high-melt-rate megachannel.

3.2 Basal channel formation

The presence of a longitudinal basal channel under an ice shelf indicates focused convection-driven sub-ice melt. Convection can be focused by pre-existing basal topography, by a persistent jet of buoyant subglacial discharge water circulation within the ice shelf cavity.

3.2.1 Topography as a source of basal channels

Basal channels can sometimes be attributed to topographic undulations imparted by the bed before ice goes afloat, where the bed acts as a die in an extrusion process. Subglacial topographic highs near the grounding line at Roi Baudouin Ice Shelf in Dronning Maud Land, Antarctica form as eskers which result from sediment deposition in subglacial water conduits that widen close to the ocean (Drews et al., 2017). Jenkins et al. (2006) found that a ridge in the grounding zone of Rutford Ice Stream carves out a channel of thin ice, and channelization is then enhanced by elevated melt rates within the channel compared to its surroundings. Similarly, modeling efforts by Gladish et al. (2012) and Sergienko (2013) indicate that melt channels require some topographic undulations to seed channel formation, though the initial basal topography is not preserved as melt can dramatically reshape an initial perturbation.

Channelized melt can be the result of basal topography created by complex stress fields over grounded ice whereby a ribbon of strain-thinned ice advects downstream and manifests as a basal channel and surface trough on an ice shelf. Glasser et al. (2015) mapped approximately 3600 flow stripes throughout Antarctica, which primarily originate on land, but are advected downstream and in many cases serve as basal channels on ice shelves. Fricker et al. (2009) found that channels form in the suture zones between the ice streams feeding Amery Ice Shelf, and similarly, Dow et al. (in review) found that the basal channel and surface river system seen at Nansen Ice Shelf lies at the confluence of Reeves Glacier and Priestly Glacier.

3.2.2 Subglacial discharge as a source of basal channels

Modeling by Sergienko (2013) and Dallaston et al. (2015) indicates that in the absence of basal topographic features, a rising plume can be sufficiently focused by localized subglacial freshwater discharge such that its high rate of convection can melt a channel into the ice shelf base. Locations of subglacial discharge modeled by Le Brocq et al. (2013) are well aligned with surface troughs visible in satellite imagery on the Filchner-Ronne Ice Shelf and elsewhere around Antarctica (Marsh et al., 2015; Alley et al., 2016). Le Brocq et al. (2013) argue that subglacial outflows are a more effective means of generating channels than natural convective heat transfer from the ocean alone, and Langley et al. (2014) showed that even in the cold waters below Fimbul Ice Shelf a network of basal channels has developed, likely as a result of subglacial meltwater from Jutulstraumen Glacier (Alley et al., 2016).

3.2.3 Cavity circulation as a source of basal channels

In some cases, longitudinal basal channels cannot be attributed to any topographic or hydrographic features, but seem to form spontaneously. In the absence of basal topography to steer a rising plume, or of localized subglacial discharge to focus convection, distributed rising meltwater may converge into a jet and create a melt channel. The location of the jet may be affected by thermally-driven circulation within the water cavity (Gwyther et al., 2016), but in many cases the jet will preferentially form on the return-flow side of the ice shelf corresponding to Coriolis-driven circulation (Gladish et al., 2012). In Antarctica, this corresponds to the western flank of a northward-flowing ice shelf or the northern flank of an eastward-flowing ice shelf such as Totten Glacier Ice Shelf (Potter and Paren, 2013; Holland and Feltham, 2006; Mankoff et al., 2012).

3.2.4 Transverse channels

Discussion has thus far focused on longitudinal channels which approximately follow the path of ice flow. However, several ice shelves around Antarctica exhibit transverse features with a surface relief of $\sim$20 m and corresponding basal relief of $\sim$200 m, and in many cases these transverse features crosscut longitudinal channels. Although the transverse features are not aligned with ice flow, they are approximately linear and have similar geometry to longitudinal channels. Transverse channels have been observed at Larsen C Ice Shelf (McGrath et al., 2012b), Getz Ice Shelf (Alley et al., 2016), Thwaites Glacier (Logan et al., 2013), Pine Island Ice Shelf (Bindschadler et al., 2011b), and Totten Glacier Ice Shelf (Greene and Blankenship, in press). The transverse channels on Pine Island Ice Shelf were first attributed to seasonal basal melt at the grounding line modulated by atmospheric forcing of the CDW layer, with the argument that ripples of approximately annual periodicity must be caused by annual variations in forcing (Bindschadler et al., 2011b). Annual variability of ice speed was ruled out as a possible cause of the transverse channels because variations in basal stress should be transmitted to the surface instantaneously, whereas the transverse channels at Pine Island Ice Shelf appear a few kilometers downstream of the grounding line.

It is worth noting that the ice thickness amplitudes corresponding to the transverse channels at Pine Island Ice Shelf exceed 200 m, so by basal melt alone, melt rates would need to be highly localized and exceed 400 $\mathrm{m\,yr^{-1}}$ in a narrow band near the grounding line for part of each year, followed by nearly no melt for the rest of the year. Such high melt rates are unlikely and the proposed narrow focusing of melt is contradicted by Stanton et al. (2013) and Dutrieux et al. (2013) who observe that melt is not limited to the grounding zone of Pine Island Ice Shelf, but persists for half the length of the ice shelf. An alternative explanation for the transverse channels at Pine Island Ice Shelf is given by Sergienko (2013), who shows that periodic transverse variations in ice thickness can form on an ice shelf in steady state with constant ice flow and constant oceanic forcing as a mechanical response to lateral shear along the sides of a bounded ice shelf.

3.3 Longitudinal basal channels after formation

After receiving some initial guidance from topography, water column circulation, or subglacial outflows, basal channels are melted into their form by convective heat transfer driven by theromhaline circulation. Water circulation within a channel is similar to the ice pump described by Lewis and Perkin (1986), but a clarification should be made that basal channels do not necessarily involve the accretion of marine ice toward the ice shelf front. In most models and observations, channelized melt appears to follow Mode 1 of the ice pump described by Jacobs et al. (1992), whereby melt is concentrated at the deepest part of the ice shelf base and tapers with distance from the grounding line. The tendency of melt to be focused in the region of channel formation has been observed by Rignot and Steffen (2008) at Petermann Glacier, Jenkins et al. (2006) at Rutford Ice Stream, Stanton et al. (2013) and Dutrieux et al. (2013) at Pine Island Ice Shelf, Le Brocq et al. (2013) at Filchner-Ronne Ice Shelf, Marsh et al. (2015) at the Ross Ice Shelf, and in models by Gladish et al. (2012) and Sergienko (2013).

3.3.1 Focused basal melt where channels form

Channel formation typically occurs near the grounding line, where melt rates are high because the ice base is deep within the water column where the pressure-melting temperature is suppressed (Jenkins and Doake, 1991); basal topography is steep, which is associated with high rates of heat entrainment within the mixed layer (Little et al., 2009); and the deepest part of the water cavity is where dense, warm CDW is most likely to be present (Thoma et al., 2008; Wåhlin et al., 2010; Jacobs et al., 2011; Rintoul et al., 2016). In some locations around Antarctica, channels appear to form away from the grounding line (Alley et al., 2016), but the formation process for such channels is not fully understood.

3.3.2 Plume flow within basal channels

In the ice pump mechanism, the cycle of ice/ocean interaction begins near the grounding line, where the relative warmth of the ocean water begins the melt process. As meltwater is entrained into the mixed layer along the ice shelf base, the mixed layer becomes increasingly buoyant and rises along the ice shelf base with increasing velocity. Rates of heat transfer and subsequent melt are positively related to the velocity of water as it interacts with ice (Holland et al., 2008b; Gladish et al., 2012; Gwyther et al., 2015). This creates a positive feedback mechanism whereby meltwater increases the buoyancy of a rising plume, which increases the plume velocity, which increases melt and entrains more buoyant meltwater into the rising plume. However, the addition of cold meltwater into the mixed layer also reduces the mixed layer temperature and therefore reduces its capacity to induce melt. Furthermore, as water rises toward the ocean surface, the local pressure-melting temperature increases and the water temperature must decrease. This represents a negative feedback mechanism whereby rising water with an increasing proportion of cold meltwater will have a decreasing capacity to cause melt. Accordingly, channelized melt is most intense near the grounding line in models (Gladish et al., 2012; Millgate et al., 2013; Sergienko, 2013; Dallaston et al., 2015) and observations (Rignot and Steffen, 2008; Dutrieux et al., 2013; Stanton et al., 2013; Le Brocq et al., 2013; Marsh et al., 2015).

After inducing melt near the grounding line, a rising channelized plume of water may become mixed such that it matches the density of the surrounding water column, at which point the plume may detrain and no longer interact with the ice shelf base (Jacobs et al., 1992; Gladish et al., 2012). If, however, the plume maintains buoyancy relative to its surroundings, it will continue to rise along the channel and can exit the ice shelf cavity in a focused jet that creates an open-water polynya at the ice shelf front (Mankoff et al., 2012; Alley et al., 2016). If polynya water contains iron-rich subglacial meltwater, it can provide fertilization for plankton blooms (Death et al., 2014; Herraiz-Borreguero et al., 2016), which are observable in satellite imagery (Arrigo and Van Dijken, 2003).

If the water cavity is sufficiently cold, rising channelized plume water may complete the ice pump cycle (Lewis and Perkin, 1986) by generating frazil ice crystals that accrete on the ice shelf base (e.g., Oerter et al., 1992; Holland et al., 2009). Channelized freeze-on of marine ice has not yet been directly observed in Antarctica, although bands of marine ice at Amery Ice Shelf (Fricker et al., 2001; Craven et al., 2009) apparently align with flow stripes visible in satellite imagery.

3.3.3 Channels amplitude decay

Marine ice accumulation may act to fill in basal channels away from the grounding zone, but even in the absence of channelized freezing, other processes act to smooth basal topography toward the ice shelf front. Away from the grounding line, melt rates within channels decline considerably while the keels between channels may descend into deeper, warmer water where melt continues (Dutrieux et al., 2013). Simple spreading of ice also tends to diminish channel amplitudes as thickness gradients encourage channels to slowly close by diffusion (Casassa and Whillans, 1994; Gudmundsson et al., 1998).

3.3.4 Bridging stresses in channelized ice

In addition to gravitationally-driven diffusion, complex stress fields can affect channel shape wherever ice is not in local hydrostatic equilibrium. A basal channel whose width is on on the order of an ice thickness or less must be supported at least partly by bridging stresses from the sides of the channel (Vaughan et al., 2012; Humbert et al., 2015). As a result, the horizontal velocity of the ice may not be constant with depth as ice tends to converge toward the center of channels at the surface while diverging from the channel crests at the ice base (Dutrieux et al., 2013; Drews, 2015). The depth-dependent stress field can produce surface crevasses between channels and basal crevasses in the crests of channels (Vaughan et al., 2012; McGrath et al., 2012b).

3.4 Evidence of channels in satellite imagery

Flow stripes have been observed in satellite imagery around Antarctica (Fahnestock et al., 2000; Glasser et al., 2015). In many cases, flow stripes on ice shelves correspond to basal channels whose topography can be mapped by photometric methods (Raup et al., 2005) or laser altimetry (Fricker et al., 2009; Münchow et al., 2014; Marsh et al., 2015; Alley et al., 2016). The presence of polynyas in satellite images can also provide evidence for channelized plume flow. Mankoff et al. (2012) analyzed a time series of satellite images and found polynyas at the outlets of three basal channels in Pine Island Ice Shelf. Alley et al. (2016) followed a similar procedure and determined that ice shelf front polynyas are most often associated with channels formed by ocean forcing rather than subglacial discharge.

3.5 Temporal evolution of longitudinal basal channels

Where an ice shelf exhibits longitudinal surface depressions that become more or less pronounced over time, the localized changes can be interpreted as changes in channelized basal melt, with two exceptions: First, if a channel appears to become deeper along one flank while becoming shallower along the opposite flank in an Eulerian measurement, changes in ice flow direction may be responsible for advecting the channel to one side. A Lagrangian measurement of a laterally-advected channel should indicate no significant change but requires contemporaneous velocity measurement rather than a steady-state velocity assumption. Second, longitudinal changes in surface elevation can be caused by local surface mass balance anomalies such as blowing snow or surface meltwater-driven firn collapse which may align with the channelized surface topography. The spatial resolution of current atmospheric and firn models is too coarse to account for the kilometer-scale phenomena of interest (Lenaerts et al., 2012; Ligtenberg et al., 2011) so we must acknowledge that surface processes may contaminate the assumption that surface elevation anomalies are caused purely by changes in basal melt.

3.5.1 A subglacial source moves or changes its discharge rate

Longitudinal surface elevation changes linked to basal melt may be caused by changes in subglacial discharge, grounding line migration, or a changing water circulation pattern beneath the ice shelf. In agreement with models by Gladish et al. (2012) which show that channelized melt rates can be highly sensitive to plume velocity driven by subglacial discharge, Le Brocq et al. (2013) argue that subglacial outflows are a much more efficient means of incising basal channels compared to ocean-driven melt alone. Thus, longitudinal changes in surface elevation observed near the grounding line may be caused by changes in melt driven by subglacial discharge, particularly if channels align with subglacial discharge locations predicted by water-routing software.

Subtle changes in subglacial discharge rates have not yet been observed by surface altimetry; however, changes in subglacial discharge locations have been observed where the advected surface elevation record shows channel shutdown in concert with the appearance of a neighboring channel (Le Brocq et al., 2013; Marsh et al., 2015). The appearance of a new basal channel timed with the shutdown of a neighboring channel implies changes in the pressure gradient beneath grounded ice which results in subglacial water flow switching. A change in channelized melt rate aligned with a predicted subglacial discharge location implies changes in subglacial discharge rate, which may be linked to subglacial lake drainage events.

Given the iron-rich nature of subglacial meltwater, changes in subglacial discharge may potentially be inferred from biological productivity measurements at the channel terminus. However, such a detection would require that the subglacial discharge rise fully to the surface without detraining from the plume.

3.5.2 Grounding line migration incises new basal topography

Where changes in channelized basal melt near the grounding line cannot be linked to subglacial discharge, grounding or ungrounding from local topographic highs could result in basal topographic changes sufficient to change channelized melt. Grounding line migration has been observed at Totten Glacier (Li et al., 2015), and airborne radar data (Blankenship et al., 2011) may be available to confirm the presence or absence of topographic features available to incise basal channels.

3.5.3 Changes in ocean forcing

Gwyther et al. (2016) have shown that the water circulation pattern beneath an ice shelf can be affected by the large-scale availability of heat in the water cavity. At the Totten Glacier Ice Shelf, a sufficiently large increase in water temperature from the ocean could induce increased melt on the southern side of the ice shelf where a new plume could form a jet, incise a new channel, and deflect ice shelf cavity circulation away from the Coriolis-preferred northern flank of the ice shelf. This case would require an ocean-driven water temperature increase of several degrees, which is expected to be paired with large-scale changes in surface elevation and ice velocity (Christianson et al., 2016).

The shifting water circulation patterns modeled by Gwyther et al. (2016) were in response to a rather large 2.4°C increase in ocean temperature. Such reorganization may not occur or be observable from smaller changes in ocean temperature, which are expected to induce an approximately quadratic increase in melt rate as a result of increased thermal forcing (Holland et al., 2008b). If the entire water cavity experiences a small increase in temperature, melt rates beneath the entire ice shelf are expected to increase accordingly and be observed as broad-scale surface lowering. By an alternative mechanism of ocean forcing, a rising thermocline should generate increased melt primarily in a band of basal elevations corresponding to the change in thermal forcing (Padman et al., 2012).

3.5.4 Interpretation of surface elevation change

Chapter 4 presents a method of detecting surface elevation change using repeat photoclinometry applied to a fifteen year record of MODIS images. Changes observed with the repeat photoclinometry technique may be interpreted with the following guidelines. Wherever channelized melt rates change, the resulting surface elevation pattern is expected to be asymmetric about the centerline of the channel. At Totten Glacier Ice Shelf, an increase in channelized melt should lead to a thicker mixed layer and increased plume velocity on northern channel flanks due to Coriolis steering (Gladish et al., 2012; Sergienko, 2013). Steeper surface slopes have been observed on the Coriolis-preferred side of longitudinal channels on ice shelves around Antarctica (Alley et al., 2016) and are expected at Totten Glacier Ice Shelf. Millgate et al. (2013) found that when basal channels are narrow, Coriolis effects are not observed within them and circulation in the channels is fundamentally altered. However, such narrow channels are unlikely to be sufficiently resolved in surface altimetry due to bridging support within the ice (Humbert et al., 2015) and are thus not investigated in this surface-altimetry-based work.

3.6 Nansen Ice Shelf

Research for this dissertation included an investigation of the role played by a large basal channel in Nansen Ice Shelf, Terra Nova Bay, East Antarctica, in contributing to a major calving event in April 2016. The full study was led by Christine Dow at the University of Waterloo, and its findings are that the presence of an ice shelf basal channel produced a surface depression, where melt water concentrated, caused hydrofracture, and lead to calving (Dow et al., in review). The paper relies on a high-resolution digital elevation model (DEM) to understand surface hydrology. The process used to generate the Nansen Ice Shelf DEM and scientific rationale for each step is discussed below.

3.6.1 Surface DEM generation

To understand the surface hydrology of Nansen Ice Shelf, I generated a 50 m resolution surface DEM by combining a 1 km gridded elevation dataset by Bamber et al. (2009), the 1 arc-second ASTER GDEM2, and over 90,000 laser altimetry measurements from ICESat (Zwally et al., 2014), IceBridge ATM, and IceBridge Riegl. The custom DEM blends the high precision of ASTER GDEM2 for short-wavelength topographic features with the superior accuracy of the Bamber et al. DEM (BDEM) for large-scale features.

A custom surface DEM was developed for this work because all readily-available DEMs fail to sufficiently replicate the surface water routing behavior

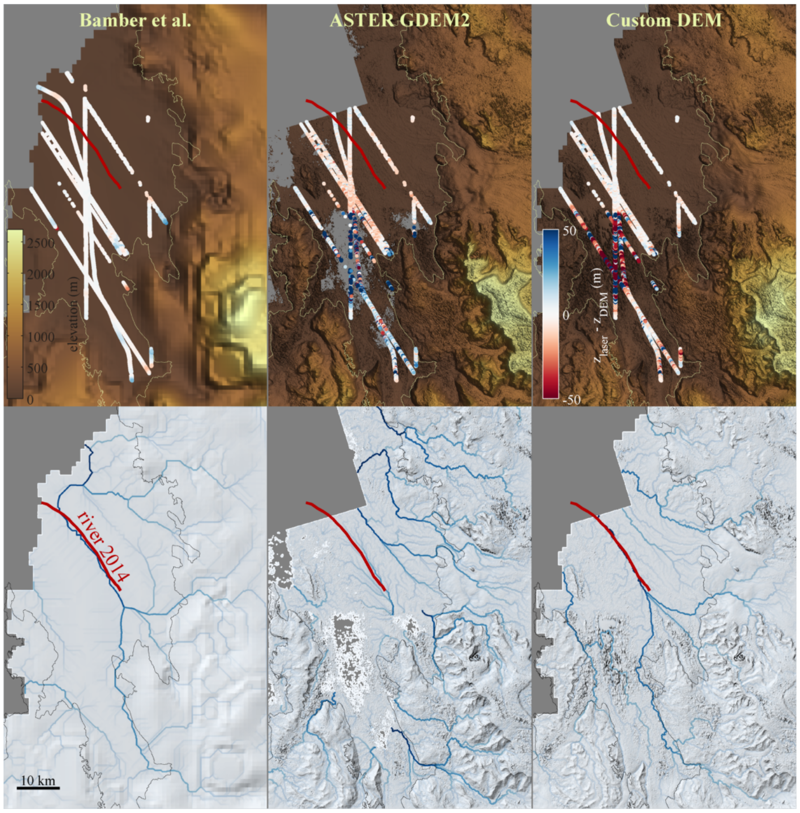

Figure 3.2: The primary components of our custom DEM for Nansen Ice Shelf are the 1 km BDEM which contributes topographic features longer than 4250 m, and the 1 arc-second ASTER GDEM2 which contributes features whose characteristic wavelength exceed 4250 m. The upper panels show surface elevation in brown tones and the difference between laser altimetry and interpolated DEM values in a polar colormap. Lower panels show flow accumulation for each DEM predicted by TopoToolbox-2. The location of the surface river observed in 2014 appears as a red line in all panels.

which has been observed on Nansen Ice Shelf. Several publicly-available DEMs were directly compared to satellite- and airborne laser altimetry using the data interpolation functions in Antarctic Mapping Tools for MATLAB (Greene et al., 2017b). Of the available DEMs, BDEM exhibited the best fit ($z_{\text{laser}} - z_{\text{DEM}} = 0.5$ m ± 3.7 m) with over 15,000 laser altimetry measurements taken over the ice shelf and ASTER GDEM2 was the poorest performer ($z_{\text{laser}} - z_{\text{DEM}} = 10.3$ m ± 51.4 m). In addition to absolute elevation error, DEM accuracy was assessed by estimating surface water routing for each DEM with TopoToolbox-2 (Schwanghart and Scherler, 2014). Each of the 1 km DEMs allow the formation of a surface river in the rough proximity of the river observed in 2014, but the finer-resolution ASTER GDEM2 produced clearly nonphysical flow accumulation including apparent landward-flowing rivers. Absolute error and predicted surface water routing for BDEM, ASTER GDEM2, and our custom DEM are shown in Figure 3.2.

BDEM was selected as the basis for the large-scale topography of the custom surface DEM. However, due to the poor performance of contributing radar altimetry along the steep topography that bounds Nansen Ice Shelf, and due to uncertain firn depth correction in radar altimetry, we adjusted the BDEM using all available laser altimetry in the region. The BDEM was produced in part with ICESat laser altimetry; however we use ICESat data release version 34 (Zwally et al., 2014), which includes a necessary range correction. ICESat measurements with any quality flags or gain values exceeding 30 were discarded. We also include airborne laser altimetry from the IceBridge Riegl (Blankenship et al., 2013) and ATM (Krabill, 2010, updated 2016) sensors. All laser altimetry measurements were given a coefficient of flexure based on ice mechanics using the Antarctic Mapping Tools `iceflex_interp` function (Greene et al., 2017b), then corrections were applied for tides using CATS2008b (Padman et al., 2002) and weatherband-filtered inverse-barometer effects (Padman et al., 2003) with ECMWF ERA-Interim surface pressure reanalysis data (Dee et al., 2011). Corrections applied to floating ice measurements were small and contributed very little to the final DEM, but are included as proper treatment of the data.

A surface was fit to the differences between measured laser altimetry surface elevations and interpolated BDEM elevations, then the fitted surface was added to BDEM and interpolated to 50 m resolution. Adjustments to BDEM were minor (<4 m) within the watershed of the observed surface river, but reached 20 m in a small area near the north end of Nansen Ice Shelf. After adjusting BDEM with laser altimetry data, the adjusted BDEM was then converted from a WGS84 ellipsoid height reference to the GL04-C geoid reference (Förste et al., 2008).

Despite the large-scale inaccuracies of ASTER GDEM2 and its failure to produce plausible surface water routing on Nansen Ice Shelf, stereo photogrammetry offers unparalleled small-scale precision. We employed a 3x3 median filter on the ASTER GDEM2 to reduce speckle and to serve as an anti-aliasing mechanism before interpolation to the 50 m grid. After interpolation, large areas of missing data were filled with values from the adjusted BDEM, but a 500 m gap between ASTER GDEM2 values and infilled values was retained, then filled using an inverse-distance weighting method to smooth the transition between ASTER GDEM2 values and adjusted BDEM values. Remaining holes in the ASTER

GDEM2 were filled by an inverse distance weighting algorithm. We do not attempt to model the surface where the ASTER GDEM2 is missing a large section of data near the southern seaward edge of Nansen Ice Shelf. ASTER GDEM2 contains an area of missing data and some likely erroneous pits and spikes due to the presence of surface snow near (74.8°S,163.5°E), but this region has negligible effects on final water routing predictions.

The custom DEM for Nansen Ice Shelf was created by summing the filled ASTER GDEM2 and the Gaussian low-pass-filtered adjusted BDEM, then subtracting the Gaussian low-pass-filtered filled ASTER GDEM2. The final product contains long-wavelength features from the adjusted BDEM and short-wavelength features from the filled ASTER GDEM2. By this method, 2π times the standard deviation of the Gaussian filter effectively represents the crossover wavelength at which the adjusted BDEM and the filled ASTER GDEM2 contribute equally to the final DEM.

The crossover wavelength was determined using TopoToolbox-2 to predict flow paths for many DEM solutions wherein a point source of water was placed at the headwaters of the surface river observed in 2014. Resulting flow path predictions were then converted to curvilinear coordinates with coordinates of the surface river picked manually from satellite imagery as the known river centerline. The best match was found with an effective crossover wavelength of 4250 m, which reproduced river flow within 347 m rms error of the observed river flow path (Figure 3.3). It should be noted that the river flow path is relatively insensitive to the choice of crossover wavelength and is reproduced within 1 km rms error whether

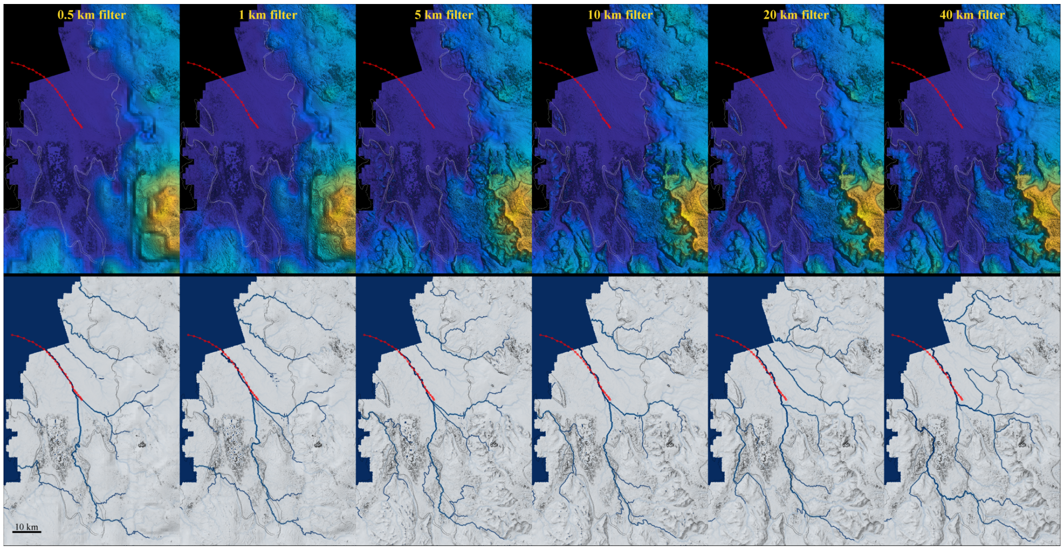

Figure 3.3: The crossover wavelength determines the relative contributions of BDEM versus ASTER GDEM2 in the final custom DEM. Low values of the crossover wavelength toward the left side of the series above favor contributions from BDEM. The relative contribution of ASTER GDEM2 increases as the crossover wavelength is increased; end members are shown in Figure 3.2. Lower panels show a flow accumulation model applied to each DEM. Flow accumulation predictions were compared to surface river observations to determine the optimum crossover wavelenth of 4250 m.

the adjusted BDEM is used alone or if it is blended with filled ASTER GDEM2 up to a crossover wavelength of 12 km. The robustness of the river feature implies it is driven by underlying large-scale topographic phenomena.

Chapter 4

Detecting small-scale ice sheet surface evolution by repeat photoclinometry

Small-scale glaciological processes can drive large-scale ice sheet behavior, but remain underreported due to a paucity of surface elevation measurements in remote polar regions. Satellite images provide a relatively long record of spatially dense surface observations which allow us to investigate changes in ice sheet topography on the spatial scales of 1 to 10 km. Inferring surface topography from satellite images is an established technique, but in previous efforts strict requirements for illumination conditions and image quality have led to a great quantity of discarded data. Relaxing quality requirements and fitting linear trends to the time series of image-derived surface topography allows inclusion of more total signal and enables blending data from multiple platforms. As a proof of concept we combine 121 MODIS images to develop a 250-m resolution map of surface elevation change at Totten Glacier, Antarctica achieving a 1-σ uncertainty of $0.22\,\mathrm{m\,a^{-1}}$ for a 15 year period. Our method of repeat photoclinometry agrees with repeat laser

---

The contents of this chapter are in publication as C. A. Greene and D. D. Blankenship. A method of repeat photoclinometry for detecting kilometer-scale ice sheet surface evolution. *IEEE Transactions on Geoscience and Remote Sensing*, in press. doi: 10.1109/TGRS.2017.2773364. The work presented here was conceived of and carried out primarily by the author of this dissertation.

altimetry while revealing clear patterns of surface elevation change associated with ice advection, channelized ice shelf basal melt, subglacial lake activity, and possible grounding line migration.

4.1 Historical applications of photoclinometry

In Greenland and Antarctica, surface topography on the order of 1 to 10 km horizontal scale provides insight into processes occurring below the ice sheet (Gudmundsson, 2003; Thorsteinsson et al., 2003; Sergienko et al., 2007; Smith et al., 2009; Dutrieux et al., 2013). For example, activity in complex networks of subglacial lakes can manifest as choreographed changes in localized surface elevation (Flament et al., 2014; Smith et al., 2017). Subglacial lakes can affect the flow of overlying ice (Bell et al., 2007; Stearns et al., 2008; Gudlaugsson et al., 2016) and their presence has been confirmed throughout Antarctica (Wright and Siegert, 2012) and in Greenland (Howat et al., 2015; Palmer et al., 2015; Willis et al., 2015).

Where an ice sheet goes afloat to form ice shelves, long, narrow basal channels can develop by a number of processes (Gladish et al., 2012; Le Brocq et al., 2013; Sergienko, 2013; Graham et al., 2013; Marsh et al., 2015), may serve to structurally weaken (Vaughan et al., 2012) or stabilize (Gladish et al., 2012; Millgate et al., 2013) the ice, and can provide a centuries-long record of ice shelf behavior (Fahnestock et al., 2000). Surface expressions of basal channels have been observed around Antarctica (Alley et al., 2016) and in Greenland (Münchow et al., 2014). Understanding the respective roles of subglacial lakes and ice shelf basal channels requires an ability to accurately measure surface topography and monitor topographic changes through time.

Photoclinometry[1] is a well-established method of extracting topographic information from a single image such as a satellite photograph. For an image of a surface of uniform albedo, the brightness of each pixel is assumed to be related to the target's surface slope, and topography is generated by integrating along the inferred slopes. Van Diggelen (Van Diggelen, 1951) applied photoclinometry to images of the Moon and the technique has since been applied to other astronomical objects (e.g., (Wildey, 1975; Howard et al., 1982)). On Earth, photoclinometry has been used to study land and atmospheric phenomena including volcanic plume top topography (Glaze et al., 1999). Applications to the cryosphere began when Dowdeswell and McIntyre (Dowdeswell and McIntyre, 1987) used Landsat imagery to characterize Antarctic surface roughness and Rees and Dowdeswell (Rees and Dowdeswell, 1988) quantified the slope uncertainty for photoclinometry applied to Landsat images of snowy regions. Bindschadler and Vornberger (1994) described in detail how to use a Landsat TM image to obtain the surface topography of Kamb Ice Stream, Antarctica while Cooper (Cooper, 1994) generated a surface of Rutford Ice Stream, Antarctica from a SPOT 1 image. Scambos and Fahnestock(Scambos and Fahnestock, 1998) generated topography from an Advanced Very High Resolution Radiometer image and the work was later extended to develop a complete elevation map of the Greenland Ice Sheet (Scambos and Haran, 2002). Bindschadler et al. (2002) used photoclinometry to characterize surface do-

---

[1] In some texts, photoclinometry may be referred to as *shape-from-shading* or *photometry*. The method of photoclinometry described in this paper and the use of stereo photography to generate surface topography are different types of *photogrammetry*.

lines on Larsen Ice Shelf, Antarctica and Liu (2003) introduced yet another method of extracting shape from shading in a SPOT image of Crary Ice Rise, Antarctica. Photoclinometry has proven useful for generating static topography, but has not gained traction as a tool to investigate surface elevation changes through time, perhaps due to a conception that the high-noise technique cannot reliably detect small signals of elevation change.

Small-scale surface elevation changes have been observed by a number of other remote sensing methods including laser altimetry (e.g., (Fricker et al., 2007; Fricker and Scambos, 2009; Young et al., 2015)), interferometric synthetic aperture radar (InSAR) (Gray et al., 2005), and satellite image differencing (Fricker et al., 2007; Fricker and Scambos, 2009; Bindschadler et al., 2010), but each method comes with a unique set of limitations. The common thread among all altimetry in polar regions is a chronic paucity of data in space and time. Large gaps exist between ground tracks of satellite altimeters and data collection is often limited by clouds, surface slopes, and relatively short sensor lifespans.

In many locations stereo photogrammetry can provide high-resolution surface topography (Shean et al., 2016), but data coverage is limited by a relative rarity of satellites with stereo capability and by restrictions on surface conditions and illumination angles for stereo processing. Stereo photogrammetry benefits from high contrast provided by rock outcrops, blue ice, surface debris, and well-defined surface features, but performance suffers where images appear nearly featureless.

The method of photoclinometry detailed in this paper excels in large regions of uniform albedo, but is limited by a fundamental assumption that all variations in image brightness are a function only of variations in surface slope. The direct relationship between surface slope and pixel brightness breaks down in the presence of nonuniform snow grain size (Dozier et al., 1981; Kuipers Munneke et al., 2008), heterogeneously distributed snowpack density (Warren, 1982), surface frost (Scambos and Fahnestock, 1998), shadows (Cooper, 1994), or inclusion of any materials such as nunataks that do not perfectly match the optical properties of snow (Hurt, 1991). But in regions of uniform albedo, the satellite image record can provide decades of small-scale topographical information. Individual digital elevation models (DEMs) generated by photoclinometry typically contain appreciable amounts of noise, but by fitting a linear trend to many photoclinometric DEMs of a region, small-scale surface elevation trends can be measured to a level of precision which may be useful for glaciological applications. In this paper we describe a method of constructing DEMs by photoclinometry and we use 15 years of MODerate-resolution Imaging Spectroradiometer (MODIS) images of Totten Glacier, Antarctica as a test case to assess the characteristic noise of the measurement technique. Uncertainty estimates are validated by comparison to laser altimetry.

4.2 DEM construction

4.2.1 Preprocess satellite images

Photoclinometry can be applied to airborne or satellite images. For this analysis we use MODIS images collected from Aqua and Terra satellites in the band 2 spectral range, which spans 841 nm to 876 nm and has a spatial resolution of

250 m. The MODIS dataset was selected because it is freely available for research purposes and offers a consistent 15+ year record with at least 20 images per year of much of coastal Antarctica and Greenland. We use publicly available images of East Antarctica's Sabrina Coast (Scambos et al., 2001, updated 2017) and we manually discard any images where clouds are visible over Totten Glacier. We rotate each image such that rows of pixels align with the direction of the sun. Rotation is performed by the `imrotate` function in MATLAB, which applies a simple rotation matrix transformation with bicubic interpolation.

4.2.2 Construct a reference DEM

Before performing photoclinometry, we construct a reference DEM (RDEM) which will be used to both calibrate the photoclinometric relation for each image, and to constrain final DEMs to known large-scale topography. To begin, we evaluated the accuracy of existing gridded DEMs using available laser altimetry measurements. Surface elevations from three publicly available 1 km resolution DEMs were referenced to the WGS84 ellipsoid and bilinearly interpolated to the locations of 399,892 elevation measurements obtained by satellite and airborne laser altimetry. The procedure by which we processed laser altimetry is described in the Appendix. Accuracy of each DEM is shown in Figure 4.1. Bedmap2 (Fretwell et al., 2013) performs poorly, with surface elevation errors exceeding 170 m near the deep western grounding line of Totten Glacier. A DEM compiled by Bamber *et al.* (Bamber et al., 2009) was expected to agree well with laser altimetry because it was generated in part with ICESat data, but it shows a mean offset of 6.8 m when

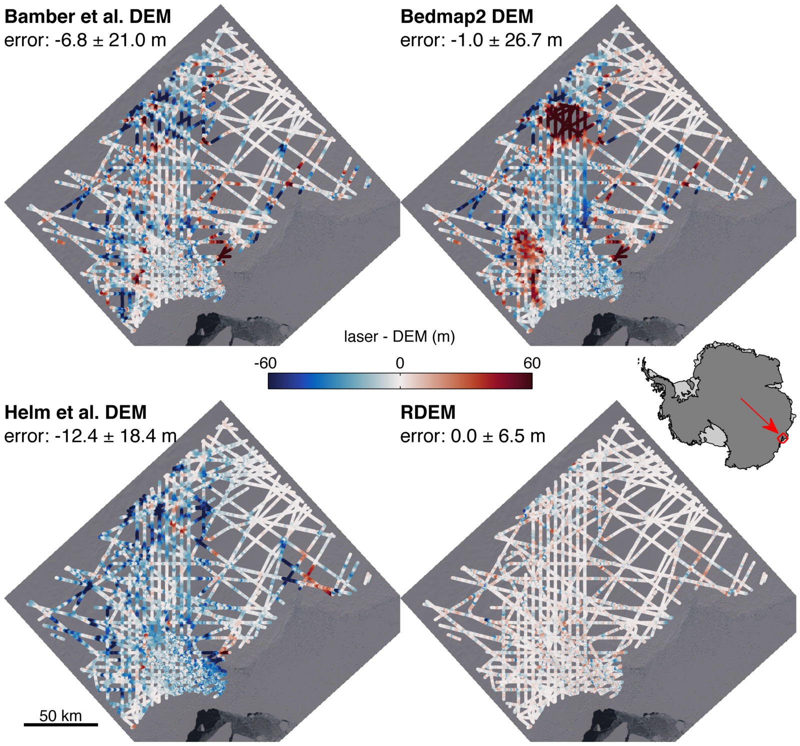

Figure 4.1: Laser altimetry reveals large errors in current publicly available 1 km Antarctic surface DEMs. Errors are shown as the mean difference between laser altimetry measurements and interpolated DEM values ± one standard deviation of differences. We developed a reference DEM (RDEM) by fitting a surface to the difference between 399,892 laser altimetry measurements and the DEM developed by Helm *et al.* (Helm et al., 2014), then added the difference surface to the Helm *et al.* DEM. Remaining errors in RDEM are due to small-wavelength features not captured by the 1 km RDEM and a changing surface over the ∼10 years of ICESat and ICECAP laser altimetry data collection.

airborne laser altimetry is included in the comparison. A DEM constructed from CryoSat-2 data by Helm et al. (Helm et al., 2014) exhibits a substantial mean offset of 12.4 m, but after accounting for the mean offset the Helm *et al.* DEM shows the lowest standard deviation of error.

Inspection of Figure 4.1 reveals that errors are spatially correlated within each of the 1 km DEMs. The spatial correlation allows us to fit a surface to the errors and we construct RDEM by adding the fitted surface of errors to the 1 km DEM provided by Helm *et al.* (Helm et al., 2014). A smoothing parameter is manually tuned in the surface fitting process to provide the best fit with laser altimetry while disallowing any surface dips or spikes which would be visible in shaded-relief imagery of the resulting surface. The resulting difference between laser altimetry and RDEM is 0.0 ± 6.4 m, which is primarily due to small-scale features not captured by the 1 km resolution of RDEM, but also reflects a changing surface over the timespan of laser measurements.

4.2.3 Calibrate photoclinometry equation

To calibrate a relation between each satellite image and RDEM, we linearly interpolate RDEM values to the geolocation of each pixel in the satellite image then rotate the interpolated RDEM grid to match the sun-oriented satellite image. The sun-oriented surface slope of RDEM α_{RDEM} is then taken as the arctangent of the surface elevation gradient along rows of the sun-oriented RDEM. Following Raup *et al.* (Raup et al., 2005), we remove the elevation bulge associated with the curvature of the Earth before calculating α_{RDEM}. The elevation bulge z_{e} relative to

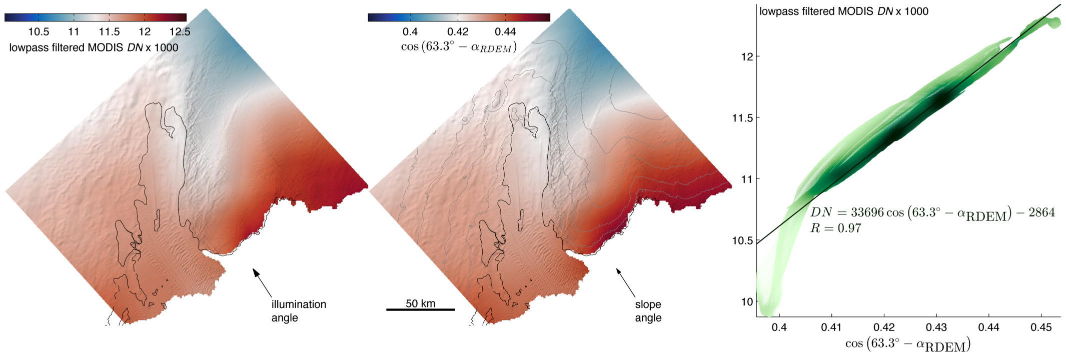

Figure 4.2: In regions of uniform albedo, surface brightness is related to surface slope in the direction of sunlight. **Left:** Color shows a lowpass filtered MODIS image from October 11, 2009. An InSAR-derived grounding line is overlaid in black (Rignot et al., 2011a). **Center:** Color shows the lowpass filtered surface slope of RDEM in the direction matching the illumination angle of the left panel. Color is scaled such that white corresponds to zero slope in the direction of sunlight. Surface elevation contours at 250 m intervals are overlaid in gray. **Right:** A relation between pixel brightness in each MODIS image and surface slope is obtained by a linear fit between all grid cells of the lowpass filtered MODIS image and the lowpass filtered RDEM. Dipping DN values toward the left of the scatter plot correspond to a small patch of blue ice.

a flat plane is approximated as

$$z_{\mathrm{e}} = \sqrt{r_{\mathrm{e}}^2 + \sqrt{(x - x_{\mathrm{n}})^2 + (y - y_{\mathrm{n}})^2}} - r_{\mathrm{e}}, \tag{4.1}$$

where $r_{\mathrm{e}} = 6360000$ m is the approximate radius of the Earth at 67°S, polar stereographic coordinates (x, y) correspond to the location of each pixel, and $(x_{\mathrm{n}}, y_{\mathrm{n}})$ describes the sensor's nadir position in polar stereographic coordinates. Accounting for the curvature of the Earth is essential for proper calibration where an image covers a large area such as the case of MODIS images, in which the Earth's surface drops more than 10 km from the center of an image to the edge.

Assuming a diffuse Lambertian surface (Lambert, 1760) of uniform albedo and no shadows or sensor saturation present in the image, the digital number DN of each pixel in an image is related to the sun-oriented surface slope α to the first order by the photoclinometric relation

$$DN = A \cos(\theta_{\mathrm{sun}} - \alpha) + B, \tag{4.2}$$

where θ_{sun} is the solar zenith angle[2] and A and B are constants related to sensor properties, surface reflectance, and atmospheric scattering (Bindschadler and Vornberger, 1994). We calibrate Equation 4.2 in a manner similar to (Scambos and Fahnestock, 1998) and (Scambos and Haran, 2002) using spatially lowpass-filtered values of DN and α_{RDEM} to find best-fit values of A and B by least squares. We tested several images and found that a 2D moving average filter with a block size

---

[2] Some photoclinometry texts use the solar elevation angle, which is the complement of the solar zenith angle.

of 46 km (184 pixels) on each side provided the best correlation between DN and α_{RDEM}. Values of A and B are calibrated for each image and a correlation coefficient R describing the fit of all pixels is logged as a simple measure of goodness of fit. An example calibration curve is shown in Figure 4.2 along with maps of lowpass-filtered DN and α_{RDEM}.

4.2.4 Build DEMs by photoclinometry

After calibrating the constants A and B for each image, Equation 4.2 is rearranged to solve for sun-oriented surface slopes. We generate a surface from each image as the cumulative sum of surface gradients along each row of the sun-oriented image. At this point in the process, the initial DEM produced by photoclinometry is still rotated in the direction of the sun and its first column contains all zero-elevation values, because elevation was taken as the cumulative sum of surface gradients along each row, beginning with zero. It is possible to apply a scalar offset to each row by constraining a column of elevations to corresponding RDEM values; however, due to errors that are integrated in the surface building process, the scalar offset method results in horizontal corrugations that grow in amplitude with increasing distance from the constraining column. To minimize integrated errors and to tie DEMs to known large-scale topography we apply a 1D first-order highpass Butterworth filter with a cutoff wavelength of 25 km to each row of the DEMs, then add RDEM values which have been lowpass filtered to the same wavelength. As described in the Discussion section, the cutoff wavelength should be selected as the smallest value sufficient to capture the physical phenomena under investigation. The final step is to rotate each DEM back to standard polar stereographic orientation.

4.3 Measurement precision and accuracy

The method of DEM consruction presented in Section 4.2 results in a surface which may contain appreciable noise at small scales and offers no information about features larger than the prescribed cutoff wavelength. However, the long record available and dense temporal coverage of MODIS data make it possible to extract useful information about spatial variability of small-scale trends by analyzing many DEMs constructed by repeat photoclinometry. In this section we assess the characteristic uncertainty of surface elevation trends generated from a time series of photoclinometric DEMs and we compare to trend estimates obtained by laser altimetry over Totten Glacier.

4.3.1 Uncertainty estimation by least squares

For a time series of DEMs with the linear trend removed, we find that elevation values at any given location typically exhibit a normal distribution with standard deviation σ_z, indicating a least-squares trend line fit to N DEMs generated from images collected at times t will have a characteristic uncertainty σ_{trend} given by

$$\sigma_{\mathrm{trend}} = \sigma_z \sqrt{\frac{N}{N\Sigma t^2 - (\Sigma t)^2}} \tag{4.3}$$

(Taylor, 1997). Equation 3 tells us that while each elevation measurement is characterized by some constant uncertainty σ_z, uncertainty in the slope of the linear trend

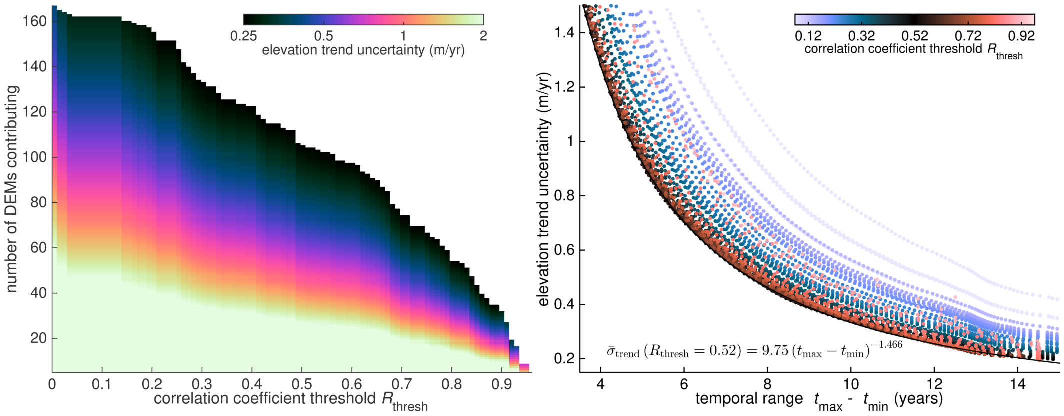

Figure 4.3: **Left:** A target level of uncertainty σ_{trend} can be attained by fitting a linear trend to many low-quality DEMs or fewer high-quality DEMs. This figure shows the average estimated trend uncertainty $\bar{\sigma}_{\text{trend}}$ for N consecutive DEMs meeting a correlation coefficient threshold R_{thresh}. **Right:** Uncertainty in local surface elevation trend decreases with increasing temporal range because more DEMs are included when fitting a trend line to each grid cell. Starting with 168 MODIS-generated DEMs of Totten Glacier, best results are obtained by applying a quality threshold $R_{\text{thresh}} = 0.52$, which limits the dataset to 121 DEMs. More stringent values of R_{thresh} increase uncertainty by reducing the number of DEMs contributing to an estimate, while relaxing R_{thresh} to values lower than 0.52 degrades the overall signal-to-noise ratio. A power-law fit to $\bar{\sigma}_{\text{trend}}\left(R_{\text{thresh}} = 0.52\right)$ is shown as a thin black curve.

σ_{trend} decays exponentially with increasing N. Due to variations in illumination conditions, sensor angle, surface conditions, and partial cloud cover in some images, noise level varies by DEM, but is closely related to the correlation coefficient R obtained in the calibration process described in Section 4.2.3. We use R as a proxy for DEM quality and explore the effects of limiting trend analysis to DEMs generated with R values exceeding a threshold R_{thresh}. Overall uncertainty $\bar{\sigma}_{\text{trend}}$ for a set of DEMs is taken as the mean σ_{trend} for all grid cells within the domain shown in Figure 4.2, except grid cells within 25 km from the DEM edges or coast, which have been masked out to eliminate any edge effects of filtering.

The left panel of Figure 4.3 shows the average $\bar{\sigma}_{\text{trend}}$ for all combinations of N consecutive DEMs meeting a given R_{thresh} generated from up to 168 MODIS images of Totten Glacier. For any given R_{thresh}, $\bar{\sigma}_{\text{trend}}$ decreases monotonically with increasing N because inclusion of more DEMs allows signal coherence to develop among self-canceling noise. Higher values of R_{thresh} can generate a target $\bar{\sigma}_{\text{trend}}$ with fewer contributing DEMs, but may require many years of data to accumulate a sufficient number of scenes meeting R_{thresh}. In practice, the most precise trend estimate possible for images collected in a limited time frame is not achieved by highly stringent quality control; rather, relaxing R_{thresh} toward a value of 0.5 allows the additive effects of more signal inclusion to outweigh any degradation from added noise. The right panel of Figure 4.3 shows that for any temporal range of analysis in this dataset, $R_{\text{thresh}} = 0.52$ is the optimum value which provides the lowest measurement uncertainty—higher values of R_{thresh} result in a dataset with less total signal whereas the signal in lower-quality DEMs is small and overwhelmed a high contribution of noise.

4.3.2 Validation with laser altimetry

An R_{thresh} of 0.52 applied to our dataset provides a 15 year record of 121 DEMs corresponding to a trend uncertainty of $0.22\,\mathrm{m\,a^{-1}}$. Using all 121 DEMs we resolve clear patterns of thinning aligned with visible channels near the deep western grounding line of Totten Glacier. On grounded ice we detect a nearby subglacial lake drainage event which was first observed by airborne laser altimetry (Young et al., 2015). To illustrate how our method compares to laser altimetry we must limit our dataset to the temporal range corresponding to the dates of complete repeat-track laser altimetry coverage over Totten Glacier. By limiting the number of DEMs contributing to the trend analysis we increase uncertainty, but small-scale surface features can change on rapid timescales, meaning the relatively high values of $\bar{\sigma}_{\mathrm{trend}}$ associated with reduced N do not preclude detection of change where the short-term rate of change is large.

Figure 4.4 shows small-scale surface elevation trends obtained from 62 MODIS images collected between September 19, 2003 and February 24, 2011. Patterns of localized surface elevation trends are evident and correspond primarily to advection of small-scale surface features on the floating ice shelf. Figure 4.5 shows a photoclinometry-derived elevation trend profile which we compare to laser altimetry trends along ICESat track 1312. Details of laser altimetry processing are provided in the Appendix. The laser altimetry trend profile has been highpass-filtered with a cutoff wavelength of 25 km to match the cutoff wavelength of the

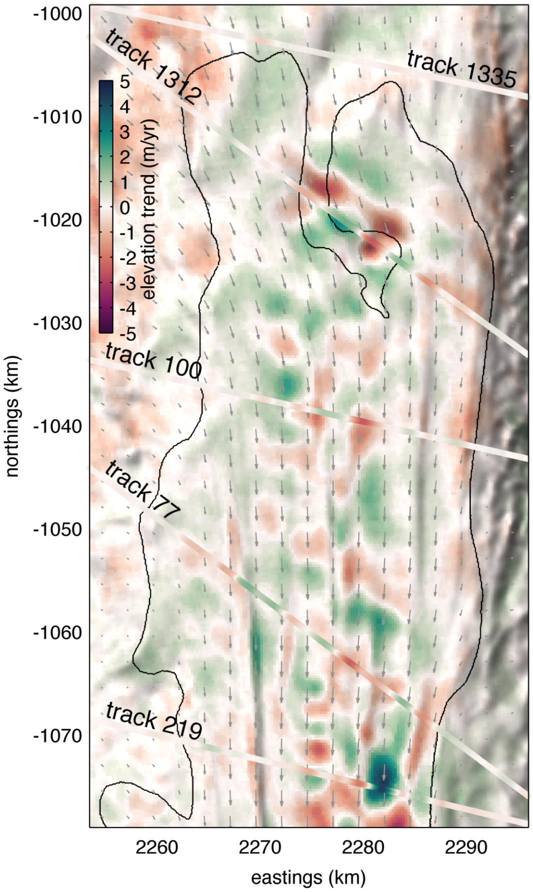

Figure 4.4: Repeat photclinometry can fill the large gaps between repeat tracks of laser altimetry. This map of small-scale surface elevation trends was generated from 62 MODIS images taken over 7.4 years. Elevation trends from five tracks of repeat laser altimetry have been highpass filtered to correspond to the detection limit of repeat photoclinometry. On this time scale, trends are dominated by surface feature advection, but patterns of channelized thickening and thinning are subtly visible. Longer records tend to bring persistent channelized signals into focus while reducing the effects of trends attributable to advection. Mismatch between repeat-track laser altimetry and repeat photoclinometry occurs primarily where the laser altimetry record does not span the full temporal range of satellite imagery contributing to the underlying trend map. For context, relief shading is applied to the mean of the 62 contributing DEMs. A profile of track 1312 is presented in Figure 4.5 and a timeline of data contributing to this map is given in Figure 4.6. Surface velocity vectors are from InSAR (Rignot et al., 2011b, 2017).

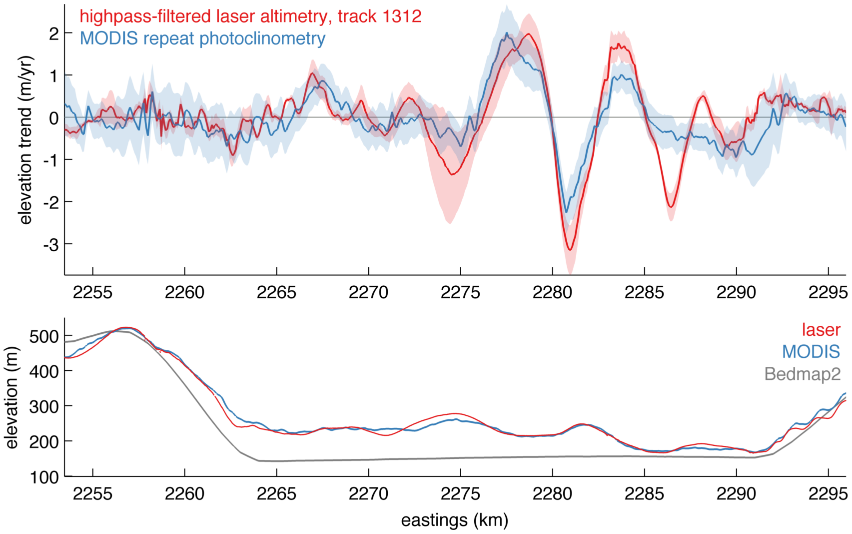

Figure 4.5: Surface elevation trends measured by repeat photoclinometry agree with laser altimetry observations within the shaded regions of uncertainty estimated by Equation 4.3 for both measurement types. The large-magnitude trends between 2273 and 2285 km easting would be difficult to interpret by laser altimetry alone, but the surrounding pattern observed by repeat photoclinometry suggests a link to changes in basal shear stress. Absolute elevations are shown from the airborne ICECAP laser altimeter, the mean of 62 photoclinometry DEMs for which trend analysis was performed, and Bedmap2.

photoclinometry DEMs. To be clear, we validate surface elevation trends obtained by repeat photoclinometry using the same laser altimetry dataset we used to adjust the RDEM by which the Equation 2 was calibrated. However, RDEM is a static surface lowpass filtered to a wavelength of 46 km for calibration, whereas the laser altimetry trends we use for validation provide time-varying information only on scales shorter than 25 km. In effect, the laser altimetry contribution to the calibration process is independent of the laser altimetry contribution to the validation discussed here.

By laser altimetry alone, the elevation trend along track 1312 would be difficult to interpret, but repeat photoclinometry offers spatial context. The pattern seen in Figure 4.4 resembles observations at Pine Island Glacier (Joughin et al., 2016) and suggests a link to changes in basal shear stress (Gudmundsson et al., 1998; Gudmundsson, 2003) associated with Totten Glacier's recent grounding line migration (Li et al., 2015).

Small-scale trends measured by repeat photoclinometry along track 1312 agree within uncertainty estimates despite sparse laser altimetry coverage that does not span the full 7.4 years of MODIS data used for this comparison. The major difficulty in comparing laser altimetry to repeat photoclinometry is that each satellite image covers the entire spatial domain, while a spatial distribution of trends from laser altimetry can only be created by piecing together hyper-local trends measured at different times, with a variable number of observations available at each posting. Figure 4.6 illustrates the asynchronous nature of turning incomplete laser altimetry coverage into an apparent snapshot of spatially-distributed elevation trends, and

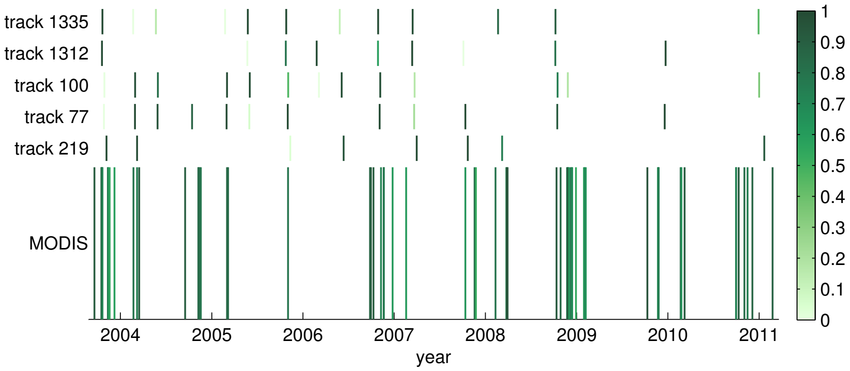

Figure 4.6: Elevation trend maps generated from laser altimetry are inherently based on asynchronous and incomplete data coverage, whereas repeat photoclinometry covers large areas with each measurement. The trend map presented in Figure 4.4 was generated from data of varying quality collected at scattered times. Data collection dates are indicated by vertical bars with color scaled as a measure of data quality—for repeat tracks of laser altimetry, color corresponds to the fraction of postings in the domain containing valid data while MODIS bars are color-scaled by their R value obtained in calibrating each image to known large-scale topography.

may explain some of the discrepancies we see between laser altimetry and repeat photoclinometry.

4.4 Discussion

Our observations support modeling efforts that have found the coarse spacing of ICESat repeat tracks is insufficient to capture the glaciological processes that control ice flow, and can lead to significant miscalculation of large-scale thinning rates (Sergienko, 2013).

By the method presented in this paper, σ_{trend} is inversely related to the cutoff wavelength of the 1D filter applied in Section 4.2.4; consequently, a cutoff wavelength shorter than 25 km would reduce the uncertainty values seen in Figure 4.3 but would preclude detection of larger-scale phenomena. To minimize uncertainty, the cutoff wavelength should be chosen as the shortest wavelength possible to capture the surface elevation changes under investigation.

By establishing a direct relationship between pixel brightness and surface slope for individual images, we eliminate the need to rely on laboratory values of sensor calibrations; we minimize assumptions regarding the reflectance properties of local snow, which can vary with temperature, snow age, and illumination angle (Steffen, 1987; Kuipers Munneke et al., 2008); and we minimize the impact of multiple scattering between snow and atmosphere (Aoki et al., 1999; Mousivand et al., 2015). But despite the gains made by tailoring the transfer function between known large-scale surface slopes and pixel brightness for each image, not all images are adequate for DEM generation.

Photoclinometry is limited first by long, dark polar nights and second by persistent cloud cover in many coastal regions. Where a sufficient number of well-lit, cloud-free images are available for small-scale trend analysis, photoclinometry may still be complicated by the presence of nunataks, blue ice, surface frost, surface water, wet snow, crevassing, dust cover, surface debris, or sensor saturation. Regions of an image where pixel brightness is not directly related to surface slope can be masked before performing the brightness-to-slope calibration; however, masking introduces a complication when integrating across discontinuous pixels to build a DEM. In this work, we did not give special treatment to subregions within the domain because snow grain size is relatively uniform in the Totten region (116 ± 20 um (Scambos et al., 2007; Haran et al., 2014a)) and should result in slope errors of less than 0.2° (Kuipers Munneke et al., 2008). The uniformity of albedo is reflected in the linear nature of the relationship between surface slope and DN, and is included in the correlation coefficient R. By only considering DEMs whose R value exceeds R_{thresh}, DEMs are excluded if the linear relationship breaks down.

The method we present is limited to large, uninterrupted regions of uniform albedo with known large-scale topography, but computational requirements are low and measurement uncertainties are well constrained. Photoclinometry performs best in the nearly featureless environments which often cause stereo photogrammetry to fail, but suffers in high-contrast environments where stereo photogrammetry excels. Small-scale elevation trends obtained by repeat photoclinometry can be readily blended with large-scale trends obtained by other altimeters (e.g., (Paolo et al., 2016)) to construct high-resolution maps of absolute elevation change. Our method does not require a great deal of human expertise or interpretation; rather, after discarding cloud-contaminated images and tuning the cutoff wavelength to capture processes of interest, the surface elevation trend measurement technique and uncertainty estimations can be automated.

Until now, the vast majority of polar satellite images have been left unused because they do not meet stringent requirements for conventional photoclinometry. In them we find small, but detectable signals which are fit for science and need not be discarded. By assessing trends in high-noise photoclinometry-derived DEMs we are able to resolve and quantify small-scale processes which are directly linked to large-scale ice sheet dynamics.

Chapter 5

Seasonal dynamics of Totten Ice Shelf

Previous studies of Totten Ice Shelf have relied upon surface velocity measurements to investigate its mass balance and sensitivities to interannual climate forcing. However, short-term displacement measurements may not accurately characterize long-term flow rates where ice velocity fluctuates with the seasons. Quantifying annual mass budgets or analyzing interannual changes in ice velocity requires knowing when, whether, and where observations of glacier velocity may be aliased by short-term variability. Here, we analyze 16 years of velocity data for Totten Ice Shelf, which we generate at sub-annual resolution by applying feature tracking algorithms to several hundred MODIS satellite image pairs. We find the ice shelf is characterized by a seasonal cycle of spring to autumn speedup of more than 100 m/yr close to the ice front. The amplitude of the seasonal cycle diminishes with distance from the open ocean, suggesting the presence of a resistive backstress at the ice front that reaches a maximum in winter. Springtime acceleration precedes summer surface melt and is not attributable to thinning from basal melt. We find

---

The contents of this chapter are currently in preparation for publication. The work presented here was conceived of and carried out primarily by the author of this dissertation.

that the ice shelf accelerates each spring in response to lost buttressing from the breakup of seasonal landfast sea ice.

5.1 Introduction

Totten Glacier in East Antarctica drains the Aurora Subglacial Basin, which is grounded well below sea level (Young et al., 2011) and contains enough ice to raise the global sea level by at least 3.5 m (Greenbaum et al., 2015). Short-term observations have identified Totten Glacier and its ice shelf (TIS) as thinning rapidly (Pritchard et al., 2009, 2012) and losing mass (Chen et al., 2009), but longer-term observations paint a more complex picture of interannual variability (Paolo et al., 2015; Li et al., 2016; Roberts et al., 2017; Greene et al., 2017a). The current best estimates of Totten Glacier and TIS mass budgets have been calculated using a mosaic of surface velocity measurements collected at different times throughout the year (Rignot et al., 2013), but the underlying assumption of steady ice flow has not been validated. It is possible that common methods of velocity measurement are aliased by subannual fluctuations and may not be suitable for investigations of steady state mass balance or interannual changes in ice shelf velocity. Furthermore, many common methods of velocity measurement, such as satellite image feature tracking or in-situ GPS measurements taken over the course of a field season, are strongly biased toward summer acquisition and may present an inaccurate measure of annual ice discharge. Wherever seasonal velocity variability exists, it is important to consider how ice velocity is measured, and how the measurements can be interpreted.

Seasonal variations in glacier velocity have been observed in Greenland and Antarctica (e.g., Joughin et al., 2008; Moon et al., 2014; Fahnestock et al., 2016), and have been attributed to a number of different mechanisms. On grounded ice, surface meltwater can drain into crevasses or moulins, make its way to the bed, pressurize inefficient subglacial hydraulic systems, and allow the glacier to speed up until pressure is reduced (Sohn et al., 1998; Bartholomew et al., 2010; Moon et al., 2014). On floating ice, surface meltwater may also influence ice shelf velocity by percolating through and weakening the ice shelf shear margins (Liu and Miller, 1979; Vaughan and Doake, 1996). Observations have shown correspondence between seasonal advance and retreat of marine-terminating glaciers and the presence of ice melange at the glacier terminus (Howat et al., 2010). Modeling studies have shown that the back stress provided by sea ice can be sufficient to completely shut down calving (Robel, 2017) and have an appreciable effect on glacier velocity (Todd and Christoffersen, 2014; Krug et al., 2015). At Store Glacier in Greenland, the buttressing stress of sea ice has been estimated at 30–60 kPa, which is an order of magnitude below the driving stress of the glacier, but is sufficient to produce observable changes in velocity (Walter et al., 2012; Todd and Christoffersen, 2014).

In Antarctica, marine ice is known to strengthen the Brunt and Stancomb-Willis ice shelf system (Hulbe et al., 2005), and an ice shelf acceleration event observed there in the 1970s has been attributed to a reduction in stiffness of the ice melange that connects the two ice shelves. Similarly, landfast multi-year sea ice is strongly mechanically coupled to Mertz Glacier Tongue (Massom et al., 2010) and may have delayed a major calving event that occurred there in 2010 (Massom et al., 2015). Closer to TIS, two recent major calving events that each affected several glaciers in Porpoise Bay (76°S,128°E) have been attributed to the breakup of landfast sea ice at the ice shelf termini (Miles et al., 2017). To our knowledge, there have been no reports of seasonal variability of TIS or any connection between sea ice at its front and TIS dynamics.

5.2 Surface velocity observations

For this work, we analyzed surface velocity time series using feature tracking algorithms applied to MODIS and Landsat 8 images. The MODIS and Landsat 8 images were processed separately, using different feature tracking programs, and the resulting time series represent two independent measures of TIS velocity. The MODIS record contains several images per year from 2000 to present; however, the 250 m spatial resolution of MODIS images limits measurement accuracy where ice displacements are small between images. The 15 m resolution of Landsat 8 permits more accurate velocity measurements of slow-moving ice over short time intervals, but the relatively short Landsat 8 record provides lower confidence in the separation of interannual variability from seasonality.

5.2.1 GoLIVE velocity data

With the 2013 launch of Landsat 8 and the development of new algorithms to perform rapid feature tracking (Fahnestock et al., 2016), sub-annual ice velocity time series are now available in near-real-time for most of the world's ice-covered regions (Scambos et al., 2016). We used the Global Land Ice Velocity Extraction from Landsat 8 (GoLIVE) dataset (Scambos et al., 2016; Fahnestock et al., 2016), which is processed at 600 m resolution for most of Antarctica. We analyzed the high-confidence `vx_masked` and `vy_masked` velocity fields from late 2013 to early 2017 and limited the dataset to 123 image pairs separated by $16 \leq dt \leq 112$ days. Many of the image pairs overlap in time, providing several redundant, semi-independent velocity measurements, particularly throughout the summer months when each image may contribute to multiple image pairs.

To better understand the spatial pattern of TIS seasonality, we calculated separate velocity maps for spring and autumn. Spring velocity was taken as the mean of 61 velocity measurements whose image pairs were obtained between June 16 and December 15. Autumn velocity was calculated as the mean of 62 velocity fields in within the remainder of the year. The difference between spring and autumn velocities is shown in Figure 5.1.

The terminal ∼50 km of TIS exhibits an annual flow acceleration from spring to autumn and subsequent slowdown from autumn to spring. Seasonality is strongest close to the glacier terminus and decays with distance from the open ocean. The pattern is similar to the 2010−2009 InSAR-derived velocity difference reported by Li et al. (2016), which may reflect a difference in timing or magnitude of the 2009 and 2010 seasonal accelerations. Grounded ice of the eastern tributary accelerates slightly throughout the summer and the seasonal signal reaches at least 20 km upstream of the grounding line. Farther from the open ocean, the inner TIS shows a weak seasonal cycle that has the opposite phase of outer TIS velocities; however, the nearly featureless nature of the inner TIS surface greatly reduces the

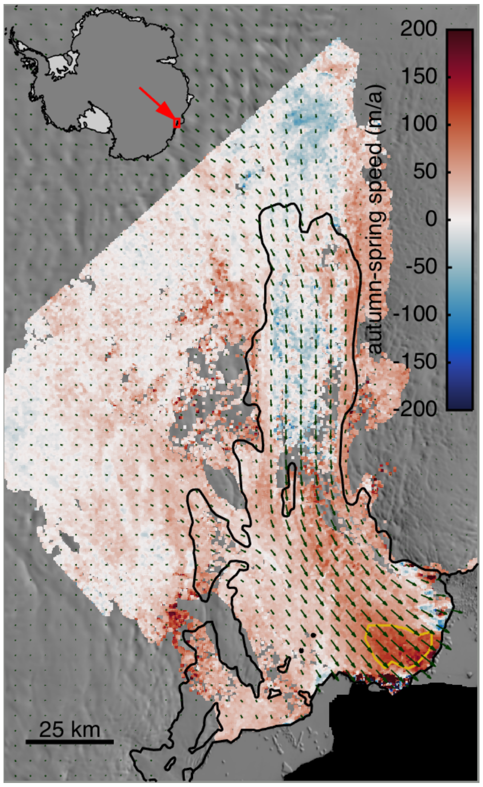

Figure 5.1: Toward the ice front, autumn velocity exceeds spring velocity by more than 100 m/yr. This image shows the difference between the mean of 62 spring (centered on September 15) and 61 autumn (centered on March 15) GoLIVE velocity fields. Green vectors indicate the mean velocity, supplemented by MEaSUREs (Rignot et al., 2011c) InSAR-derived velocity outside the range of Landsat path 102, row 107. A time series of the mean of velocities within the gold polygon is shown in Figure 5.2.

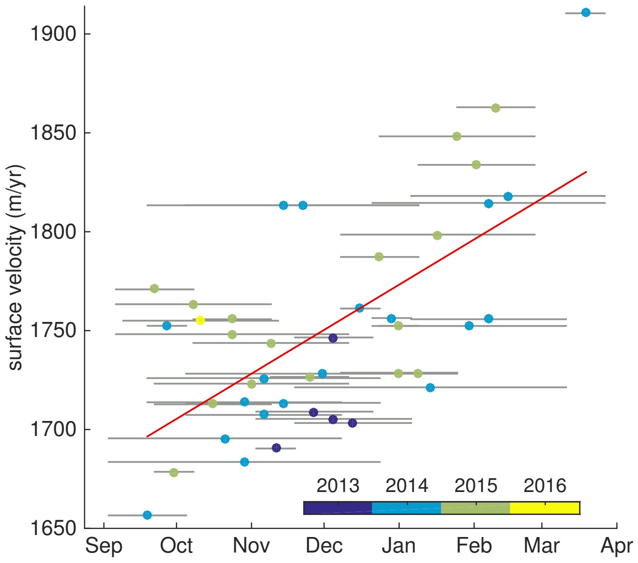

Figure 5.2: The GoLIVE dataset contains many overlapping TIS velocity measurements captured between September and April of each year. The velocities here are the mean of all measurements within the gold polygon shown in Figure 5.1. The red line is a linear least-squares fit to the observations, indicating a typical spring-to-fall acceleration of 0.8 m/yr per day.

number of high-confidence velocity measurements available and uncertainties here are high.

Figure 5.2 shows a time series of the summer acceleration of velocity measurements close to the TIS front. The short record of the GoLIVE dataset inhibits assessment of the timing of the onset of acceleration, but a linear trend fit to all available measurements indicates an typical acceleration of approximately 0.8 m/yr per day from late September to early April.

5.2.2 MODIS velocity data

A MODIS velocity time series was generated from 561 pairs of MODIS images (Scambos et al., 2001, updated 2017) obtained between 2002 and 2017. Each image pair was separated by 92 to 182 days and was processed at 500 m resolution using the ImGRAFT template matching software (Messerli and Grinsted, 2015) with Antarctic Mapping Tools for MATLAB (Greene et al., 2017b). The present work represents a reprocessed and extended form of the MODIS dataset described by Greene and Blankenship (in press), which has previously been processed for investigations of interannual change by Greene et al. (2017a).

Figure 5.3 shows a time series of the TIS velocity averaged between 20 and 40 km from the TIS front. A one-year moving average has been removed to retain only subannual velocity anomalies. Because no MODIS band 2 images are available during the dark winter months, no image pairs separated by 92 to 192 days are centered on any days in April, May, August, or September. However, 46 image pairs span the winter, providing velocity measurements centered on June and July. A sinusoid fit to the 561 measurements is characterized by an amplitude of 117 m/yr, a maximum on March 21, and a minimum on September 19. The sinusoid matches observations with a root-mean-square error of 95 m/yr.

5.3 Surface melt

In Greenland, surface melt has been linked to glacier velocity acceleration where surface water drains to the bottom of the ice sheet, alters the basal water

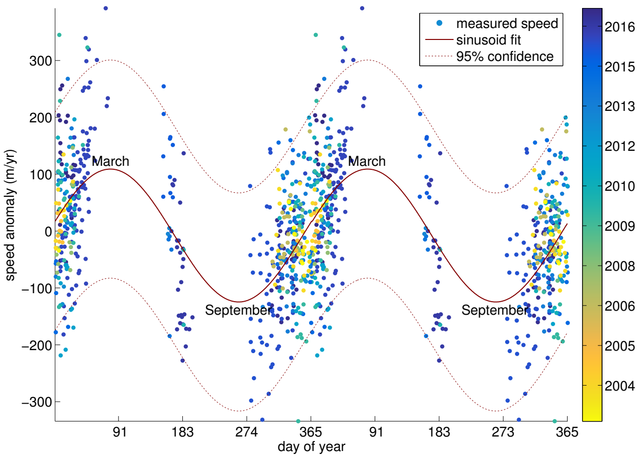

Figure 5.3: Velocity anomalies from 561 MODIS image pairs separated by 92 to 182 days. A one-year moving average has been removed for improved interannual comparison. The time series is replicated, showing two years of data for visual continuity. Values shown are the mean of all measurements within the green polygon shown in Figure 6.1.

pressure, and allows the overlying ice to accelerate (Zwally et al., 2002; Schoof, 2010; Bartholomew et al., 2010). The seasonal velocity anomalies we observe at TIS are strongest near the ice front and do not appear to be driven by grounded ice processes, so it is unlikely that the seasonal variability of TIS velocity is driven by subglacial hydrology on nearby grounded ice. However, the presence of liquid water within ice is known to weaken ice (Liu and Miller, 1979), and several ice shelves around the Antarctic Peninsula have dramatically responded to atmospheric warming with major breakup events resulting from surface meltwater-induced hydrofracture (Doake and Vaughan, 1991; Vaughan and Doake, 1996; Scambos et al., 2009; Banwell et al., 2013). TIS experiences ∼10 days of surface melt each year, and thus it is possible that meltwater could percolate into the ice, weaken the ice

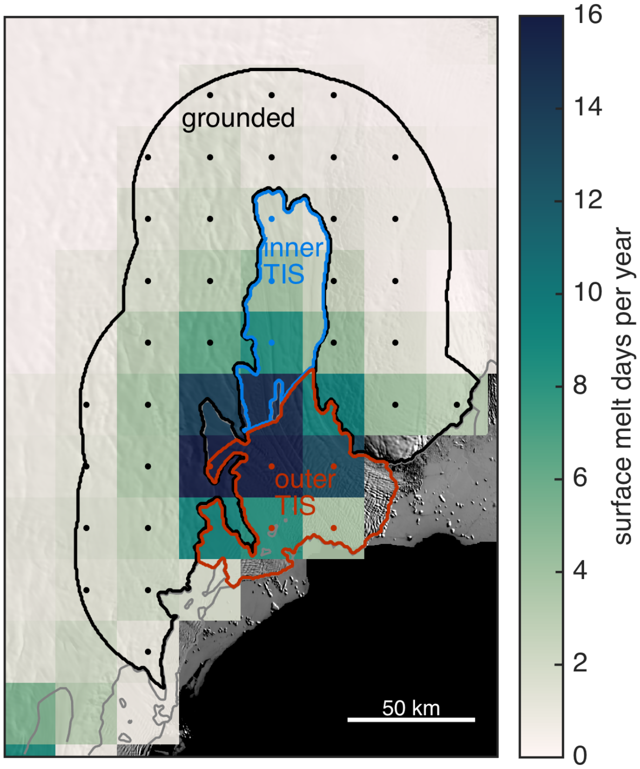

Figure 5.4: Mean surface melt from Picard and Fily (2006).

shelf shear margins, and allow the ice shelf to speed up as a result of reduced buttressing.

To assess the possible link between TIS velocity anomalies and surface melt, we use daily observations of surface melt from passive microwave radiometers (SMMR and SSM/I) gridded to 25 km resolution (Picard and Fily, 2006). We limit the period of analysis to 2000 through 2015 to roughly coincide with available MODIS image data. Figure 5.4 shows the spatial distribution of mean annual surface melt. Using the masks developed by Mouginot et al. (2016) with the Antarctic Mapping Tools for MATLAB `dist2mask` function (Greene et al., 2017b), we define three subdomains of surface melt analysis as

1. *Outer TIS:* the floating portion of the ice shelf up to 50 km from the ice shelf front,
2. *Inner TIS:* the floating portion of the ice shelf more than 50 km from the ice shelf front, and
3. *grounded:* all grounded ice within 50 km of the TIS grounding line.

Up to 16 days of surface melt occur per year in the outer TIS, while fewer days of surface melt are observed farther from the ice front or on grounded ice. For the full 16 year record, Figure 5.5 shows that although the outer TIS experiences much more surface melt than the inner TIS or surrounding grounded ice, the timing of surface melt is roughly the same in all three subdomains, with the typical melt season lasting from December to February. For the outer TIS, the onset of surface melt typically occurs on December 23 ($\pm 1\sigma = 12$ days), with the earliest surface melt of any season recorded December 6, 2006. The mean final day of surface melt occurs on January 23 ($\pm 1\sigma = 9$ days), but has been observed as late as February 11 in 2005.

5.4 Basal melt

Both TIS and West Antarctica's Pine Island Ice Shelf have exhibited velocity variability in response to interannual changes in ice shelf thickness (Christianson et al., 2016; Greene et al., 2017a). For these laterally-bounded ice shelves re-

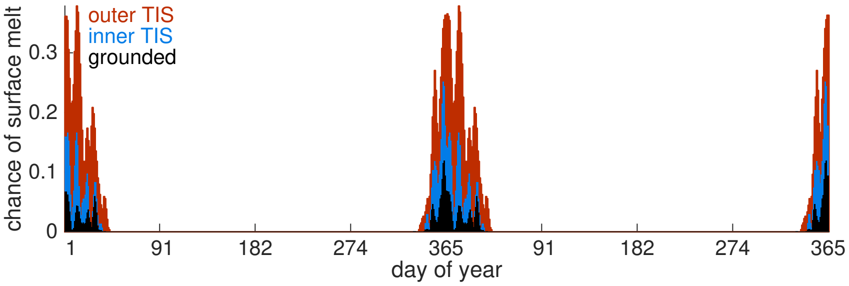

Figure 5.5: Probability of surface melt in each of the three subdomains shown in Figure 5.4. Low-elevation areas near the coast experience more days of surface melt than high-elevation grounded ice, but the timing of surface melt is roughly the same throughout the domain. The time series is intentionally repeated above, showing two years for visual continuity.

strained largely by shear stress at their margins, thinning reduces resistance to flow and allows ice shelf acceleration. To assess whether this mechanism acts on TIS at sub-annual timescales, we used the Regional Ocean Modeling System (ROMS; Shchepetkin and McWilliams, 2005) to simulate ocean-ice shelf interaction at TIS.

A terrain-following vertical coordinate provides enhanced resolution close to the seafloor and ice shelf interface. Modifications to the code allow thermodynamic interaction between ocean and ice, following Dinniman et al. (2003). Seafloor topography is based on the RTOPO dataset (Timmermann et al., 2010), while cavity geometry is inferred, assuming ice elevation (from ICESat) above flotation and a constant 300 m thick offset along the central flow line. Between the central flow line and the grounding line, cavity bathymetry is linearly interpolated. The model lateral and surface boundaries are forced over the hindcast period 1992-2012. Lateral forcing is derived from the ECCO2 cube92 reanalysis solution (Menemenlis et al., 2008); surface forcing is ERA-interim wind stress (Dee

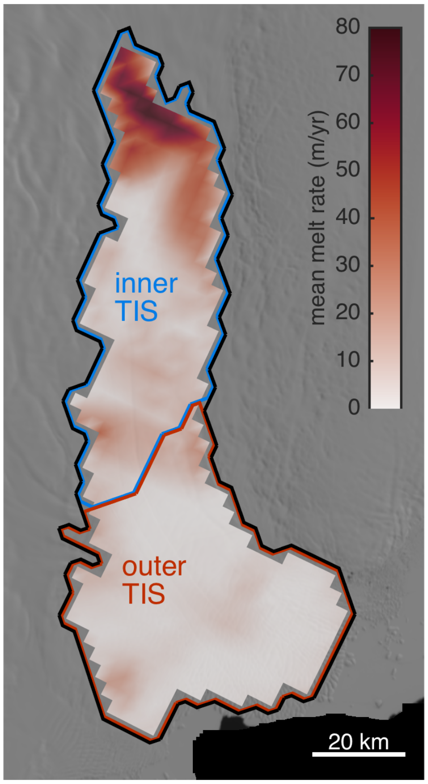

Figure 5.6: Modeled mean melt rate distribution of TIS. Melt is focused where ice is deepest, exceeding 80 m/yr near the grounding line of the inner TIS. Melt anomalies propagate in a clockwise fashion around the cavity, with a characteristic circulation time of roughly three weeks (not shown).

et al., 2011) and heat and salt fluxes derived from Special Sensor Microwave/Imager (SSM/I) algorithms for sea-ice production (Tamura et al., 2016). The model was spun-up for 21 model years using 1992–2012 forcing. After spin-up, the 1992–2012 forcing was repeated and we analyze the mean seasonal cycle of melt from the second run. The mean spatial distribution of melt throughout the year is shown in Figure 5.6.

Figure 5.7 shows the time series of modeled melt rates for each subdomain

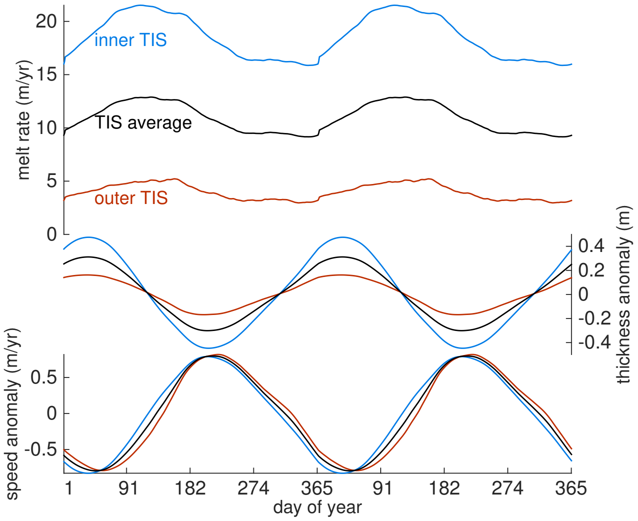

Figure 5.7: Two years of 1992–2012 climatological average melt rates from ROMS, for the TIS subdomains shown in Figure 5.6. Ice thickness anomalies from integrated melt rate anomalies show a small <1 m sub-annual change in thickness, which is expected to result in a <1 m/yr spring velocity anomaly.

in Figure 5.6. The deepest ice of the inner TIS exhibits the highest average melt rate and largest seasonal cycle of melt, whereas the shallow ice of the outer TIS experiences only modest basal melt. Using the model given by Greene et al. (2017a) (see also Joughin et al. (2004)) to estimate velocity anomalies from seasonal changes in ice thickness, we find that TIS seasonal basal melt anomalies should produce only slight changes in TIS velocity on the order of 1 m/yr. Somewhat by coincidence, the large ($>$ 8 m/yr) difference between summer and fall melt rates in the inner TIS where the ice thickness exceeds 2000 m should affect local ice velocity to roughly the same degree as the much smaller ($\sim$ 3 m/yr) seasonal melt rate variability in the outer TIS where ice is much thinner.

The model we use to estimate melt-induced velocity anomalies assumes TIS velocity is limited only by lateral shear stress at the ice shelf margins and velocity anomalies are a function only of local ice thickness. These assumptions vastly oversimplify the complex stress regime of the TIS, but are used to obtain an order-of-magnitude approximation of how the TIS should respond to seasonal variability of ice thickness related to basal melt. By this model, the <1 m/yr velocity variability resulting from basal-melt-related changes in ice thickness is not sufficient to explain the >100 m/yr variability of TIS velocity we observe. Moreover, the melt-induced TIS thickness reaches a maximum in late February, and should correspond to a velocity minimum at that time; yet, this is precisely when TIS velocity nears its maximum. Thus, it is unlikely that the seasonal cycle of basal melt could explain the seasonal cycle of TIS velocity we observe.

5.5 Sea ice

To assess whether sea ice may influence the flow of TIS, we use sea ice concentrations from the Scanning Multichannel Microwave Radiometer (SMMR), the Defense Meteorological Satellite Program (DMSP) -F8, -F11 and -F13 Special Sensor Microwave/Imagers (SSM/Is), and the DMSP-F17 Special Sensor Microwave Imager/Sounder (SSMIS) (Cavalieri et al., 1996). For 2000–2016, we analyzed the daily time series of the mean of three 25 km resolution grid cells near the TIS front (Figure 5.8). We also visually inspected 315 cloud-free MODIS visual band 2 and 164 thermal band 32 images (Scambos et al., 2001, updated 2017; Greene and Blankenship, in press) to assess the annual cycle of sea ice consolidation near the TIS front.

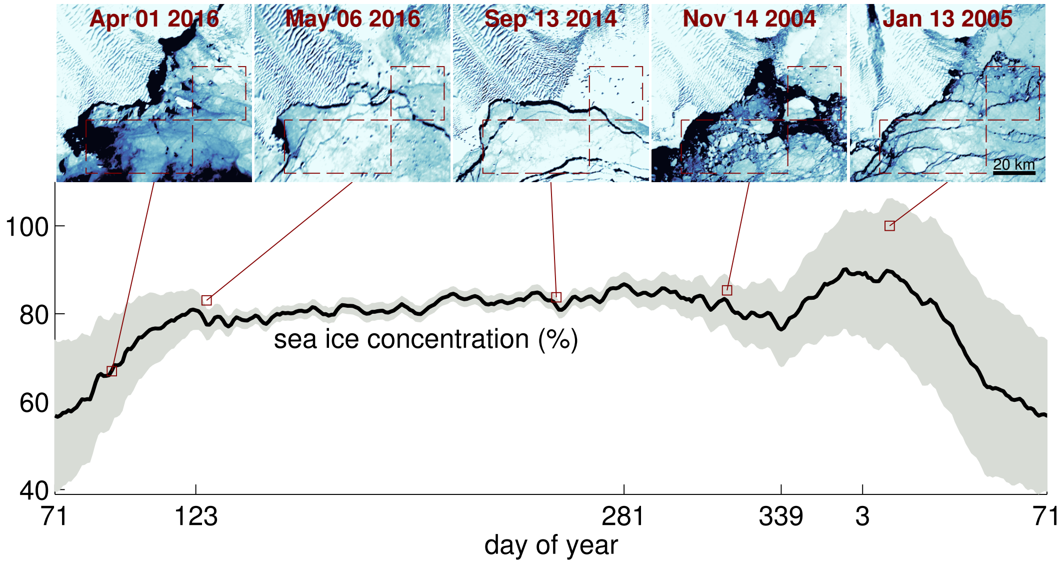

Figure 5.8: Mean annual cycle of sea ice concentration from 2000–2016 passive microwave data (Cavalieri et al., 1996). The time series begins on day 71 (March 12) to correspond to the typical sea ice minimum. Fast ice forms on or about day 123 (May 3) and begins to break up on or about day 281 (October 8). On day 339 (December 5) begins to form again and reaches a maximum on January 3. Shading in the time series indicates $\pm 1\sigma$. Five example MODIS images (Scambos et al., 2001, updated 2017) are shown for context, with dashed quadrangles indicating the region of ice concentration averaging.

Figure 5.8 shows the characteristic annual cycle of sea ice activity near the TIS front. A minimum concentration of sea ice typically occurs in mid March, corresponding to the final days of summer when surface air temperatures are above freezing (Dee et al., 2011). Sea ice grows rapidly throughout April and appears to become fastened to the western TIS front by early to mid May. The rigid connection of landfast ice to the western TIS front holds throughout the winter, although inspection of thermal band MODIS images suggests a small area of the polynya that abuts Law Dome (see Alley et al. (2016)) may briefly open some years in July. Regardless of polynya activity, the majority of landfast ice remains connected to the TIS front until October. Each year the landfast connection breaks in October or early November, followed by a visible reduction in sea ice cover that occurs throughout November. Although air temperatures typically remain above freezing from late spring through summer, the decline of sea ice is interrupted most years as unconsolidated sea ice temporarily fills the embayment and reaches a maximum concentration in early January. From January to March, sea ice melts or is exported out of the embayment until concentration reaches a minimum in mid March, then the cycle is repeated.

Comparing visual band MODIS images to concurrent sea ice concentration data from the passive microwave sensor, it apparent that the available sea ice concentration data cannot be used alone to assess the strength of the landfast connection with the TIS front. Passive microwave data assess the mere presence of ice by inferring a mean skin temperature, and thus can only serve as a rough proxy for the strength of ice consolidation within a grid cell. Furthermore, no cells in the sea ice

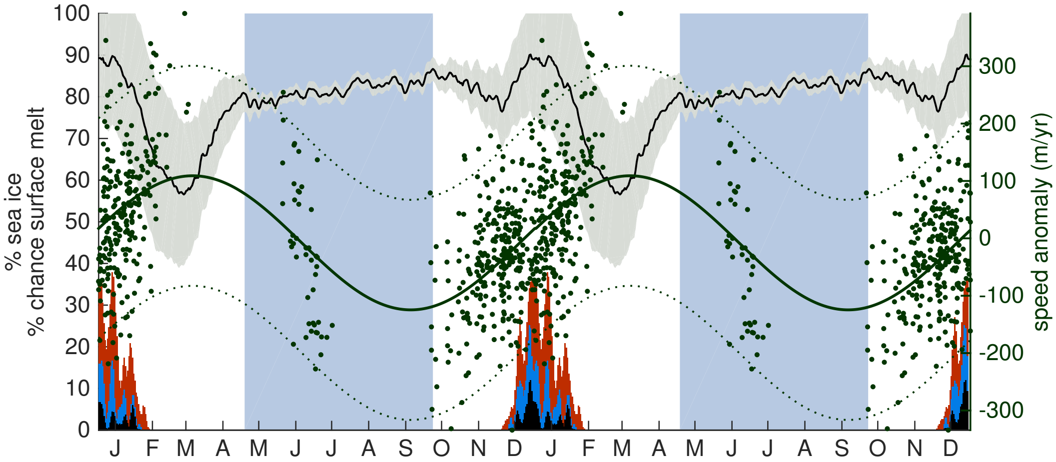

Figure 5.9: The springtime acceleration of TIS begins with the breakup of landfast sea ice and continues through the summer, possibly enhanced by shear margin weakening from surface melt. Shaded blue areas indicate typical times of landfast ice connection with TIS. The black line is sea ice concentration repeated from Figure 5.8; histograms show probability of surface melt from Figure 5.5. Velocity anomalies predicted from basal melt are not shown here becuase the ±1 m/yr amplitude would appear to be a flat line at this scale.

concentration grid overlie the TIS front; thus, the sea ice concentration data do not provide a direct measure of the connection strength between landfast ice and the TIS front.

5.6 Discussion

The spatial pattern of the annual TIS acceleration implies that it is governed by processes at the ice front. The timing of the acceleration implicates the annual breakup of landfast ice at the TIS front as an influencing factor. Figure 5.9 shows the relationship between sea ice concentration, surface melt, and TIS velocity. If the ice shelf is restrained by rigid landfast ice in winter and begins to accelerate upon the initial loss of the landfast ice connection in the spring, it is possible that surface melt may lead to weakened shear margins and continued acceleration later in summer or into the autumn.

The seasonal cycle of TIS velocity is unlikely to be as simple as a sinusoid, and the timing and magnitude of spring-to-autumn speedup undoubtedly vary from year to year. Nonetheless, we have shown that the ice shelf does respond to environmental forcing on sub-annual timescales, the response is significant, and it occurred in every year of our observations. This seasonal variability must be considered when interpreting velocity measurements obtained over periods that are not integer multiples of a year. Specifically, observations that are biased toward the summer months such as the GoLIVE may not provide an accurate representation of annual ice shelf velocity. MEaSUREs Annual Antarctic Ice Velocity Maps 2005–2016 (Mouginot et al., 2017a,b) have also recently been made available for assessment of interannual variability, but each year of data is generated from measurements obtained at different times throughout the year. The times of observations are not directly available to the user, but it is suggested that users consider the count and standard deviation of measurements contributing to each pixel before interpreting interannual changes.

A number of previous studies have investigated the causes interannual variability of TIS velocity, and have relied on measurements of TIS velocity taken over discrete intervals. Li et al. (2016) used subannual velocity observations to investigate long-term velocity variability in the eastern tributary of Totten Glacier where we observe a weak seasonal signal; however, their primary findings are based on the flow of the deep western tributary, where we detect no significant annual cycle. A similar study by Roberts et al. (2017) investigated interannual variability of TIS velocity using Landsat image pairs separated by near-integer multiples of years, and thus, each season is equally represented in each image pair. Well-timed surface velocity observations used in previous studies of TIS dynamics have led to robust findings, and future work must consider the seasonal cycle of TIS when interpreting velocity measurements.

Chapter 6

Wind causes Totten Ice Shelf melt and acceleration

Totten Glacier in East Antarctica has the potential to raise global sea level by at least 3.5 m, but its sensitivity to climate change has not been well understood. The glacier is coupled to the ocean by Totten Ice Shelf, which has exhibited variable speed, thickness, and grounding line position in recent years. To understand the drivers of this interannual variability, we compare ice velocity to oceanic wind stress and find a consistent pattern of ice shelf acceleration 19 months after upwelling anomalies occur at the continental shelf break nearby. The sensitivity to climate forcing we observe is a response to wind-driven redistribution of oceanic heat and is independent of large scale warming of the atmosphere or ocean. Our results establish a link between the stability of Totten Glacier and upwelling near the East Antarctic coast, where surface winds are projected to intensify over the next century as a result of increasing atmospheric greenhouse gas concentrations.

The contents of this chapter have been published as C. A. Greene, D. D. Blankenship, D. E. Gwyther, A. Silvano, and E. van Wijk. Wind causes Totten Ice Shelf melt and acceleration. *Science Advances*, 3:e1701681, 2017a. doi: 10.1126/sciadv.1701681. The work presented here was conceived of and carried out primarily by the author of this dissertation.

6.1 Introduction

Totten Glacier drains a 550,000 km^2 ice basin whose base lies primarily below sea level (Young et al., 2011), indicating potential vulnerability to rapid collapse (Weertman, 1974; Schoof, 2007). The grounding line where Totten Glacier goes afloat to form Totten Ice Shelf (TIS) has recently retreated (Li et al., 2015) while the ice shelf velocity and terminus position have been unstable (Li et al., 2016; Roberts et al., 2017; Miles et al., 2016). The TIS surface showed a dramatic lowering trend from 2002 to 2008 (Pritchard et al., 2012; Rignot et al., 2013) which continued through at least 2012 in the grounded part of the glacier (Young et al., 2015), but longer records of TIS surface elevation suggest sub-decadal trends may only represent part of a longer-term variability (Paolo et al., 2015; Roberts et al., 2017).

Observed changes in TIS are thought to be driven by a variable supply of warm, salty, modified circumpolar deep water (mCDW) (Rignot and Jacobs, 2002; Li et al., 2016; Miles et al., 2016) which can access the water cavity below TIS through a network of bathymetric troughs (Greenbaum et al., 2015). Ship-based observations have repeatedly shown a presence of mCDW along the outer continental shelf (Wakatsuchi et al., 1994; Bindoff et al., 2000; Williams et al., 2011; Nitsche et al., 2017), and a recent survey confirmed the ability of mCDW to traverse the continental shelf and fill the troughs near the TIS ice front (Rintoul et al., 2016; Silvano et al., 2017). Ocean models have linked interannual variability of the TIS melt rate to sea ice production, which generates cold, dense water that has the potential to displace mCDW and quench melt (Khazendar et al., 2013; Gwyther et al., 2014); however, no such cold, dense water was detected at the time of the only survey conducted on the continental shelf (Rintoul et al., 2016; Silvano et al., 2017, 2016). Observations and models both suggest the TIS melt rate is modulated by a variable supply of mCDW, but the mechanism driving mCDW exchange across the continental shelf break has not yet been explained, and until now, no links between forcing mechanisms and TIS response have been directly observed.

Insights into the drivers of TIS variability may lie in West Antarctica, where similar behaviors observed at Pine Island Ice Shelf have been hypothesized as resulting from a variable supply of circumpolar deep water, forced onto the continental shelf by wind processes at the shelf break (Wåhlin et al., 2013; Dutrieux et al., 2014; Webber et al., 2017; Kim et al., 2017).

We investigate the causes of recent TIS acceleration and deceleration by comparing a 14 year time series of ice-shelf velocity to oceanic surface wind stress. We use ice surface velocity as a proxy for melt-driven ice thickness change and as a direct measure of the response of TIS to variable forcing. The TIS velocity time series is generated by a template-matching algorithm applied to 629 satellite image pairs obtained between February 2001 and September 2014 (Appendix B). Zonal and meridional components of wind stress are calculated from surface wind and sea-ice reanalysis data (Appendix B). We focus on local regions of upwelling, which develop where wind causes surface waters to diverge. Due to the effects of Earth's rotation, surface water is transported 90° to the left of the wind direction in the southern hemisphere, so surface water divergence is given by the mathematical curl of wind stress. We define upwelling as the vertical water velocity at the bottom of the surface layer, which we estimate from wind stress curl (Appendix B).

6.2 Results

To assess the TIS response to interannual forcing from the ocean, we limit velocity analysis to a region of the ice shelf laterally bounded by shear margins, between 20 km and 40 km from the ice front, where we expect minimal influence from pinning points, calving processes, or velocity anomalies associated with lateral motion near the ice front (Fig. 6.1). Here we see a 5 % increase in surface velocity from 2001 to 2006 followed by an immediate trend reversal, slowing 6 % by 2013 (Fig. 6.2). Minor velocity minima occurred in 2005 and 2009 and minor maxima occurred in 2010 and 2014.

With a 19 month lag, TIS velocity is negatively correlated with zonal wind throughout the domain (Fig. 6.2), indicating TIS accelerates in response to weakening of the eastward winds that drive the Antarctic Circumpolar Current or strengthening of the westward winds that drive the Antarctic Coastal Current. We assume TIS velocity is linked to a variable supply of mCDW and lag times are primarily attributable to the time required for melt rate anomalies to integrate and cause sufficient thinning to produce an observable response in surface velocity (Christianson et al., 2016). Over the deep ocean north of the continental shelf break, the negative correlation with zonal wind contrasts with the notion from classical Ekman dynamics that positive zonal wind anomalies should induce upwelling of warm deep water near 63°S. Over the continental shelf, westward winds are expected to induce southward transport of surface water, depress isotherms, and could there-

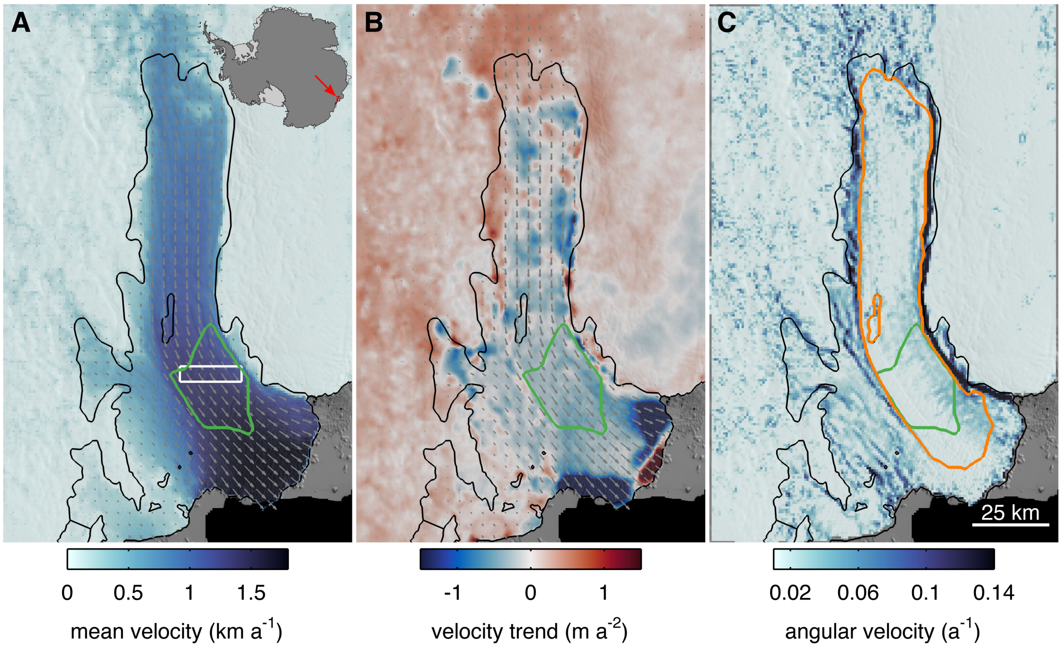

Figure 6.1: **Ice flow regime of TIS, 2001 to 2014.** **A**, Mean surface velocity from 2001 to 2014. A green polygon outlines the region of velocity measurements used in this analysis. A white box outlines the region used in a previous study by Roberts et al. (2017). Inset map shows the location of TIS. **B**, Linear trend of surface velocity indicates an overall slowdown of TIS from 2001 to 2014, while the surrounding grounded ice accelerated. Accelerations close to the ice front reflect calving processes. **C**, The curl of the mean surface velocity is used to identify shear margins within TIS. The orange polygon outlines the region of surface velocities plotted in Fig. B.2. The geographic location of TIS is shown in Fig. 6.2.

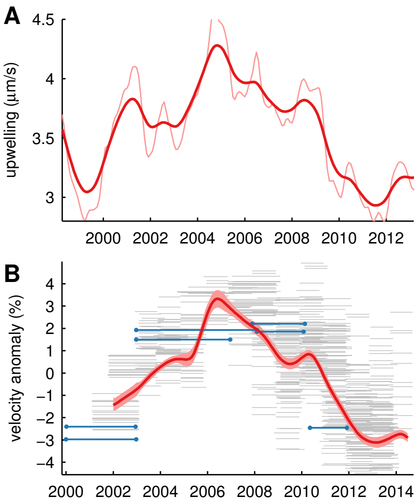

Figure 6.2: **Upwelling and ice shelf velocity time series. A**, Vertical water velocity at the bottom of the Ekman layer estimated from surface water divergence caused by wind stress; plotted is the mean velocity within the gold polygon in Fig. 6.2. Light and dark lines are lowpass filtered to 12 and 24 months, respectively. **B**, Dark red line is ice velocity derived from 629 displacement measurements shown as thin grey lines (Appendix B) bounded by shaded region of estimated uncertainties (Fig B.1). Blue lines are from displacement observations published in a previous study by Roberts et al. Roberts et al. (2017). The horizontal axis of panel (**B**) has been shifted relative to panel (**A**) to account for an observed 19 month lag.

fore prevent mCDW from surmounting the continental shelf (Ohshima et al., 1996; Hayakawa et al., 2012), yet we provide evidence that competing processes prevail.

Over the continental shelf, prevailing westward winds serve as the southern component of the wind stress curl which causes upwelling along the continental slope. Thus, the negative correlation between TIS velocity and zonal wind over the continental shelf is associated with a positive correlation between TIS velocity and upwelling along the continental slope. Over the deep ocean, zonal winds maintain their negative correlation with TIS velocity, particularly where downwelling occurs in compensation for upwelling along the continental slope. These observations suggest the meridional gradient of zonal wind stress contributes more to TIS velocity variability than do uniform zonal wind stress anomalies.

The mean coastal wind flow in the region is oriented such that its meridional component is small or nil with the exception of a northward flow diversion around Law Dome to the west of the TIS front. Throughout most of our region of study, where the meridional component of the mean velocity field is nearly zero, TIS velocity shows a weak, but slightly negative relationship with meridional wind stress (Fig. 6.2). Where coastal wind directs north around Law Dome, TIS shows a weak ($r^2 < 0.2$) positive correlation with meridional wind (Fig. B.4). TIS velocity is positively correlated with sea ice concentration throughout much of the domain, with small regions of negative correlation over the continental shelf and over the deep ocean (Fig. 6.2). However, the relationship between sea ice concentration and TIS velocity is quite weak ($r^2 < 0.15$) everywhere in the region (Fig. S4C).

Linear regression of upwelling and TIS velocity reveals that TIS acceler-

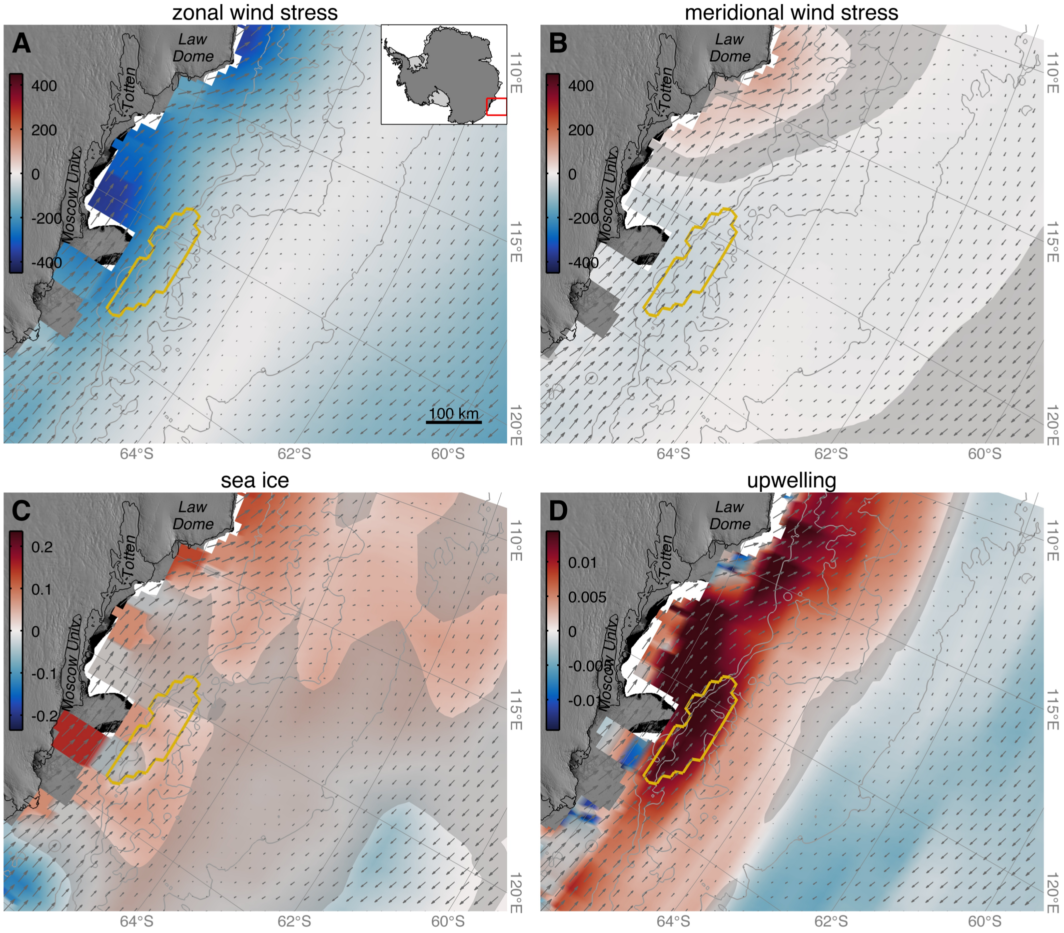

Figure 6.3: **Reanalysis fields and ice shelf velocity.** Regression coefficients of linear least squares fits of TIS velocity and **A**, zonal wind stress (μPa/(m a^{-1})); **B**, meridional wind stress (μPa/(m a^{-1})); **c**, sea ice concentration (%/(m a^{-1})); and **D**, upwelling ((μm s^{-1})/(m a^{-1})). All panels contain grey vectors representing mean wind velocity, grey 1 km bathymetric contours, and a gold polygon outlining the region of upwelling referred to in Fig. 6.2. Grey shading denotes statistical insignificance at the 95 % confidence level. Coefficients of determination are given in Fig. B.4.

ates when upwelling is strong along the continental slope (Figs. 6.2, 6.3). The relationship roughly follows bathymetric contours, indicating the role of seafloor topography in blocking mCDW intrusions when upwelling is weak. An upwelling zone shown bounded by a gold polygon in Fig. 6.2 lies upstream along the Antarctic Coastal Current and exhibits a particularly strong relationship with TIS velocity (r^2 >0.85). This implies that TIS accelerates as a response to increased melt following strong upwelling anomalies along the continental slope. Correlation is maximized with a 19 month lag (Fig. B.4), indicating the time required for upwelled mCDW to traverse the continental shelf, enter the water cavity below TIS, induce melt, and lead to ice shelf acceleration by reduced lateral shear stress.

6.3 Discussion

Oceanographic observations further implicate upwelling as the primary driver of mCDW variability on the continental shelf, where between 450 m and 650 m depth, temperature anomalies of 2°C or more can result from thermocline shoaling associated with upwelling along the nearby continental slope (Fig. B.3). The mean depth of the TIS base is 550 m in the region of our velocity time series observations, at which depth a +2°C temperature anomaly represents a sixfold increase in thermal driving potential relative to observed temperature minima of 0.4°C above the in-situ freezing point. Models indicate ice shelf melt rates scale superlinearly to quadratically with thermal driving potential (Holland et al., 2008b; Little et al., 2009; Gwyther et al., 2015), suggesting some areas of the TIS base can experience more than a tenfold increase or decrease in melt rate depending on availability of upwelled mCDW.

Profiling float and ship-based observations show a widespread presence of mCDW on the continental shelf and the thickness of the mCDW layer is linked to upwelling along the continental slope. We posit that after mCDW surmounts the continental slope, the westward winds that drive the coastal current may enhance the delivery of mCDW to the water cavity below TIS, where the ice shelf base is highly sensitive to small changes in thermal forcing (Fig. 6.3). Furthermore, a strengthened coastal current may flush cold meltwater from the cavity below TIS or intensify cavity circulation and increase melt (Gwyther et al., 2016).

Surface velocity averaged over the main trunk of TIS reached a maximum in early 2007, corresponding to a reported ice thickness minimum (Roberts et al., 2017), when the lateral shear stress restraining TIS flow was minimized (Fig. B.2 B. The linear trend of TIS slowdown amidst ongoing acceleration of the surrounding grounded ice (Fig. 6.1) is similar to a pattern seen at Pine Island Glacier, whose ice shelf has shown a response to ocean forcing by accelerating approximately 9 months after thermal anomalies arrive at the ice front (Christianson et al., 2016). The 19 month lag we observe from the time of upwelling along the continental slope to TIS acceleration includes the time required for mCDW to traverse the continental shelf. On average, TIS is much thicker than Pine Island Ice Shelf, and is thus expected to respond more slowly to basal melt anomalies (Christianson et al., 2016).

The region along the continental slope in which upwelling is highly covariant with TIS velocity is near a persistent eddy feature where dissolved silicate

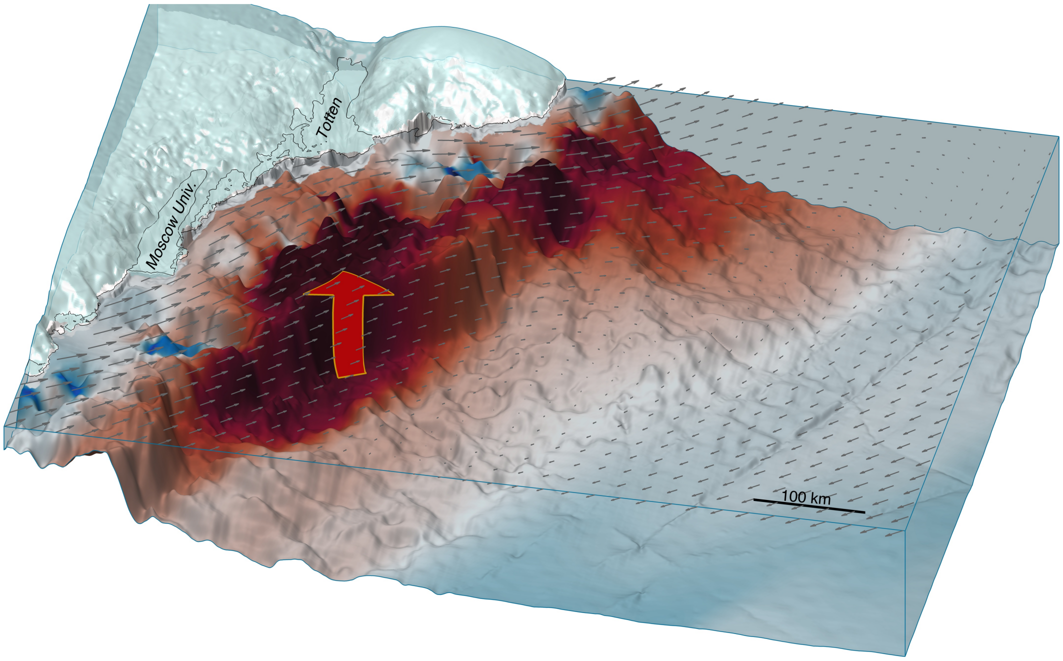

Figure 6.4: **Schematic of mCDW upwelling along the Antarctica's Sabrina Coast.** Around Antarctica, the warmest waters are found in the deep ocean north of the continental shelf break. Where wind stress (grey vectors) causes surface waters to part, warm deep water (red arrow) can upwell, surmount the continental shelf, and melt nearby ice shelves from below. Seafloor colour depicts the covariance of TIS velocity and local upwelling as in Fig. 6.2, indicating where wind-driven upwelling is closely linked to TIS velocity.

measurements have repeatedly revealed upwelling (Wakatsuchi et al., 1994); warm, saline circumpolar deep water has been detected (Bindoff et al., 2000; Williams et al., 2011); and upwelling has been shown to be positively correlated with the Southern Annular Mode (SAM) (Hayakawa et al., 2012). The SAM is the leading mode of climate variability in the southern hemisphere, it is seasonally influenced by various natural and anthropogenic drivers (Fogt et al., 2009), and its positive mode is associated with an intensification of the eastward winds around Antarctica (Thompson et al., 2011). In summer, the SAM has been trending toward its positive phase in recent decades primarily due to effects of ozone-depleting substances, but an increasing influence of atmospheric greenhouse gas is expected to dominate the SAM in the coming century and continue its positive bias as the ozone hole recovers (Fyfe et al., 2007; Sigmond et al., 2011). Projections show an intensification of the wind-driven Antarctic Circumpolar Current and an increase in upwelling particularly along the East Antarctic continental slope (Fyfe et al., 2007; Wang, 2013; Spence et al., 2014). It is possible that westward winds along the coast could weaken in conjunction with a southward migration of the divergence zone (Spence et al., 2014), in which case mCDW delivery to TIS could be tempered by a weakened coastal current; however, projections of coastal westward winds near TIS are few and their relationships to SAM or atmospheric greenhouse gas have not been validated.

We have confirmed the role of wind-driven upwelling as a primary delivery mechanism for mCDW on the continental shelf of East Antarctica and we have shown that mCDW upwelling is directly correlated with the melt-driven velocity of

TIS. Wind patterns over the Southern Ocean are expected to evolve throughout the 21 st century, and a shifting regime of upwelling could precipitate a marked response in Totten Glacier, unlocking the door to at least 3.5 m of eustatic sea level potential (Greenbaum et al., 2015) in the vast ice basin it drains.

Chapter 7

Synthesis and conclusions

7.1 Process investigations

This dissertation focused on several specific processes that affect ice shelf dynamics. Various mechanisms of basal channel formation were reviewed in Chapter 3, and a survey of studies of basal channels was included to highlight the complex nature of how basal channels affect ice shelf stability. The examination of processes at Nansen Ice Shelf added yet another layer of complexity to the story basal channels.

A surface DEM of Nansen Ice Shelf was developed in Chapter 3, and that work found that regardless of the formation mechanism, basal channels cause surface depressions in which surface water can collect. Surface rivers incise troughs in the top of the ice shelf while channelized plume flow at the base thins the ice shelf from below. The coincident thinning from above and below creates locally thin, weak areas of the ice shelf that are susceptible to hydrofracture from the surface river. We found that this sequence of events led to the major calving event at Nansen Ice Shelf which occurred in 2016.

To better understand basal channels *before* major calving events occur, in Chapter 4 I developed a new method to observe small-scale changes in ice shelf surface elevation using the nearly two-decade record of MODIS satellite images. The new technique of repeat photoclinometry revealed channelized patterns of melt and local surface elevation changes likely attributable to changes in basal shear stress at the Totten Ice Shelf grounding line.

Using the MODIS image dataset described in Chapter 4, I developed the first-ever Totten Ice Shelf velocity time series to have sub-annual resolution, described in Chapter 5. With this new dataset, I found that the terminal $\sim$50 km of the ice shelf exhibits seasonal variability in velocity. A velocity minimum occurs each year in September to October, then the ice shelf begins to accelerate in response to lost backstress at the ice front as wintertime landfast sea ice breaks up. The springtime speedup begins before surface melt appears and a ROMS model was used to show that the seasonal velocity variability is not timed with basal melt. The findings of Chapter 5 bring a more nuanced understanding of the sensitivities of Totten Ice Shelf and the host of forces acting upon it.

In Chapter 6, I expanded analysis of the Totten Ice Shelf velocity time series to investigate interannual variability. This provided the first observational evidence that Totten is sensitive to variable inflow of warm circumpolar deep water driven by wind forcing at the continental shelf break. A similar mechanism has been seen in West Antarctica, where thermal anomalies in Dotson Trough, which leads to Pine Island Bay, have been attributed to wind forcing at the continental shelf break. This similarity strengthens the case for comparisons between Totten Glacier and Pine Island Glacier—The past decade of polar research has been driven in part by ICESat-1 data that showed both ice shelves and their grounded basins thinning, apparently in

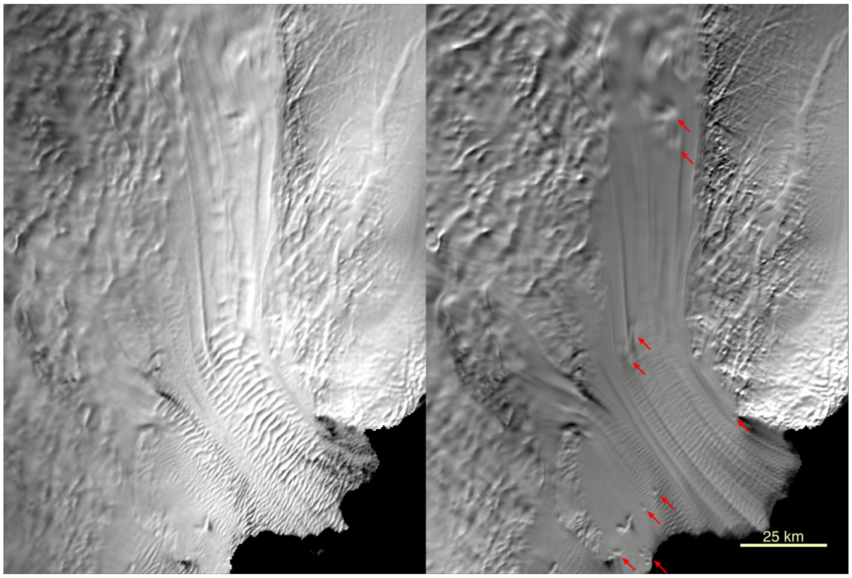

Figure 7.1: Repeat photoclinometry can be used to separate dynamic components of topography from stationary features. On the left, a single MODIS image shows a snapshot of the Totten Ice Shelf surface. On the right, the mean of 164 images spanning 14 years clarifies a series of grounding points near the ice front and ice rumples near the deep grounding line identified by Roberts et al. (2017).

response to oceanic forcing. Now we see that the variability of oceanic heat content affecting both ice shelves may be linked to wind stress at the continental shelf break.

7.2 Future work

The methods developed in this work offer much promise beyond that which has been described in this thesis. For example, I have begun employing repeat photoclinometry on Totten Ice Shelf to explore the response of channelized melt rates to subglacial lake activity that has been detected by laser altimetry near the grounding line (e.g., Young et al., 2015). In fact, subglacial lake activity itself can be detected by repeat photoclinometry.

Repeat photoclinometry also offers the ability to separate advected components of surface topography from persistent or stationary topography that may be attributable to basal processes. Akin to leaving a camera shutter open for a long-exposure photograph, the mean of many DEMs generated from images acquired over decades has a characteristic of smoothing the relief of moving topography, while bringing stationary features into crisp focus. Figure 7.2 shows how this technique can be used to identify ice shelf rumples such as those identified by Roberts et al. (2017). Taking this further, with known surface velocities and several MODIS DEMs acquired each year, it is then possible to artificially advect the moving components of surface topography from many MODIS DEMs to a common date, allowing signal-to-noise benefits of averaging without losing topographic information due to the smearing effect introduced by advection. Early results are promising, and with this technique I have been able to obtain topographic information at spatial scales smaller than the 250 m resolution of the MODIS images from which the DEMs are generated. These high-resolution DEMs can be generated for any arbitrary date within the MODIS record and may be used for such purposes as advective cross-track slope correction of repeat-track laser altimetry.

Chapter 6 showed the impact of wind-driven upwelling on the Totten Glacier system. I found that on the continental shelf, the thermocline depth is sensitive to upwelling along a large swath of the continental shelf break near Moscow University Ice Shelf. Thus, investigations of the sensitivity of Moscow University Ice Shelf are in order. As the surface altimetry record around Antarctica grows longer and improves in quality, it may be possible to compare ice shelf elevation time series to wind-driven processes around the continent. We will likely see regional variations in the magnitude of upwelling variability, and some ice shelves may respond to upwelling, while others may have topographic barriers that block intrusions of MCDW. It is unlikely that wind-driven upwelling dominates interannual variability of ice dynamics around the continent, but assessing which ice shelves respond to upwelling will be essential to fully understanding the sensitivities of the Antarctic Ice Sheet.

7.3 Bringing it all back home

This dissertation was aimed at understanding the interplay of environmental forces acting on a wide range of spatial and temporal scales. The interdisciplinary nature of this work warranted the development of a new, generalized computational toolbox that would allow simple, repeatable analysis of a variety of Antarctic geospatial datasets. Antarctic Mapping Tools for MATLAB (Greene et al., 2017b) now provides users worldwide with a well-tested, well-documented, easy-to-use toolkit and has gained widespread use across disciplines from subglacial volcanology to marine biology. The toolbox provides a wide range of general, low-level functions for mapping, plotting, georeferencing, and performing common types of basic data analysis. The toolbox was designed to let users develop and share their own plugins, and in this way, AMT can continue to grow and adapt as new datasets are introduced into the community.

Since the first version of AMT was published online, I have received feedback from users worldwide who rely on the toolkit for their daily research, have used it to rapidly generate figures to share with the public when polar science is in the news, or have begun teaching the toolbox to their undergraduate and graduate students. Students and senior researchers alike have expressed appreciation for the clear and thoughtfully written documentation that communicates not only *what* each given function was designed to do, but *why* it was created, *how* to use it, and *when* to use particular options. The synchronous nature of *how* and *why* in the documentation has helped users simultaneously develop an intuition for concepts in both Earth science, and *Matlab* programming.

Docendo discimus

"By teaching, we learn." In hindsight, it is clear that the process of writing and sharing Antarctic Mapping Tools for MATLAB contributed more to my maturation as a scientist than anything else in this dissertation. Designing useful and user-friendly functions required me to spend the past several years repeatedly asking myself, "what will users want to accomplish when they seek out this function, and what kind of data will they be working with?" In other words, "what is the Earth science question at hand, and what is the most intuitive, computationally efficient method of solving the problem?" Designing for intuition required designing with an understanding of glaciological context. When I felt I did not fully understood the glaciological context, I would seek out the relevant literature and spend hours or days exploring the available data. Designing for computational efficiency requires structuring code in a linear, logical sequence of steps. When my functions were slow or filled with unwieldy code, I found ways to simplify the computational steps, and in doing so, the underlying physics would also become clear, linear, and logical in my mind.

I found myself devoting a great deal of time to writing documentation. I would often spend two to three times as long writing the documentation for a function as it took to write the working parts of the function itself. I made an effort to write realistic examples of glaciological analysis, often using AMT to repeat the findings of well-known papers while teaching function syntax. Throughout the examples I would guide the user through the scientific decision making process, explaining each step, and in the process I was also teaching myself these very same principles. I found great value in documenting my code because it put me in the role of teaching others how and when to use my functions, and by teaching, we learn.

Appendices

Appendix A

Laser altimetry processing

Chapter 4 uses data from the Ice, Cloud, and land Elevation Satellite (ICESat) Geoscience Laser Altimeter System release 34 (Zwally et al., 2014) combined with data from the airborne International Collaborative Exploration of the Cryosphere by Airborne Profiling (ICECAP) Riegl laser altimeter (Blankenship et al., 2013). Following Fricker et al. (2009), we discard all ICESat measurements with gain values exceeding 30 and we discard measurements with quality flags `elev_use_flg`=1, `rng_uqf_is_flg`=1, or 3≥`sat_corr_flg`≤4. ICESat inter-campaign biases were removed using values obtained by Gunter et al. (2014) for East Antarctica. ICESat measurements containing tidal corrections were re-tided, then de-tided by the CATS2008B tide model Padman et al. (2002). A correction was applied to remove the inverse-barometer effect (Padman et al., 2003) using ERA-Interim surface pressure time series (ECMWF, 2009, updated 2016), bandpass filtered from 0.03 to 0.5 cycles per day to mimic the ice shelf response to weather-band frequencies (Padman et al., 2003). All floating-ice corrections were multiplied by a coefficient of flexure as a first-order measure to account for ice mechanics in the grounding zone (Vaughan, 1995). Flexure is estimated by the Antarctic Mapping Tools `iceflex_interp` function (Greene et al., 2017b). Aliasing effects from surface accumulation and firn layer processes were removed by subtracting surface elevation anomalies modelled by the firn densification model IMAU-FDM (Ligtenberg et al., 2011). This model includes temporal changes of surface mass balance, firn compaction, and meltwater processes such as percolation, retention and refreezing, and is forced at the surface by 6-hourly climate data from the regional climate model RACMO2.1 (Lenaerts et al., 2012). For the Totten region, a similar approach has been used earlier (Khazendar et al., 2013).

For the repeat-track analysis described in Section 4.3.2, observations along each repeat track were converted to a curvilinear coordinate system using satellite ground tracks as a centerline reference (Merwade et al., 2005). All measurements more than 500 m from the centerline were discarded and remaining observations were migrated to the centerline. We remove cross-track-slope-induced errors by subtracting the elevation differences between observation locations and corresponding centerline locations in a DEM taken as the mean of all photoclinometry DEMs in Figure 4.6. Centerline-migrated observations were linearly interpolated to 100 m postings along each reference track and trend estimates were obtained by linear least squares fit to the data available at each posting.

Appendix B

Methods in upwelling estimation

This Appendix describes the methods employed in upwelling estimation in Chapter 6.

B.1 Ice velocity time series

The ice velocity time series was generated from displacement fields obtained for 363 MODIS band 2 image (Scambos et al., 2001, updated 2017) pairs separated by 365±29 days (M1 data, herein) and 266 image pairs separated 730±21 days (M2 data, herein). Images were preprocessed with a Gaussian highpass filter characterised by a two-pixel standard deviation, then supersampled by a factor of two. Template matching was performed with ImGRAFT (Messerli and Grinsted, 2015) for a 500 m resolution grid using a 10x10 pixel template and 20x20 pixel search box centred on displaced locations predicted by InSAR-derived velocity fields (Rignot et al., 2011b). Displacement fields were postprocessed with a 3x3 pixel median filter and remaining grid cells with missing data were filled using a spring-metaphor inpainting technique (D'Errico, 2012).

M1 data and M2 data were treated separately to allow direct comparison of velocity fields obtained over one and two years, respectively. M2 data provides lower uncertainty for slow-moving ice whereas M1 data provides superior temporal resolution and performs best where ice moves fast, where motion is curvilinear, or where surface effects prevent matches separated by long periods of time.

An averaging technique was used to obtain velocities at monthly postings from 2001 to 2014. M1 data and M2 data were treated separately, and for each monthly posting, an average velocity was calculated for all image pairs whose first image was obtained before the posting and whose second image was obtained after the posting. At least 14 image pairs contributed to M1 data and M2 data at each monthly posting (Fig. B.1). Velocity uncertainty σ at each monthly posting t is estimated as

$$\sigma(t) = \frac{\sigma_N}{\sqrt{N}}, \tag{B.1}$$

where σ_N is the standard deviation of all N velocity measurements corresponding to time t and N is the number of image pairs contributing to each monthly posting (Taylor, 1997). The continuous ice velocity time series in this work was generated by the linear combination of lowpass filtered M2 data and highpass filtered M1 data, where the crossover filtering period is 48 months for both datasets.

B.2 Ice shelf thinning and acceleration

For a laterally-bounded ice shelf under constant driving stress, small perturbations in ice thickness δH lead to changes in ice velocity δU by

$$\delta U = U_0 \left[\left(\frac{H_0}{H_0 + \delta H} \right)^3 - 1 \right], \tag{B.2}$$

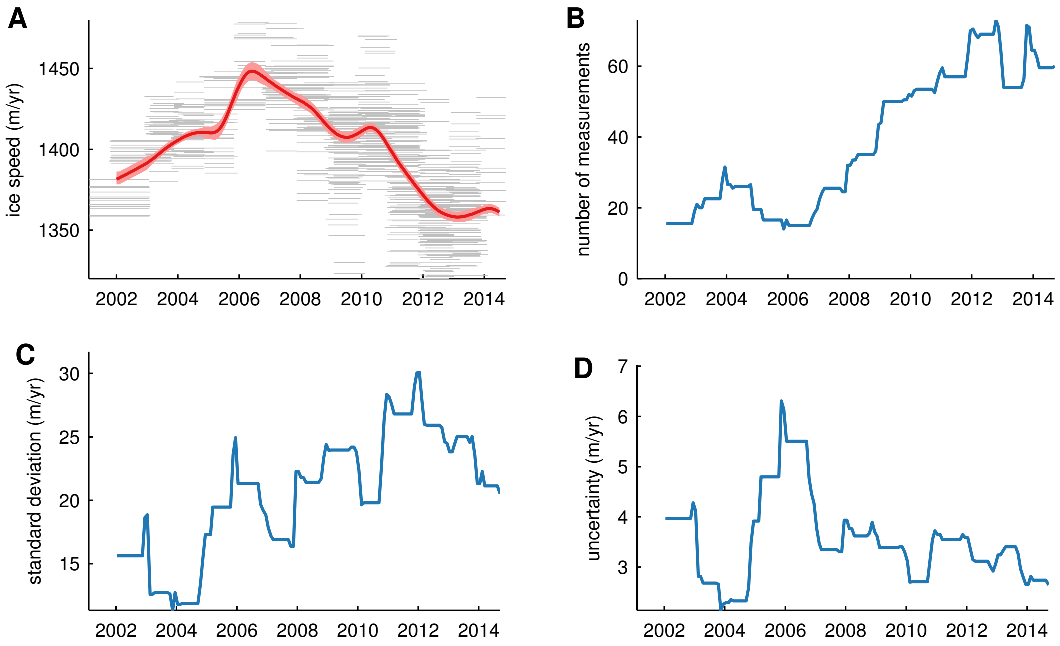

Figure B.1: **Uncertainty estimates for TIS velocity time series.** Surface velocities are obtained by feature tracking using 629 overlapping image pairs. **A**, TIS velocity measurements as in Fig. 6.2. Grey lines indicate velocity measurements from each image pair; dark red line is obtained by averaging velocity measurements at monthly postings; the shaded region bounding the velocity curve is the uncertainty estimate shown in panel (**D**). **B**, Number of displacement measurements contributing to each monthly posting. **C**, Standard deviation of velocity measurements at each monthly posting. **D** Velocity uncertainty estimate from panels (**B**) and (**C**).

where H_0 and U_0 are the nominal ice thickness and velocity, respectively (Joughin et al., 2004). Fig. B.2 compares TIS velocity observations to predictions by equation B.2, where U_0 is taken as the mean ice shelf velocity within the orange polygon in Fig. 6.1, $H_0 = 1163$ m is the mean ice thickness along the lateral shear margins of TIS (Fretwell et al., 2013), and δH is the time-varying ice thickness anomaly. We use an ice thickness time series derived from surface elevation measurements obtained by radar altimetry (Paolo et al., 2016; Roberts et al., 2017) and follow an established procedure (Pritchard et al., 2012; Khazendar et al., 2013) to remove the anomalies associated with accumulation (Lenaerts et al., 2012) and firn densification (Ligtenberg et al., 2011). Surface elevation is converted to ice thickness assuming hydrostatic equilibrium, where seawater density is 1028 kg/m^3 and column-averaged ice density is 897 kg/m^3, including a 22 m mean firn air thickness (Ligtenberg et al., 2011).

B.3 Profiling float data

Figure B.3 shows a 15 month time series of the T=-0.4°C isotherm depth obtained by a profiling float. Geolocation of the profiling float was recorded for 29 surfacing events during data collection. Profile locations (solid green line) shown in Fig. B.3 indicate surfaced positions with a GPS fix. Linearly interpolated positions when the float was under ice between 05-Apr-2015 and 27-Dec-2015 are indicated by the dashed green line. Isotherm depth was determined by linear interpolation for each profile collected by the profiling float. The isotherm depth time series was linearly interpolated to daily postings, then a first order lowpass Butterworth filter

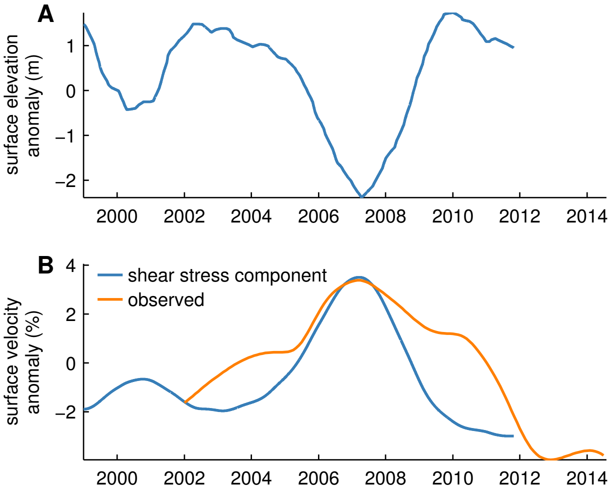

Figure B.2: **Ice shelf thinning drives acceleration.** **A**, TIS-averaged surface elevation anomaly from a previous study by Roberts et al.(Roberts et al., 2017). **B**, orange line shows surface velocity averaged over the main trunk of TIS; blue line shows ice velocity anomaly predicted from observed ice thickness anomalies. Secondary peaks in surface velocity observed in 2003 and 2010 are attributed to loss of basal stress and short-term acceleration observed in the western grounding zone of TIS. Both time series in panel (**B**) are lowpass filtered to 24 months.

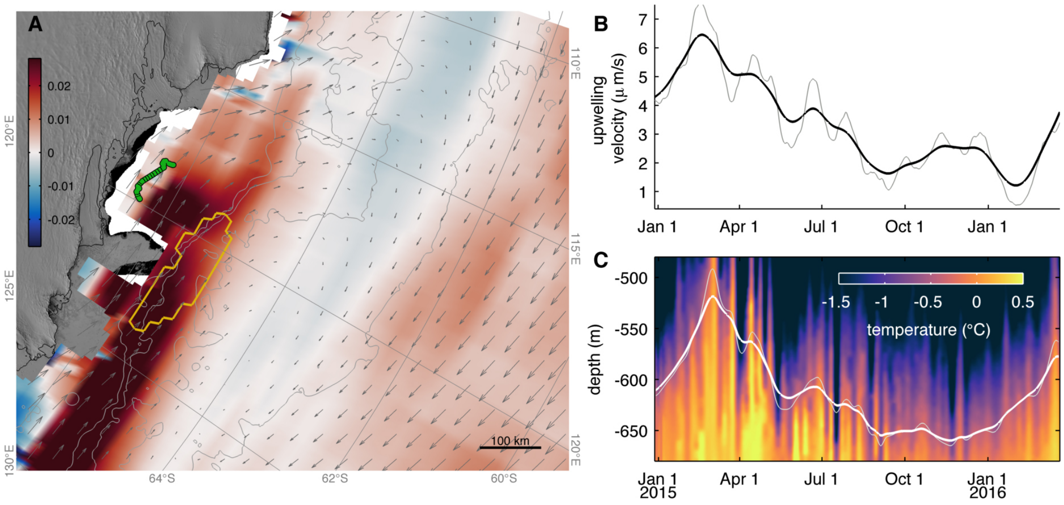

Figure B.3: **Upwelling brings warm water onto the continental slope.** **A**, Following Fig. 6.2, regression coefficients ((μm s^{-1})/m) of upwelling as a function of the T=-0.4°C isotherm depth by a profiling float, whose westward-drifting path is depicted in green. Dashed regions indicate interpolated float locations. **B**, Time series of upwelling averaged within the gold polygon in panel (**A**). **C**, Color-scaled time series of temperature logged by the profiling float overlaid with the T=-0.4°C isotherm depth in white. Heavy and light lines in panels (**B**,**C**) are lowpass filtered to 90 and 45 days, respectively.

was applied to account for the response of the lower layers to surface forcing. Filter cutoff periods of 45 and 90 days bracket expected response times(Ohshima et al., 1996), and both filtered time series agree well with upwelling time series filtered to the same periods.

B.4 Reanalysis data and upwelling estimation

This work uses ERA-Interim monthly means of daily mean (Dee et al., 2011) sea ice concentration and 10 m zonal and meridional wind components u_{10}

and v_{10} generated at 0.75° resolution and regridded to 0.125° resolution. It has been shown that higher-resolution atmospheric models often produce stronger coastal winds (Bromwich et al., 2005; Dinniman et al., 2015), but ERA-Interim matches observations well (Bracegirdle and Marshall, 2012; Jones et al., 2016) and is of sufficient resolution to capture the wind processes of interest to our analysis. Wind stress τ is calculated as

$$\tau = \rho_{\text{air}} C_{\text{D}} (u_{10}^2 + v_{10}^2), \tag{B.3}$$

where $\rho_{\text{air}} = 1.225$ kg/m^3 is the density of air and the drag coefficient is $C_{\text{D}} = 1.25 \times 10^{-3}$ in the absence of sea ice (Kara et al., 2007) and is parametrized when sea ice is present (Lüpkes and Birnbaum, 2005). Seasonal cycles are removed and time series of each grid cell are lowpass filtered with a cutoff period of 24 months using a first order Butterworth filter. Ekman pumping is calculated as the vertical velocity of water induced by surface water divergence using the relation

$$w_{\text{E}} = \text{curl}\left(\frac{\tau}{\rho_{\text{w}} f}\right), \tag{B.4}$$

where $\rho_{\text{w}} = 1028$ kg/m^3 is the density of seawater and f is the Coriolis frequency (Kessler, 2002).

B.5 Mapping and figure generation

Data analysis was performed using Antarctic Mapping Tools for MATLAB (Greene et al., 2017b) and graphics in this paper employ cmocean (Thyng et al., 2016) colormaps. Background images in Fig. 6.1,6.2 and Fig. B.3,B.4 are from the MODIS Mosaic of Antarctica (Haran et al., 2014b; Scambos et al., 2007), ground-

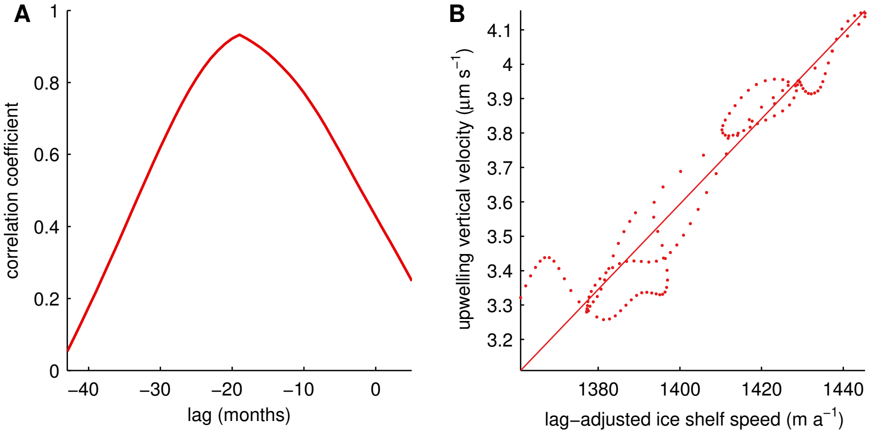

Figure B.4: **Regression of upwelling and TIS velocity.** **A**, Correlation coefficient of 24 month lowpass filtered time series of upwelling and TIS velocity, plotted as a function of lag time. Lag time corresponding to the correlation maximum (r=0.92) indicates TIS accelerates 19 months after upwelling occurs within the gold polygon shown in Fig. 6.2. **B**, Linear regression relates upwelling to TIS velocity as 0.0125 (μm s^{-1}) /(m a^{-1}).

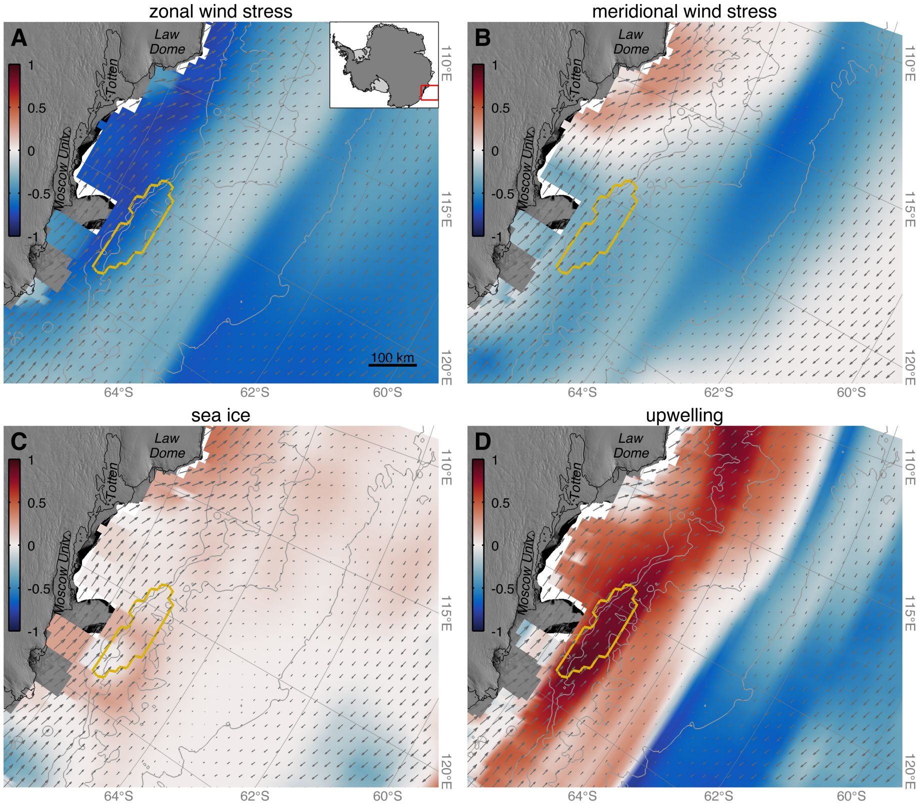

Figure B.5: **Coefficients of determination.** Values of $r \cdot |r|$ indicate the strength and sign of the relationship between TIS velocity and reanalysis fields for respective linear regressions in Fig. 6.2.

ing lines are from MEaSUREs radar mapping (Mouginot et al., 2016), and bathymetric contours are from IBCSO (Arndt et al., 2013).

Bibliography

G. A, J. Wahr, and S. Zhong. Computations of the viscoelastic response of a 3-D compressible Earth to surface loading: an application to Glacial Isostatic Adjustment in Antarctica and Canada. *Geophysical Journal International*, 192(2): 557–572, 2013.

K. E. Alley, T. A. Scambos, M. R. Siegfried, and H. A. Fricker. Impacts of warm water on Antarctic ice shelf stability through basal channel formation. *Nature Geoscience*, 9(4):290–293, 2016. doi: doi:10.1038/ngeo2675.

R. B. Alley, P. U. Clark, P. Huybrechts, and I. Joughin. Ice-sheet and sea-level changes. *science*, 310(5747):456–460, 2005. doi: 10.1126/science.1114613.

T. Aoki, T. Aoki, M. Fukabori, and A. Uchiyama. Numerical simulation of the atmospheric effects on snow albedo with a multiple scattering radiative transfer model for the atmosphere-snow system. *Journal of the Meteorological Society of Japan*, 77(2):595–614, 1999.

J. M. Arblaster and G. A. Meehl. Contributions of external forcings to southern annular mode trends. *Journal of Climate*, 19(12):2896–2905, 2006. doi: 10.1175/jcli3774.1. URL `https://doi.org/10.1175/jcli3774.1`.

J. E. Arndt, H. W. Schenke, M. Jakobsson, F. O. Nitsche, G. Buys, B. Goleby, M. Rebesco, F. Bohoyo, J. Hong, J. Black, et al. The International Bathymetric Chart of the Southern Ocean (IBCSO) Version 1.0—A new bathymetric compilation covering circum-Antarctic waters. *Geophysical Research Letters*, 40(12): 3111–3117, 2013. doi: 10.1002/grl.50413.

K. R. Arrigo and G. L. Van Dijken. Phytoplankton dynamics within 37 antarctic coastal polynya systems. *Journal of Geophysical Research: Oceans*, 108(C8), 2003. doi: 10.1029/2002JC001739.

M. Årthun, K. W. Nicholls, K. Makinson, M. A. Fedak, and L. Boehme. Seasonal inflow of warm water onto the southern Weddell Sea continental shelf, Antarctica. *Geophysical Research Letters*, 39(17), 2012.

K. Assmann, A. Jenkins, D. Shoosmith, D. Walker, S. Jacobs, and K. Nicholls. Variability of Circumpolar Deep Water transport onto the Amundsen Sea Continental shelf through a shelf break trough. *Journal of Geophysical Research: Oceans*, 118(12):6603–6620, 2013.

J. Bamber, J. Gomez-Dans, and J. Griggs. A new 1 km digital elevation model of the Antarctic derived from combined satellite radar and laser data–Part 1: Data and methods. *The Cryosphere*, 3(1):101–111, 2009. doi: 10.5194/tc-3-101-2009.

J. L. Bamber and W. Aspinall. An expert judgement assessment of future sea level rise from the ice sheets. *Nature Climate Change*, 2013.

A. F. Banwell, D. R. MacAyeal, and O. V. Sergienko. Breakup of the Larsen B Ice Shelf triggered by chain reaction drainage of supraglacial lakes. *Geophysical Research Letters*, 40(22):5872–5876, 2013.

D. Barber and R. Massom. The role of sea ice in Arctic and Antarctic polynyas. *Elsevier Oceanography Series*, 74:1–54, 2007.

I. Bartholomew, P. Nienow, D. Mair, A. Hubbard, M. A. King, and A. Sole. Seasonal evolution of subglacial drainage and acceleration in a Greenland outlet glacier. *Nature Geoscience*, 3(6):408, 2010.

R. E. Bell, M. Studinger, C. A. Shuman, M. A. Fahnestock, and I. Joughin. Large subglacial lakes in East Antarctica at the onset of fast-flowing ice streams. *Nature*, 445(7130):904, 2007. doi: 10.1038/nature05554.

R. E. Bell, W. Chu, J. Kingslake, I. Das, M. Tedesco, K. J. Tinto, C. J. Zappa, M. Frezzotti, A. Boghosian, and W. S. Lee. Antarctic ice shelf potentially stabilized by export of meltwater in surface river. *Nature*, 544(7650):344–348, 2017.

N. L. Bindoff, M. A. Rosenberg, and M. J. Warner. On the circulation and water masses over the Antarctic continental slope and rise between 80 and 150 E. *Deep Sea Research Part II: Topical Studies in Oceanography*, 47(12):2299–2326, 2000. doi: 10.1016/S0967-0645(00)00038-2. URL `http://doi.org/10.1016/S0967-0645(00)00038-2`.

R. Bindschadler and P. Vornberger. Detailed elevation map of Ice Stream C, Antarctica, using satellite imagery and airborne radar. *Annals of Glaciology*, 20(1): 327–335, 1994.

R. Bindschadler, T. A. Scambos, H. Rott, P. Skvarca, and P. Vornberger. Ice dolines on Larsen Ice Shelf, Antarctica. *Annals of Glaciology*, 34(1):283–290, 2002. doi: 10.3189/172756402781817996.

R. Bindschadler, P. Vornberger, A. Fleming, A. Fox, J. Mullins, D. Binnie, S. J. Paulsen, B. Granneman, and D. Gorodetzky. The Landsat image mosaic of Antarctica. *Remote Sensing of Environment*, 112(12):4214–4226, 2008.

R. Bindschadler, H. Choi, A. Wichlacz, R. Bingham, J. Bohlander, K. Brunt, H. Corr, R. Drews, H. Fricker, M. Hall, et al. Getting around Antarctica: new high-resolution mappings of the grounded and freely-floating boundaries of the Antarctic ice sheet created for the International Polar Year. *The Cryosphere*, 2011a.

R. Bindschadler, D. G. Vaughan, and P. Vornberger. Variability of basal melt beneath the Pine Island Glacier ice shelf, West Antarctica. *Journal of Glaciology*, 57(204):581–595, 2011b. doi: 10.3189/002214311797409802.

R. A. Bindschadler, T. A. Scambos, H. Choi, and T. M. Haran. Ice sheet change detection by satellite image differencing. *Remote Sensing of Environment*, 114 (7):1353–1362, 2010. doi: 10.1016/j.rse.2010.01.014.

D. Blankenship, S. Kempf, D. Young, T. Richter, D. Schroeder, J. Greenbaum, J. Holt, T. van Ommen, R. Warner, J. Roberts, N. Young, E. Lemeur, and M. Siegert. IceBridge HiCARS 1 L2 Geolocated Ice Thickness, Version 1., 2011.

D. Blankenship, S. Kempf, D. Young, J. Roberts, T. van Ommen, R. Forsberg, M. Siegert, S. Palmer, and J. Dowdeswell. IceBridge Riegl Laser Altimeter L2 Geolocated Surface Elevation Triplets, Version 1, ILUTP2, 2013.

T. J. Bracegirdle and G. J. Marshall. The reliability of Antarctic tropospheric pressure and temperature in the latest global reanalyses. *Journal of Climate*, 25(20): 7138–7146, 2012.

C. A. Brewer. ColorBrewer 2.0, 2015. URL `http://www.ColorBrewer2.org`.

D. H. Bromwich, A. J. Monaghan, K. W. Manning, and J. G. Powers. Real-time forecasting for the Antarctic: an evaluation of the Antarctic Mesoscale Prediction System (AMPS). *Monthly Weather Review*, 133(3):579–603, 2005.

K. M. Brunt, H. A. Fricker, L. Padman, and S. O'Neel. ICESat-Derived Grounding Zone for Antarctic Ice Shelves, 2010. URL `http://dx.doi.org/10.7265/N5CF9N19`.

K. M. Brunt, H. A. Fricker, and L. Padman. Analysis of ice plains of the Filchner-Ronne Ice Shelf, Antarctica, using ICESat laser altimetry. *Journal of Glaciology*, 57(205):965–975, 2011. doi: 10.3189/002214311798043753. URL `http://dx.doi.org/10.3189/002214311798043753`.

G. Casassa and I. M. Whillans. Decay of surface topography on the Ross Ice Shelf, Antarctica. *Annals of Glaciology*, 20(1):249–253, 1994. doi: 10.3198/1994AoG20-1-249-253.

M. Catalán, L. M. Agudo, and A. Muñoz. Geomagnetic secular variation of Bransfield Strait (Western Antarctica) from analysis of marine crossover data. *Geophysical Journal International*, 165(1):73–86, 2006.

D. Cavalieri, C. Parkinson, P. Gloersen, and H. J. Zwally. Sea Ice Concentrations from Nimbus-7 SMMR and DMSP SSM/I-SSMIS Passive Microwave Data, Version 1, 1996. URL `http://dx.doi.org/10.5067/8GQ8LZQVL0VL`.

N. S. . I. D. Center. IceBridge Data – Standard Projections for Gridded Data, 2015. URL `http://nsidc.org/data/icebridge/projections_grids.html`.

J. Chen, C. Wilson, D. Blankenship, and B. Tapley. Accelerated Antarctic ice loss from satellite gravity measurements. *Nature Geoscience*, 2(12):859, 2009.

K. Christianson, M. Bushuk, P. Dutrieux, B. R. Parizek, I. R. Joughin, R. B. Alley, D. E. Shean, E. P. Abrahamsen, S. Anandakrishnan, K. J. Heywood, et al. Sensitivity of Pine Island Glacier to observed ocean forcing. *Geophysical Research Letters*, 2016. doi: 10.1002/2016GL070500.

S. Cobeldick. ColorBrewer: Attractive and Distinctive Colormaps, 2015. URL `http://www.mathworks.com/matlabcentral/fileexchange/45208`.

A. P. R. Cooper. A simple shape-from-shading algorithm applied to images of ice-covered terrain. *IEEE Transactions on Geoscience and Remote Sensing*, 32(6): 1196–1198, 1994.

M. Craven, I. Allison, H. A. Fricker, and R. Warner. Properties of a marine ice layer under the Amery Ice Shelf, East Antarctica. *Journal of Glaciology*, 55 (192):717–728, 2009. doi: 10.3189/002214309789470941.

M. Dallaston, I. Hewitt, and A. Wells. Channelization of plumes beneath ice shelves. *Journal of Fluid Mechanics*, 785:109–134, 2015. doi: 10.1017/jfm.2015.609.

C. H. Davis and A. C. Ferguson. Elevation change of the Antarctic ice sheet, 1995-2000, from ERS-2 satellite radar altimetry. *Geoscience and Remote Sensing, IEEE Transactions on*, 42(11):2437–2445, 2004.

G. E. R. Deacon. *The Hydrology of the Southern Ocean*. Cambridge University Press, 1937.

R. Death, J. Wadham, F. Monteiro, A. Le Brocq, M. Tranter, A. Ridgwell, S. Dutkiewicz, and R. Raiswell. Antarctic ice sheet fertilises the southern ocean. *Biogeosciences*, 11(10):2635–2643, 2014. doi: 10.5194/bg-11-2635-2014.

D. P. Dee, S. M. Uppala, A. J. Simmons, P. Berrisford, P. Poli, S. Kobayashi, U. Andrae, M. A. Balmaseda, G. Balsamo, P. Bauer, P. Bechtold, A. C. M. Beljaars, L. van de Berg, J. Bidlot, N. Bormann, C. Delsol, R. Dragani, M. Fuentes, A. J. Geer, L. Haimberger, S. B. Healy, H. Hersbach, E. V. Hlm, L. Isaksen, P. Kllberg, M. Khler, M. Matricardi, A. P. McNally, B. M. Monge-Sanz, J.-J. Morcrette, B.-K. Park, C. Peubey, P. de Rosnay, C. Tavolato, J.-N. Thpaut, and F. Vitart. The ERA-Interim reanalysis: configuration and performance of the data assimilation system. *Quarterly Journal of the Royal Meteorological Society*, 137(656):553–597, 2011. ISSN 1477-870X. doi: 10.1002/qj.828. URL `http://dx.doi.org/10.1002/qj.828`.

M. Depoorter, J. Bamber, J. Griggs, J. Lenaerts, S. Ligtenberg, M. van den Broeke, and G. Moholdt. Calving fluxes and basal melt rates of antarctic ice shelves. *Nature*, 502(7469):89–92, 2013. doi: 10.1038/nature12567.

J. D'Errico. Inpaint nans, 2012. MATLAB Central File Exchange, http://www.mathworks.com/matlabcentral/fileexchange/4551.

T. M. Diehl, J. W. Holt, D. D. Blankenship, D. A. Young, T. A. Jordan, and F. Ferraccioli. First airborne gravity results over the Thwaites Glacier catchment, West Antarctica. *Geochemistry, Geophysics, Geosystems*, 9(4), 2008.

M. S. Dinniman, J. M. Klinck, and W. O. Smith. Cross-shelf exchange in a model of the Ross Sea circulation and biogeochemistry. *Deep Sea Research Part II: Topical Studies in Oceanography*, 50(22):3103–3120, 2003.

M. S. Dinniman, J. M. Klinck, L.-S. Bai, D. H. Bromwich, K. M. Hines, and D. M. Holland. The effect of atmospheric forcing resolution on delivery of ocean heat to the Antarctic floating ice shelves. *Journal of Climate*, 28(15):6067–6085, 2015.

C. Doake and D. Vaughan. Rapid disintegration of the Wordie Ice Shelf in response to atmospheric warming. *Nature*, 350(6316):328–330, 1991.

C. Dow, W. Lee, J. Greenbaum, C. Greene, D. Blankenship, K. Poiner, A. Forrest, D. Young, and C. Zappa. Basal channels drive active surface hydrology and transverse ice-shelf fracture. in review.

J. A. Dowdeswell and N. F. McIntyre. The surface topography of large ice masses from Landsat imagery. *Journal of Glaciology*, 33(113):16–23, 1987. doi: 10.3198/1987JoG33-113-16-23.

J. Dozier, S. R. Schneider, and D. F. McGinnis. Effect of grain size and snowpack water equivalence on visible and near-infrared satellite observations of snow. *Water Resources Research*, 17(4):1213–1221, 1981. doi: 10.1029/WR017i004p01213.

R. Drews. Evolution of ice-shelf channels in Antarctic ice shelves. *The Cryosphere*, 9(3):1169–1181, 2015. doi: 10.5194/tc-9-1169-2015.

R. Drews, F. Pattyn, I. Hewitt, F. Ng, S. Berger, K. Matsuoka, V. Helm, N. Bergeot, L. Favier, and N. Neckel. Actively evolving subglacial conduits and eskers initiate ice shelf channels at an Antarctic grounding line. *Nature Communications*, 8 (15228), 2017.

T. Dupont and R. Alley. Assessment of the importance of ice-shelf buttressing to ice-sheet flow. *Geophysical Research Letters*, 32(4), 2005. doi: 10.1029/2004GL022024.

T. Dupont and R. Alley. Role of small ice shelves in sea-level rise. *Geophysical Research Letters*, 33(9):L09503, 2006.

P. Dutrieux, D. G. Vaughan, H. F. Corr, A. Jenkins, P. R. Holland, I. Joughin, and A. Fleming. Pine Island Glacier ice shelf melt distributed at kilometre scales. *The Cryosphere*, 7:1543–1555, 2013. doi: 10.5194/tc-7-1543-2013.

P. Dutrieux, J. De Rydt, A. Jenkins, P. R. Holland, H. K. Ha, S. H. Lee, E. J. Steig, Q. Ding, E. P. Abrahamsen, and M. Schröder. Strong sensitivity of Pine Island ice-shelf melting to climatic variability. *Science*, 343(6167):174–178, 2014. doi: 10.1126/science.1244341. URL `http://dx.doi.org/10.1126/science.1244341`.

ECMWF. European Centre for Medium-Range Weather Forecasts ERA-Interim Project, 2009, updated 2016. Research Data Archive at the National Center for Atmospheric Research, Computational and Information Systems Laboratory.

V. Ekman. On the influence of the earth's rotation on ocean currents. *Ark. Mat. Astron. Fys.*, 2:1–53, 1905.

J. P. Ericson, C. J. Vörösmarty, S. L. Dingman, L. G. Ward, and M. Meybeck. Effective sea-level rise and deltas: causes of change and human dimension implications. *Global and Planetary Change*, 50(1):63–82, 2006.

M. Fahnestock, T. Scambos, R. Bindschadler, and G. Kvaran. A millennium of variable ice flow recorded by the Ross Ice Shelf, Antarctica. *Journal of Glaciology*, 46(155):652–664, 2000. doi: 10.3189/172756500781832693.

M. Fahnestock, T. Scambos, T. Moon, A. Gardner, T. Haran, and M. Klinger. Rapid large-area mapping of ice flow using Landsat 8. *Remote Sensing of Environment*, 185:84–94, 2016.

D. Felikson, T. C. Bartholomaus, G. A. Catania, N. J. Korsgaard, K. H. Kjær, M. Morlighem, B. Noël, M. van den Broeke, L. A. Stearns, E. L. Shroyer, et al. Inland thinning on the greenland ice sheet controlled by outlet glacier geometry. *Nature Geoscience*, 10(5):366–369, 2017.

T. Flament, E. Berthier, and F. Rémy. Cascading water underneath wilkes land, east antarctic ice sheet, observed using altimetry and digital elevation models. *Cryosphere*, 8(2):673–687, 2014. doi: 10.5194/tc-8-673-2014.

R. L. Fogt, J. Perlwitz, A. J. Monaghan, D. H. Bromwich, J. M. Jones, and G. J. Marshall. Historical SAM variability. Part II: Twentieth-century variability and trends from reconstructions, observations, and the IPCC AR4 models. *Journal of Climate*, 22(20):5346–5365, 2009.

C. Förste, R. Schmidt, R. Stubenvoll, F. Flechtner, U. Meyer, R. König, H. Neumayer, R. Biancale, J.-M. Lemoine, S. Bruinsma, et al. The GeoForschungsZentrum Potsdam/Groupe de Recherche de Geodesie Spatiale satellite-only and combined gravity field models: EIGEN-GL04S1 and EIGEN-GL04C. *Journal of Geodesy*, 82(6):331–346, 2008.

P. Fretwell, H. D. Pritchard, D. G. Vaughan, J. Bamber, N. Barrand, R. Bell, C. Bianchi, R. Bingham, D. Blankenship, G. Casassa, et al. Bedmap2: improved ice bed, surface and thickness datasets for Antarctica. *The Cryosphere*, 7(1), 2013. doi: 10.5194/tc-7-375-2013.

M. Frezzotti and M. Mabin. 20th century behaviour of Drygalski Ice Tongue, Ross Sea, Antarctica. *Annals of Glaciology*, 20(1):397–400, 1994.

H. A. Fricker and T. Scambos. Connected subglacial lake activity on lower Mercer and Whillans ice streams, West Antarctica, 2003–2008. *Journal of Glaciology*, 55(190):303–315, 2009. doi: 10.3189/002214309788608813.

H. A. Fricker, S. Popov, I. Allison, and N. Young. Distribution of marine ice beneath the Amery Ice Shelf. *Geophysical Research Letters*, 28(11):2241–2244, 2001. doi: 10.1029/2000GL012461.

H. A. Fricker, T. Scambos, R. Bindschadler, and L. Padman. An active subglacial water system in West Antarctica mapped from space. *Science*, 315(5818):1544–1548, 2007. doi: 10.1126/science.1136897.

H. A. Fricker, R. Coleman, L. Padman, T. A. Scambos, J. Bohlander, and K. M. Brunt. Mapping the grounding zone of the Amery Ice Shelf, East Antarctica using InSAR, MODIS and ICESat. *Antarctic Science*, 21(05):515–532, 2009. doi: 10.1017/S095410200999023X.

J. J. Fürst, G. Durand, F. Gillet-Chaulet, L. Tavard, M. Rankl, M. Braun, and O. Gagliardini. The safety band of Antarctic ice shelves. *Nature Climate Change*, 6(5):479–482, 2016. doi: 10.1038/nclimate2912.

J. C. Fyfe, O. A. Saenko, K. Zickfeld, M. Eby, and A. J. Weaver. The role of poleward-intensifying winds on Southern Ocean warming. *Journal of Climate*, 20(21):5391–5400, 2007. doi: 10.1175/2007JCLI1764.1. URL `http://dx.doi.org/10.1175/2007JCLI1764.1`.

B. Galton-Fenzi, J. Hunter, R. Coleman, S. Marsland, and R. Warner. Modeling the basal melting and marine ice accretion of the Amery Ice Shelf. *Journal of Geophysical Research: Oceans*, 117(C9), 2012.

C. V. Gladish, D. M. Holland, P. R. Holland, and S. F. Price. Ice-shelf basal channels in a coupled ice/ocean model. *Journal of Glaciology*, 58(212):1227–1244, 2012. doi: 10.3189/2012JoG12J003.

N. Glasser, S. Jennings, M. Hambrey, and B. Hubbard. Origin and dynamic significance of longitudinal structures (” flow stripes”) in the Antarctic Ice Sheet. *Earth Surface Dynamics*, 3(2):239, 2015. doi: 10.5194/esurf-3-239-2015.

L. S. Glaze, L. Wilson, and P. J. Mouginis-Mark. Volcanic eruption plume top topography and heights as determined from photoclinometric analysis of satellite data. *Journal of Geophysical Research: Solid Earth*, 104(B2):2989–3001, 1999. doi: 10.1029/1998JB900047.

D. Goldberg, D. Holland, and C. Schoof. Grounding line movement and ice shelf buttressing in marine ice sheets. *Journal of Geophysical Research: Earth Surface*, 114(F4), 2009. doi: 10.1029/2008JF001227.

N. Gourmelen, D. N. Goldberg, K. Snow, S. F. Henley, R. G. Bingham, S. Kimura, A. E. Hogg, A. Shepherd, J. Mouginot, J. Lenaerts, et al. Channelized melting drives thinning under a rapidly melting Antarctic ice shelf. *Geophysical Research Letters*, 2017. doi: 10.1002/2017GL074929. URL `http://dx.doi.org/10.1002/2017GL074929`.

A. G. C. Graham, P. Dutrieux, D. G. Vaughan, F. O. Nitsche, R. Gyllencreutz, S. L. Greenwood, R. D. Larter, and A. Jenkins. Seabed corrugations beneath an Antarctic ice shelf revealed by autonomous underwater vehicle survey: Origin and implications for the history of Pine Island Glacier. *Journal of Geophysical Research: Earth Surface*, 118(3):1356–1366, 2013. ISSN 2169-9011. doi: 10.1002/jgrf.20087.

L. Gray, I. Joughin, S. Tulaczyk, V. B. Spikes, R. Bindschadler, and K. Jezek. Evidence for subglacial water transport in the West Antarctic Ice Sheet through three-dimensional satellite radar interferometry. *Geophysical Research Letters*, 32(3), 2005. doi: 10.1029/2004GL021387.

J. Greenbaum, D. Blankenship, D. Young, T. Richter, J. Roberts, A. Aitken, B. Legresy, D. Schroeder, R. Warner, T. Van Ommen, et al. Ocean access to a cavity beneath Totten Glacier in East Antarctica. *Nature Geoscience*, 8(4): 294–298, 2015. doi: 10.1038/ngeo2388.

C. A. Greene. Low-frequency acoustic classification of methane hydrates. Master's thesis, The University of Texas at Austin, 2010.

C. A. Greene and D. D. Blankenship. A method of repeat photoclinometry for detecting kilometer-scale ice sheet surface evolution. *IEEE Transactions on Geoscience and Remote Sensing*, in press. doi: 10.1109/TGRS.2017.2773364.

C. A. Greene and P. S. Wilson. Laboratory investigation of a passive acoustic method for measurement of underwater gas seep ebullition. *The Journal of the Acoustical Society of America*, 131(1):EL61–EL66, 2012.

C. A. Greene, D. D. Blankenship, D. E. Gwyther, A. Silvano, and E. van Wijk. Wind causes Totten Ice Shelf melt and acceleration. *Science Advances*, 3:e1701681, 2017a. doi: 10.1126/sciadv.1701681.

C. A. Greene, D. E. Gwyther, and D. D. Blankenship. Antarctic Mapping Tools for MATLAB. *Computers & Geosciences*, 104:151–157, 2017b. doi: 10.1016/j.cageo.2016.08.003. URL `http://www.sciencedirect.com/science/article/pii/S0098300416302163`.

E. Gudlaugsson, A. Humbert, T. Kleiner, J. Kohler, and K. Andreassen. The influence of a model subglacial lake on ice dynamics and internal layering. *The Cryosphere*, 10(2):751–760, 2016. doi: 10.5194/tc-10-751-2016.

G. H. Gudmundsson. Transmission of basal variability to a glacier surface. *Journal of Geophysical Research: Solid Earth*, 108(B5), 2003. doi: 10.1029/2002JB002107.

G. H. Gudmundsson, C. F. Raymond, and R. Bindschadler. The origin and longevity of flow stripes on Antarctic ice streams. *Annals of Glaciology*, 27(1):145–152, 1998. doi: 10.3198/1998AoG27-1-145-152.

B. Gunter, O. Didova, R. Riva, S. Ligtenberg, J. Lenaerts, M. King, M. Van den Broeke, and T. Urban. Empirical estimation of present-day Antarctic glacial isostatic adjustment and ice mass change. *The Cryosphere*, 8(2):743–760, 2014.

D. Gwyther, B. Galton-Fenzi, J. Hunter, and J. Roberts. Simulated melt rates for the Totten and Dalton ice shelves. *Ocean Science*, 10(3):267–279, 2014. doi: 10.5194/os-10-267-2014. URL `http://dx.doi.org/10.1016/10.5194/os-10-267-2014`.

D. E. Gwyther, B. K. Galton-Fenzi, M. S. Dinniman, J. L. Roberts, and J. R. Hunter. The effect of basal friction on melting and freezing in ice shelf–ocean models. *Ocean Modelling*, 95:38–52, 2015. doi: 10.1016/j.ocemod.2015.09.004. URL `http://dx.doi.org/10.1016/j.ocemod.2015.09.004`.

D. E. Gwyther, E. A. Cougnon, B. K. Galton-Fenzi, J. L. Roberts, J. R. Hunter, and M. S. Dinniman. Modelling the response of ice shelf basal melting to different ocean cavity environmental regimes. *Annals of Glaciology*, 57(73):131–141, 2016. doi: 10.1017/aog.2016.31.

A. Hall and M. Visbeck. Synchronous variability in the southern hemisphere atmosphere, sea ice, and ocean resulting from the annular mode. *Journal of Climate*, 15(21):3043–3057, 2002.

T. Haran, J. Bohlander, T. Scambos, T. Painter, and M. Fahnestock. MODIS Mosaic of Antarctica 2008-2009 (MOA2009) Image Map, Version 1, Optical Snow Grain Size, 2014a.

T. Haran, J. Bohlander, T. Scambos, T. Painter, and M. Fahnestock. MODIS Mosaic of Antarctica 2008-2009 (MOA2009) Image Map, Version 1. *NSIDC National Snow and Ice Data Center*, 2014b. doi: 10.7265/N5KP8037.

T. Hattermann, O. A. Nøst, J. M. Lilly, and L. H. Smedsrud. Two years of oceanic observations below the Fimbul Ice Shelf, Antarctica. *Geophysical Research Letters*, 39(12), 2012.

H. Hayakawa, K. Shibuya, Y. Aoyama, Y. Nogi, and K. Doi. Ocean bottom pressure variability in the Antarctic Divergence Zone off Lützow-Holm Bay, East Antarctica. *Deep Sea Research Part I: Oceanographic Research Papers*, 60:22–31, 2012. doi: 10.1016/j.dsr.2011.09.005. URL `http://dx.doi.org/10.1016/j.dsr.2011.09.005`.

P. Heil, R. A. Massom, I. Allison, A. P. Worby, and V. I. Lytle. Role of off-shelf to on-shelf transitions for East Antarctic sea ice dynamics during spring 2003. *Journal of Geophysical Research: Oceans (1978–2012)*, 114(C9), 2009.

H. H. Hellmer, F. Kauker, R. Timmermann, J. Determann, and J. Rae. Twenty-first-century warming of a large Antarctic ice-shelf cavity by a redirected coastal current. *Nature*, 485(7397):225–228, 2012.

V. Helm, A. Humbert, and H. Miller. Elevation and elevation change of Greenland and Antarctica derived from CryoSat-2. *The Cryosphere*, 8(4):1539–1559, 2014. doi: 10.5194/tc-8-1539-2014.

L. Herraiz-Borreguero, D. Lannuzel, P. Van Der Merwe, A. Treverrow, and J. Pedro. Large flux of iron from the Amery Ice Shelf marine ice to Prydz Bay, East Antarctica. *Journal of Geophysical Research: Oceans*, 121(8):6009–6020, 2016. doi: 10.1002/2016JC011687.

J. Hinkel, D. Lincke, A. T. Vafeidis, M. Perrette, R. J. Nicholls, R. S. Tol, B. Marzeion, X. Fettweis, C. Ionescu, and A. Levermann. Coastal flood damage and adaptation costs under 21st century sea-level rise. *Proceedings of the National Academy of Sciences*, 111(9):3292–3297, 2014.

D. M. Holland, R. H. Thomas, B. De Young, M. H. Ribergaard, and B. Lyberth. Acceleration of Jakobshavn Isbrætriggered by warm subsurface ocean waters. *Nature geoscience*, 1(10):659–664, 2008a. doi: 10.1038/ngeo316.

P. R. Holland and D. L. Feltham. The effects of rotation and ice shelf topography on frazil-laden ice shelf water plumes. *Journal of physical oceanography*, 36(12): 2312–2327, 2006. doi: 10.1175/JPO2970.1.

P. R. Holland, A. Jenkins, and D. M. Holland. The response of ice shelf basal melting to variations in ocean temperature. *Journal of Climate*, 21(11):2558–2572, 2008b. doi: 10.1175/2007JCLI1909.1.

P. R. Holland, H. F. Corr, D. G. Vaughan, A. Jenkins, and P. Skvarca. Marine ice in Larsen Ice Shelf. *Geophysical Research Letters*, 36(11), 2009. doi: 10.1029/2009GL038162.

J. W. Holt, T. G. Richter, S. D. Kempf, D. L. Morse, and D. D. Blankenship. Airborne gravity over Lake Vostok and adjacent highlands of East Antarctica. *Geochemistry, Geophysics, Geosystems*, 7(11), 2006.

A. D. Howard, K. R. Blasius, and J. A. Cutts. Photoclinometric determination of the topography of the Martian north polar cap. *Icarus*, 50(2):245–258, 1982. doi: 10.1016/0019-1035(82)90125-7.

I. Howat, C. Porter, M. Noh, B. Smith, and S. Jeong. Sudden drainage of a subglacial lake beneath the Greenland Ice Sheet. *The Cryosphere*, 9(1):103–108, 2015. doi: 10.5194/tc-9-103-2015.

I. M. Howat, J. E. Box, Y. Ahn, A. Herrington, and E. M. McFadden. Seasonal variability in the dynamics of marine-terminating outlet glaciers in Greenland. *Journal of Glaciology*, 56(198):601–613, 2010.

T. Hughes. On the disintegration of ice shelves: the role of fracture. *Journal of Glaciology*, 29(101):98–117, 1983.

C. L. Hulbe, R. Johnston, I. Joughin, and T. Scambos. Marine ice modification of fringing ice shelf flow. *Arctic, Antarctic, and Alpine Research*, 37(3):323–330, 2005.

A. Humbert, D. Steinhage, V. Helm, S. Hoerz, J. Berendt, E. Leipprand, J. Christmann, C. Plate, and R. Müller. On the link between surface and basal structures of the Jelbart Ice Shelf, Antarctica. *Journal of Glaciology*, 61(229):975–986, 2015. doi: 10.3189/2015JoG15J023.

N. E. Hurt. Mathematical methods in shape-from-shading: a review of recent results. *Acta Applicandae Mathematica*, 23(2):163–188, 1991. doi: 10.1007/BF00048804.

S. Jacobs. Observations of change in the Southern Ocean. *Philosophical Transactions of the Royal Society A: Mathematical, Physical and Engineering Sciences*, 364(1844):1657–1681, 2006.

S. Jacobs, H. Helmer, C. Doake, A. Jenkins, and R. Frolich. Melting of ice shelves and the mass balance of antarctica. *Journal of Glaciology*, 38(130):375–387, 1992. doi: 10.3198/1992JoG38-130-375-387.

S. Jacobs, C. Giulivi, P. Dutrieux, E. Rignot, F. Nitsche, and J. Mouginot. Getz ice shelf melting response to changes in ocean forcing. *Journal of Geophysical Research: Oceans*, 2013.

S. S. Jacobs. On the nature and significance of the Antarctic Slope Front. *Marine Chemistry*, 35(1):9–24, 1991.

S. S. Jacobs, A. Jenkins, C. F. Giulivi, and P. Dutrieux. Stronger ocean circulation and increased melting under Pine Island Glacier ice shelf. *Nature Geoscience*, 4 (8):519–523, 2011. doi: 10.1038/ngeo1188.

A. Jenkins and C. Doake. Ice-ocean interaction on Ronne Ice Shelf, Antarctica. *Journal of Geophysical Research: Oceans*, 96(C1):791–813, 1991. doi: 10.1029/90JC01952.

A. Jenkins, H. F. Corr, K. W. Nicholls, C. L. Stewart, and C. S. Doake. Interactions between ice and ocean observed with phase-sensitive radar near an antarctic ice-shelf grounding line. *Journal of Glaciology*, 52(178):325–346, 2006. doi: 10.3189/172756506781828502.

A. Jenkins, P. Dutrieux, S. S. Jacobs, S. D. McPhail, J. R. Perrett, A. T. Webb, and D. White. Observations beneath Pine Island Glacier in West Antarctica and implications for its retreat. *Nature Geoscience*, 3(7):468–472, 2010. doi: 10.1038/ngeo890.

R. Jones, I. Renfrew, A. Orr, B. Webber, D. Holland, and M. Lazzara. Evaluation of four global reanalysis products using in situ observations in the Amundsen Sea Embayment, Antarctica. *Journal of Geophysical Research: Atmospheres*, 121 (11):6240–6257, 2016.

I. Joughin, D. R. MacAyeal, and S. Tulaczyk. Basal shear stress of the Ross ice streams from control method inversions. *Journal of Geophysical Research: Solid Earth*, 109(B9), 2004. doi: 10.1029/2003JB002960. URL `http://dx.doi.org/10.1029/2003JB002960`.

I. Joughin, S. B. Das, M. A. King, B. E. Smith, I. M. Howat, and T. Moon. Seasonal speedup along the western flank of the Greenland Ice Sheet. *Science*, 320(5877): 781–783, 2008.

I. Joughin, B. E. Smith, and D. M. Holland. Sensitivity of 21st century sea level to ocean-induced thinning of Pine Island Glacier, Antarctica. *Geophysical Research Letters*, 37(20), 2010.

I. Joughin, R. B. Alley, and D. M. Holland. Ice-sheet response to oceanic forcing. *science*, 338(6111):1172–1176, 2012. doi: 10.1126/science.1226481.

I. Joughin, D. E. Shean, B. E. Smith, and P. Dutrieux. Grounding line variability and subglacial lake drainage on Pine Island Glacier, Antarctica. *Geophysical Research Letters*, 2016. doi: 10.1002/2016GL070259.

J. Kämpf. Cascading-driven upwelling in submarine canyons at high latitudes. *Journal of Geophysical Research: Oceans (1978–2012)*, 110(C2), 2005.

A. B. Kara, A. J. Wallcraft, E. J. Metzger, H. E. Hurlburt, and C. W. Fairall. Wind stress drag coefficient over the global ocean. *Journal of Climate*, 20(23):5856–5864, 2007. doi: 10.1175/2007JCLI1825.1.

W. S. Kessler. Mean three-dimensional circulation in the northeast tropical Pacific. *Journal of Physical Oceanography*, 32(9):2457–2471, 2002.

A. Khazendar and A. Jenkins. A model of marine ice formation within Antarctic ice shelf rifts. *Journal of Geophysical Research: Oceans*, 108(C7), 2003.

A. Khazendar, M. Schodlok, I. Fenty, S. Ligtenberg, E. Rignot, and M. Van den Broeke. Observed thinning of Totten Glacier is linked to coastal polynya variability. *Nature Communications*, 4, 2013. doi: 10.1038/ncomms3857.

T. Kim, H. Ha, A. Wåhlin, S. Lee, C. Kim, J. Lee, and Y. Cho. Is Ekman pumping responsible for the seasonal variation of warm circumpolar deep water in the Amundsen Sea? *Continental Shelf Research*, 132:38–48, 2017.

J. Kingslake, J. C. Ely, I. Das, and R. E. Bell. Widespread movement of meltwater onto and across Antarctic ice shelves. *Nature*, 544(7650):349–352, 2017.

J. Klinck and M. Dinniman. Exchange across the shelf break at high southern latitudes. *Ocean Science*, 6:513–524.

W. B. Krabill. IceBridge ATM L1B Elevation and Return Strength, 2010, updated 2016. URL `http://dx.doi.org/10.5067/19SIM5TXKPGT`.

J. Krug, G. Durand, O. Gagliardini, and J. Weiss. Modelling the impact of submarine frontal melting and ice mélange on glacier dynamics. *The Cryosphere*, 9: 989–1003, 2015.

P. Kuipers Munneke, C. H. Reijmer, M. R. van den Broeke, G. König-Langlo, P. Stammes, and W. H. Knap. Analysis of clear-sky antarctic snow albedo using observations and radiative transfer modeling. *Journal of Geophysical Research: Atmospheres*, 113(D17), 2008. doi: 10.1029/2007JD009653.

J. H. Lambert. *Photometrie: Photometria, sive De mensura et gradibus luminis, colorum et umbrae*, volume 31. W. Engelmann, 1760.

K. Langley, A. Deschwanden, J. Kohler, A. Sinisalo, K. Matsuoka, T. Hattermann, A. Humbert, O. Nøst, and E. Isaksson. Complex network of channels beneath an Antarctic ice shelf. *Geophysical Research Letters*, 41(4):1209–1215, 2014. doi: 10.1002/2013GL058947.

A. M. Le Brocq, N. Ross, J. A. Griggs, R. G. Bingham, H. F. Corr, F. Ferraccioli, A. Jenkins, T. A. Jordan, A. J. Payne, D. M. Rippin, et al. Evidence from ice shelves for channelized meltwater flow beneath the Antarctic Ice Sheet. *Nature Geoscience*, 6(11):945–948, 2013. doi: 10.1038/ngeo1977.

J. T. M. Lenaerts, M. R. van den Broeke, W. J. van de Berg, E. van Meijgaard, and P. Kuipers Munneke. A new, high-resolution surface mass balance map of Antarctica (19792010) based on regional atmospheric climate modeling. *Geophysical Research Letters*, 39(4), 2012. ISSN 1944-8007. doi: 10.1029/2011GL050713. L04501.

E. Lewis and R. Perkin. Ice pumps and their rates. *J. Geophys. Res*, 91(11):756–11, 1986. doi: 10.1029/JC091iC10p11756.

X. Li, E. Rignot, M. Morlighem, J. Mouginot, and B. Scheuchl. Grounding line retreat of Totten Glacier, East Antarctica, 1996 to 2013. *Geophysical Research Letters*, 42(19):8049–8056, 2015. ISSN 1944-8007. doi: 10.1002/2015GL065701.

X. Li, E. Rignot, J. Mouginot, and B. Scheuchl. Ice flow dynamics and mass loss of Totten Glacier, East Antarctica, from 1989 to 2015. *Geophysical Research Letters*, 43(12):6366–6373, 2016. ISSN 1944-8007. doi: 10.1002/2016GL069173. URL `http://dx.doi.org/10.1002/2016GL069173`.

S. Ligtenberg, M. Heilsen, and M. van de Broeke. An improved semi-empirical model for the densification of Antarctic firn. *The Cryosphere*, 5(4):809–819, 2011. doi: 10.5194/tc-5-809-2011.

C. M. Little, A. Gnanadesikan, and M. Oppenheimer. How ice shelf morphology controls basal melting. *Journal of Geophysical Research: Oceans*, 114(C12), 2009. doi: 10.1029/2008JC005197.

H. Liu. Derivation of surface topography and terrain parameters from single satellite image using shape-from-shading technique. *Computers & geosciences*, 29(10): 1229–1239, 2003. doi: 10.1016/S0098-3004(03)00138-9.

H. Liu and K. Miller. Fracture toughness of fresh-water ice. *Journal of glaciology*, 22(86):135–143, 1979.

H. Liu, B. L. K. Jezek, and Z. Zhao;. Radarsat Antarctic Mapping Project Digital Elevation Model Version 2, 2001. URL `http://dx.doi.org/10.5067/PXKC81A7WAXD`.

L. Logan, G. Catania, L. Lavier, and E. Choi. A novel method for predicting fracture in floating ice. *Journal of Glaciology*, 59(216):750–758, 2013. doi: 10.3189/2013JoG12J210.

C. Lüpkes and G. Birnbaum. Surface drag in the arctic marginal sea-ice zone: a comparison of different parameterisation concepts. *Boundary-Layer Meteorology*, 117(2):179–211, 2005. doi: 10.1007/s10546-005-1445-8.

K. D. Mankoff, S. S. Jacobs, S. M. Tulaczyk, and S. E. Stammerjohn. The role of pine island glacier ice shelf basal channels in deep-water upwelling, polynyas and ocean circulation in pine island bay, antarctica. *Annals of Glaciology*, 53 (60):123–128, 2012. doi: 10.3189/2012AoG60A062.

O. J. Marsh, H. A. Fricker, M. R. Siegfried, K. Christianson, K. W. Nicholls, H. F. Corr, and G. Catania. High basal melting forming a channel at the grounding line of Ross Ice Shelf, Antarctica. *Geophysical Research Letters*, 2015. doi: 10.1002/2015GL066612.

G. J. Marshall. Trends in the Southern Annular Mode from observations and reanalyses. *Journal of Climate*, 16(24):4134–4143, 2003.

G. J. Marshall. Half-century seasonal relationships between the Southern Annular mode and Antarctic temperatures. *International Journal of Climatology*, 27(3): 373–383, 2007.

B. Marzeion and A. Levermann. Loss of cultural world heritage and currently inhabited places to sea-level rise. *Environmental Research Letters*, 9(3):034001, 2014.

R. Massom, P. Harris, K. J. Michael, and M. Potter. The distribution and formative processes of latent-heat polynyas in East Antarctica. *Annals of Glaciology*, 27 (1):420–426, 1998.

R. A. Massom, A. B. Giles, H. A. Fricker, R. C. Warner, B. Legrésy, G. Hyland, N. Young, and A. D. Fraser. Examining the interaction between multi-year landfast sea ice and the Mertz Glacier Tongue, East Antarctica: Another factor in ice sheet stability? *Journal of Geophysical Research: Oceans*, 115(C12), 2010.

R. A. Massom, A. B. Giles, R. C. Warner, H. A. Fricker, B. Legrésy, G. Hyland, L. Lescarmontier, and N. Young. External influences on the Mertz Glacier Tongue (East Antarctica) in the decade leading up to its calving in 2010. *Journal of Geophysical Research: Earth Surface*, 120(3):490–506, 2015.

P. Mathiot, H. Goosse, T. Fichefet, B. Barnier, and H. Gallée. Modelling the seasonal variability of the Antarctic Slope Current. *Ocean Science*, 7(4):445–532, 2011.

C. F. Maule, M. E. Purucker, N. Olsen, and K. Mosegaard. Heat flux anomalies in Antarctica revealed by satellite magnetic data. *Science*, 309(5733):464–467, 2005.

T. J. McDougall and P. M. Barker. Getting started with TEOS-10 and the Gibbs Seawater (GSW) oceanographic toolbox. *SCOR/IAPSO WG*, 127:1–28, 2011.

D. McGrath, K. Steffen, H. Rajaram, T. Scambos, W. Abdalati, and E. Rignot. Basal crevasses on the larsen c ice shelf, antarctica: Implications for meltwater ponding and hydrofracture. *Geophysical Research Letters*, 39(16), 2012a. doi: 10.1029/2012GL052413.

D. McGrath, K. Steffen, T. Scambos, H. Rajaram, G. Casassa, and J. L. Rodriguez Lagos. Basal crevasses and associated surface crevassing on the larsen c ice shelf, antarctica, and their role in ice-shelf instability. *Annals of Glaciology*, 53(60):10–18, 2012b. doi: 10.3189/2012AoG60A005.

C. McLandress, T. G. Shepherd, J. F. Scinocca, D. A. Plummer, M. Sigmond, A. I. Jonsson, and M. C. Reader. Separating the dynamical effects of climate change and ozone depletion. Part II: Southern Hemisphere troposphere. *Journal of Climate*, 24(6):1850–1868, 2011.

D. Menemenlis, J.-M. Campin, P. Heimbach, C. Hill, T. Lee, A. Nguyen, M. Schodlok, and H. Zhang. ECCO2: High resolution global ocean and sea ice data synthesis. *Mercator Ocean Quarterly Newsletter*, 31:13–21, 2008.

V. M. Merwade, D. R. Maidment, and B. R. Hodges. Geospatial representation of river channels. *Journal of Hydrologic Engineering*, 10(3):243–251, 2005. doi: 10.1061/(ASCE)1084-0699(2005)10:3(243).

A. Messerli and A. Grinsted. Image georectification and feature tracking toolbox: ImGRAFT. *Geoscientific Instrumentation, Methods and Data Systems*, 4(1): 23, 2015. doi: 10.5194/gi-4-23-2015. URL `http://dx.doi.org/10.5194/gi-4-23-2015`.

B. W. Miles, C. R. Stokes, and S. S. Jamieson. Pan-ice-sheet glacier terminus change in East Antarctica reveals sensitivity of Wilkes Land to sea-ice changes. *Science Advances*, 2(5):e1501350, 2016. doi: 10.1126/sciadv.1501350.

B. W. Miles, C. R. Stokes, and S. S. Jamieson. Simultaneous disintegration of outlet glaciers in Porpoise Bay (Wilkes Land), East Antarctica, driven by sea ice break-up. *The Cryosphere.*, 11:427–442, 2017.

T. Millgate, P. R. Holland, A. Jenkins, and H. L. Johnson. The effect of basal channels on oceanic ice-shelf melting. *Journal of Geophysical Research: Oceans*, 118(12):6951–6964, 2013. ISSN 2169-9291. doi: 10.1002/2013JC009402.

T. Moon, I. Joughin, B. Smith, M. R. Broeke, W. J. Berg, B. Noël, and M. Usher. Distinct patterns of seasonal Greenland glacier velocity. *Geophysical research letters*, 41(20):7209–7216, 2014.

R. J. Motyka, M. Truffer, M. Fahnestock, J. Mortensen, S. Rysgaard, and I. Howat. Submarine melting of the 1985 Jakobshavn Isbræ floating tongue and the triggering of the current retreat. *Journal of Geophysical Research: Earth Surface*, 116 (F1), 2011. doi: 10.1029/2009JF001405.

J. Mouginot, B. Scheuchl, and E. Rignot. MEaSUREs Antarctic Boundaries for IPY 2007-2009 from Satellite Radar, Version 1. *NASA National Snow and Ice Data Center Distributed Active Archive Center*, 2016. doi: 10.5067/AXE4121732AD.

J. Mouginot, E. Rignot, B. Scheuchl, and R. Millan. Comprehensive Annual Ice Sheet Velocity Mapping Using Landsat-8, Sentinel-1, and RADARSAT-2 Data. *Remote Sensing*, 9(4):364, 2017a.

J. Mouginot, B. Scheuchl, and E. Rignot. MEaSUREs Annual Antarctic Ice Velocity Maps 2005-2016, Version 1, 2017b.

A. Mousivand, W. Verhoef, M. Menenti, and B. Gorte. Modeling top of atmosphere radiance over heterogeneous non-Lambertian rugged terrain. *Remote Sensing*, 7 (6):8019–8044, 2015. doi: 10.3390/rs70608019.

A. Münchow, L. Padman, and H. A. Fricker. Interannual changes of the floating ice shelf of Petermann Gletscher, North Greenland, from 2000 to 2012. *Journal of Glaciology*, 60(221):489–499, 2014. doi: 10.3189/2014JoG13J135.

P. K. Munneke, S. R. Ligtenberg, M. R. Van Den Broeke, and D. G. Vaughan. Firn air depletion as a precursor of Antarctic ice-shelf collapse. *Journal of Glaciology*, 60(220):205–214, 2014.

A. Muñoz Martín, M. Catalán Morollón, J. Martín Dávila, and A. Carbó Gorosabel. Upper crustal structure of Deception Island area (Bransfield Strait, Antarctica) from gravity and magnetic modelling. *Antarctic Science*, 17(2):213–224, 2005.

C. Neal. The dynamics of the Ross Ice Shelf revealed by radio echo-sounding. *Journal of Glaciology*, 24(90):295–307, 1979.

F. O. Nitsche, D. Porter, G. Williams, E. A. Cougnon, A. D. Fraser, R. Correia, and R. Guerrero. Bathymetric control of warm ocean water access along the East Antarctic Margin. *Geophysical Research Letters*, 2017. ISSN 1944-8007. doi: 10.1002/2017GL074433.

I. Núñez-Riboni and E. Fahrbach. Seasonal variability of the Antarctic Coastal Current and its driving mechanisms in the Weddell Sea. *Deep Sea Research Part I: Oceanographic Research Papers*, 56(11):1927–1941, 2009.

H. Oerter, J. Kipfstuhl, J. Determann, H. Miller, D. Wagenbach, A. Minikin, and W. Graf. Evidence for basal marine ice in the filchner-ronne ice shelf. *Nature*, 358:399–401, 1992. doi: 10.1038/358399a0.

K. I. Ohshima, T. Takizawa, S. Ushio, and T. Kawamura. Seasonal variations of the Antarctic coastal ocean in the vicinity of Lützow-Holm Bay. *Journal of Geophysical Research: Oceans*, 101(C9):20617–20628, 1996. doi: 10.1029/96JC01752.

A. H. Orsi and T. Whitworth. WOCE Southern Ocean Atlas, 1998. URL `http://woceSOatlas.tamu.edu`.

A. H. Orsi, T. Whitworth, and W. D. Nowlin. On the meridional extent and fronts of the Antarctic Circumpolar Current. *Deep Sea Research Part I: Oceanographic Research Papers*, 42(5):641–673, 1995.

L. Padman, H. A. Fricker, R. Coleman, S. Howard, and L. Erofeeva. A new tide model for the Antarctic ice shelves and seas. *Annals of Glaciology*, 34(1):247–254, 2002. doi: 10.3189/172756402781817752.

L. Padman, M. King, D. Goring, H. Corr, and R. Coleman. Ice-shelf elevation changes due to atmospheric pressure variations. *Journal of Glaciology*, 49(167): 521–526, 2003. doi: 10.3189/172756503781830386.

L. Padman, D. P. Costa, M. S. Dinniman, H. A. Fricker, M. E. Goebel, L. A. Huckstadt, A. Humbert, I. Joughin, J. Lenaerts, S. R. Ligtenberg, et al. Oceanic controls on the mass balance of Wilkins Ice Shelf, Antarctica. *Journal of Geophysical Research: Oceans*, 117(C1), 2012. doi: 10.1029/2011JC007301.

S. Palmer, M. McMillan, and M. Morlighem. Subglacial lake drainage detected beneath the Greenland ice sheet. *Nature Communications*, 6, 2015. doi: 10.1038/ncomms9408.

F. S. Paolo, H. A. Fricker, and L. Padman. Volume loss from Antarctic ice shelves is accelerating. *Science*, 348(6232):327–331, 2015. doi: 10.1126/science.aaa0940.

F. S. Paolo, H. A. Fricker, and L. Padman. Constructing improved decadal records of Antarctic ice shelf height change from multiple satellite radar altimeters. *Remote Sensing of Environment*, 177:192–205, 2016. doi: 10.1016/j.rse.2016.01.026.

H. A. Phillips. Surface meltstreams on the Amery Ice Shelf, East Antarctica. *Annals of Glaciology*, 27(1):177–181, 1998. doi: 10.3198/1998AoG27-1-177-181.

G. Picard and M. Fily. Surface melting observations in Antarctica by microwave radiometers: Correcting 26-year time series from changes in acquisition hours. *Remote sensing of environment*, 104(3):325–336, 2006.

J. R. Potter and J. G. Paren. *Interaction Between Ice Shelf and Ocean in George VI Sound, Antarctica*, pages 35–58. American Geophysical Union, 2013. ISBN 9781118665206. doi: 10.1029/AR043p0035.

H. Pritchard, S. Ligtenberg, H. Fricker, D. Vaughan, M. Van den Broeke, and L. Padman. Antarctic ice-sheet loss driven by basal melting of ice shelves. *Nature*, 484(7395):502–505, 2012. doi: 10.1038/nature10968.

H. D. Pritchard, R. J. Arthern, D. G. Vaughan, and L. A. Edwards. Extensive dynamic thinning on the margins of the greenland and antarctic ice sheets. *Nature*, 461(7266):971, 2009.

B. H. Raup, T. A. Scambos, and T. Haran. Topography of streaklines on an Antarctic ice shelf from photoclinometry applied to a single Advanced Land Imager (ALI) image. *IEEE transactions on geoscience and remote sensing*, 43(4):736–742, 2005. doi: 10.1109/TGRS.2005.843953.

W. Rees and J. Dowdeswell. Topographic effects on light scattering from snow. In *Geoscience and Remote Sensing Symposium, 1988. IGARSS'88. Remote Sensing: Moving Toward the 21st Century., International*, volume 1, pages 161–164. IEEE, 1988.

E. Rignot and S. S. Jacobs. Rapid bottom melting widespread near Antarctic ice sheet grounding lines. *Science*, 296(5575):2020–2023, 2002. doi: 10.1126/science.1070942. URL `http://dx.doi.org/10.1126/science.1070942`.

E. Rignot and K. Steffen. Channelized bottom melting and stability of floating ice shelves. *Geophysical Research Letters*, 35(2), 2008. doi: 10.1029/2007GL031765.

E. Rignot, J. Mouginot, and B. Scheuchl. Antarctic grounding line mapping from differential satellite radar interferometry. *Geophys. Res. Lett.*, 38(10), may 2011a. doi: 10.1029/2011gl047109.

E. Rignot, J. Mouginot, and B. Scheuchl. Ice flow of the Antarctic ice sheet. *Science*, 333(6048):1427–1430, 2011b. doi: 10.1126/science.1208336.

E. Rignot, J. Mouginot, and B. Scheuchl. MEaSUREs InSAR-Based Antarctica Ice Velocity Map. 2011c. doi: 10.5067/MEASURES/CRYOSPHERE/nsidc-0484.001. URL `http://dx.doi.org/10.5067/MEASURES/CRYOSPHERE/nsidc-0484.001`.

E. Rignot, J. Mouginot, and B. Scheuchl. MEaSUREs Antarctic Grounding Line from Differential Satellite Radar Interferometry, 2011d. URL `http://nsidc.org/data/nsidc-0498.html`.

E. Rignot, S. Jacobs, J. Mouginot, and B. Scheuchl. Ice-shelf melting around Antarctica. *Science*, 341(6143):266–270, 2013. doi: 10.1126/science.1235798.

E. Rignot, J. Mouginot, and B. Scheuchl. MEaSUREs InSAR-Based Antarctica Ice Velocity Map, Version 2, 2017.

S. R. Rintoul, A. Silvano, B. Pena-Molino, E. van Wijk, M. Rosenberg, J. S. Greenbaum, and D. D. Blankenship. Ocean heat drives rapid basal melt of the Totten Ice Shelf. *Science Advances*, 2(12):e1601610, 2016.

A. A. Robel. Thinning sea ice weakens buttressing force of iceberg mélange and promotes calving. *Nature Communications*, 8, 2017.

J. Roberts, B. K. Galton-Fenzi, F. S. Paolo, C. Donnelly, D. E. Gwyther, L. Padman, D. Young, R. Warner, J. Greenbaum, H. A. Fricker, et al. Ocean forced variability of Totten Glacier mass loss. *Geological Society, London, Special Publications*, 461:SP461–6, 2017.

T. Scambos, J. Bohlander, and B. Raup. Images of Antarctic Ice Shelves, MODIS channel 2. National Snow and Ice Data Center, 2001, updated 2017.

T. Scambos, T. Haran, M. Fahnestock, T. Painter, and J. Bohlander. MODIS-based Mosaic of Antarctica (MOA) data sets Continent-wide surface morphology and snow grain size. *Remote Sensing of Environment*, 111(2):242–257, 2007. doi: 10.1016/j.rse.2006.12.020.

T. Scambos, H. A. Fricker, C.-C. Liu, J. Bohlander, J. Fastook, A. Sargent, R. Massom, and A.-M. Wu. Ice shelf disintegration by plate bending and hydro-fracture: Satellite observations and model results of the 2008 Wilkins ice shelf break-ups. *Earth and Planetary Science Letters*, 280(1):51–60, 2009.

T. Scambos, M. Fahnestock, A. Gardner, and M. Klinger. Global Land Ice Velocity Extraction from Landsat 8 (GoLIVE), Version 1.1, 2016.

T. A. Scambos and M. A. Fahnestock. Improving digital elevation models over ice sheets using AVHRR-based photoclinometry. *Journal of Glaciology*, 44(146): 97–103, 1998. doi: 10.3198/1998JoG44-146-97-103.

T. A. Scambos and T. Haran. An image-enhanced DEM of the Greenland Ice Sheet. *Annals of Glaciology*, 34(1):291–298, 2002. doi: 10.3189/172756402781817969.

T. A. Scambos, J. Bohlander, C. u. Shuman, and P. Skvarca. Glacier acceleration and thinning after ice shelf collapse in the Larsen B embayment, Antarctica. *Geophysical Research Letters*, 31(18), 2004.

SCAR Secretariat. Composite Gazetteer of Antarctica, 1992, updated 2015. URL `http://gcmd.nasa.gov/records/SCAR_Gazetteer.html`.

M. Scheinert, F. Ferraccioli, J. Schwabe, R. Bell, M. Studinger, D. Damaske, W. Jokat, N. Aleshkova, T. Jordan, G. Leitchenkov, et al. New Antarctic gravity anomaly grid for enhanced geodetic and geophysical studies in Antarctica. *Geophysical Research Letters*, 2016.

C. Schoof. Ice sheet grounding line dynamics: Steady states, stability, and hysteresis. *Journal of Geophysical Research: Earth Surface*, 112(F3), 2007.

C. Schoof. Ice-sheet acceleration driven by melt supply variability. *Nature*, 468 (7325):803, 2010.

W. Schwanghart and D. Scherler. Short Communication: TopoToolbox 2-MATLAB-based software for topographic analysis and modeling in Earth surface sciences. *Earth Surface Dynamics*, 2(1):1, 2014. doi: 10.5194/esurf-2-1-2014.

O. Sergienko. Basal channels on ice shelves. *Journal of Geophysical Research: Earth Surface*, 118(3):1342–1355, 2013. doi: 10.1002/jgrf.20105.

O. Sergienko, D. MacAyeal, and R. Bindschadler. Causes of sudden, short-term changes in ice-stream surface elevation. *Geophysical Research Letters*, 34(22), 2007. doi: 10.1029/2007GL031775.

A. F. Shchepetkin and J. C. McWilliams. The regional oceanic modeling system (ROMS): a split-explicit, free-surface, topography-following-coordinate oceanic model. *Ocean Modelling*, 9(4):347–404, 2005.

D. E. Shean, O. Alexandrov, Z. M. Moratto, B. E. Smith, I. R. Joughin, C. Porter, and P. Morin. An automated, open-source pipeline for mass production of digital elevation models (DEMs) from very-high-resolution commercial stereo satellite imagery. *ISPRS Journal of Photogrammetry and Remote Sensing*, 116:101–117, 2016. doi: 10.1016/j.isprsjprs.2016.03.012.

C. Shuman, H. Zwally, B. Schutz, A. Brenner, J. DiMarzio, V. Suchdeo, and H. Fricker. ICESat Antarctic elevation data: Preliminary precision and accuracy assessment. *Geophysical Research Letters*, 33(7), 2006.

M. Sigmond, M. C. Reader, J. C. Fyfe, and N. P. Gillett. Drivers of past and future Southern Ocean change: Stratospheric ozone versus greenhouse gas impacts. *Geophysical Research Letters*, 38(12):n/a–n/a, 2011. ISSN 1944-8007. doi: 10.1029/2011GL047120. URL `http://dx.doi.org/10.1029/2011GL047120`. L12601.

A. Silvano, S. R. Rintoul, and L. Herraiz-Borreguero. Ocean-ice shelf interaction in East Antarctica. *Oceanography*, 29(4):130–143, 2016. doi: 10.5670/oceanog.2016.105.

A. Silvano, S. R. Rintoul, B. Peña-Molino, and G. D. Williams. Distribution of water masses and meltwater on the continental shelf near the Totten and Moscow University ice shelves. *Journal of Geophysical Research: Oceans*, (3):2050–2068, 2017. ISSN 2169-9291. doi: 10.1002/2016JC012115. URL `http://dx.doi.org/10.1002/2016JC012115`.

B. Smith, I. Joughin, and S. Tulaczyk;. Antarctic active subglacial lake inventory from icesat altimetry, 2012. URL `http://dx.doi.org/10.7265/N57M05WS`.

B. E. Smith, H. A. Fricker, I. R. Joughin, and S. Tulaczyk. An inventory of active subglacial lakes in Antarctica detected by ICESat (2003–2008). *Journal of Glaciology*, 55(192):573–595, 2009. doi: 10.3189/002214309789470879.

B. E. Smith, N. Gourmelen, A. Huth, and I. Joughin. Connected subglacial lake drainage beneath Thwaites Glacier, West Antarctica. *The Cryosphere*, 11(1): 451–467, 2017. doi: 10.5194/tc-11-451-2017.

J. P. Snyder. *Map projections–A working manual*, volume 1395. US Government Printing Office, 1987.

H.-G. Sohn, K. C. Jezek, and C. J. van der Veen. Jakobshavn glacier, west greenland: 30 years of spaceborne observations. *Geophysical Research Letters*, 25 (14):2699–2702, 1998.

P. Spence, S. M. Griffies, M. H. England, A. M. Hogg, O. A. Saenko, and N. C. Jourdain. Rapid subsurface warming and circulation changes of Antarctic coastal waters by poleward shifting winds. *Geophysical Research Letters*, 41(13):4601–4610, 2014. ISSN 1944-8007. doi: 10.1002/2014GL060613. URL `http://dx.doi.org/10.1002/2014GL060613`.

V. B. Spikes, B. M. Csathó, and I. M. Whillans. Laser profiling over Antarctic ice streams: methods and accuracy. *Journal of Glaciology*, 49(165):315–322, 2003.

P. St-Laurent, J. M. Klinck, and M. S. Dinniman. On the Role of Coastal Troughs in the Circulation of Warm Circumpolar Deep Water on Antarctic Shelves. *Journal of Physical Oceanography*, 43(1):51–64, 2013.

T. Stanton, W. Shaw, M. Truffer, H. Corr, L. Peters, K. Riverman, R. Bindschadler, D. Holland, and S. Anandakrishnan. Channelized ice melting in the ocean boundary layer beneath Pine Island Glacier, Antarctica. *Science*, 341(6151):1236–1239, 2013. doi: 10.1126/science.1239373.

L. A. Stearns, B. E. Smith, and G. S. Hamilton. Increased flow speed on a large East Antarctic outlet glacier caused by subglacial floods. *Nature Geoscience*, 1 (12):827–831, 2008. doi: 10.1038/ngeo356.

K. Steffen. Bidirectional reflectance of snow at 500–600 nm. *International Association of Hydrological Sciences–IAHS Publication*, 166:415–425, 1987.

E. Steig, Q. Ding, D. Battisti, and A. Jenkins. Tropical forcing of Circumpolar Deep Water inflow and outlet glacier thinning in the Amundsen Sea Embayment, West Antarctica. *Annals of Glaciology*, 53(60):19, 2012.

T. Stocker, D. Qin, and G. Platner. Climate Change 2013: The Physical Science Basis. *Working Group I Contribution to the Fifth Assessment Report of the Intergovernmental Panel on Climate Change. Summary for Policymakers (IPCC, 2013)*, 2013.

T. Tamura, K. I. Ohshima, A. D. Fraser, and G. D. Williams. Sea ice production variability in Antarctic coastal polynyas. *Journal of Geophysical Research: Oceans*, 121(5):2967–2979, 2016.

J. Taylor. *An Introduction to Error Analysis: The Study of Uncertainties in Physical Measurements*. University Science Books, Sausalito, CA, second edition, 1997.

M. Thoma, A. Jenkins, D. Holland, and S. Jacobs. Modelling circumpolar deep water intrusions on the Amundsen Sea continental shelf, Antarctica. *Geophysical Research Letters*, 35(18), 2008. doi: 10.1029/2008GL034939.

D. W. Thompson, J. M. Wallace, and G. C. Hegerl. Annular modes in the extratropical circulation. Part II: Trends. *Journal of Climate*, 13(5):1018–1036, 2000.

D. W. Thompson, S. Solomon, P. J. Kushner, M. H. England, K. M. Grise, and D. J. Karoly. Signatures of the Antarctic ozone hole in Southern Hemisphere surface climate change. *Nature Geoscience*, 4(11):741, 2011.

T. Thorsteinsson, C. F. Raymond, G. H. Gudmundsson, R. A. Bindschadler, P. Vornberger, and I. Joughin. Bed topography and lubrication inferred from surface measurements on fast-flowing ice streams. *Journal of Glaciology*, 49(167):481–490, 2003.

K. M. Thyng, C. A. Greene, R. D. Hetland, H. M. Zimmerle, and S. F. DiMarco. True colors of oceanography: Guidelines for effective and accurate colormap selection. *Oceanography*, 29, September 2016. doi: 10.5670/oceanog.2016.66.

R. Timmermann and H. H. Hellmer. Southern Ocean warming and increased ice shelf basal melting in the twenty-first and twenty-second centuries based on coupled ice-ocean finite-element modelling. *Ocean Dynamics*, pages 1–16, 2013.

R. Timmermann, A. Le Brocq, T. Deen, E. Domack, P. Dutrieux, B. Galton-Fenzi, H. Hellmer, A. Humbert, D. Jansen, A. Jenkins, et al. A consistent data set of

Antarctic ice sheet topography, cavity geometry, and global bathymetry. *Earth System Science Data*, 2(2):261, 2010.

J. Todd and P. Christoffersen. Are seasonal calving dynamics forced by buttressing from ice mélange or undercutting by melting? Outcomes from full-Stokes simulations of Store Glacier, West Greenland. *The Cryosphere*, 8(6):2353–2365, 2014.

J. Van Diggelen. A Photometric Investigation of the Slopes and the Heights of the Ranges of Hills in the Maria of the Moon. *Bulletin of the Astronomical Institutes of the Netherlands*, 11:283, 1951.

D. Vaughan and C. Doake. Recent atmospheric warming and retreat of ice shelves on the Antarctic Peninsula. *Nature*, 379(6563):328, 1996.

D. G. Vaughan. Tidal flexure at ice shelf margins. *Journal of Geophysical Research: Solid Earth*, 100(B4):6213–6224, 1995. doi: 10.1029/94JB02467.

D. G. Vaughan, H. F. Corr, R. A. Bindschadler, P. Dutrieux, G. H. Gudmundsson, A. Jenkins, T. Newman, P. Vornberger, and D. J. Wingham. Subglacial melt channels and fracture in the floating part of Pine Island Glacier, Antarctica. *Journal of Geophysical Research: Earth Surface*, 117(F3), 2012. doi: 10.1029/2012JF002360.

A. Wåhlin, X. Yuan, G. Björk, and C. Nohr. Inflow of Warm Circumpolar Deep Water in the Central Amundsen Shelf. *Journal of Physical Oceanography*, 40 (6):1427–1434, 2010. doi: 10.1175/2010JPO4431.1.

A. Wåhlin, O. Kalén, L. Arneborg, G. Björk, G. Carvajal, H. K. Ha, T. Kim, S. H. Lee, J. Lee, and C. Stranne. Variability of warm deep water inflow in a submarine trough on the Amundsen Sea shelf. *Journal of Physical Oceanography*, 43(10): 2054–2070, 2013. doi: 10.1175/JPO-D-12-0157.1. URL `http://dx.doi.org/10.1175/JPO-D-12-0157.1`.

M. Wakatsuchi, K. I. Ohshima, M. Hishida, and M. Naganobu. Observations of a street of cyclonic eddies in the Indian Ocean sector of the Antarctic Divergence. *Journal of Geophysical Research: Oceans*, 99(C10):20417–20426, 1994. doi: 10.1029/94JC01478. URL `http://dx.doi.org/10.1029/94JC01478`.

R. T. Walker, T. K. Dupont, D. M. Holland, B. R. Parizek, and R. B. Alley. Initial effects of oceanic warming on a coupled ocean–ice shelf–ice stream system. *Earth and Planetary Science Letters*, 287(3):483–487, 2009.

J. I. Walter, J. E. Box, S. Tulaczyk, E. E. Brodsky, I. M. Howat, Y. Ahn, and A. Brown. Oceanic mechanical forcing of a marine-terminating Greenland glacier. *Annals of Glaciology*, 53(60):181–192, 2012.

Q. Wang, S. Danilov, E. Fahrbach, J. Schröter, and T. Jung. On the impact of wind forcing on the seasonal variability of Weddell Sea Bottom Water transport. *Geophysical Research Letters*, 39(6), 2012.

Z. Wang. On the response of southern hemisphere subpolar gyres to climate change in coupled climate models. *Journal of Geophysical Research: Oceans*, 118(3): 1070–1086, 2013. doi: 10.1002/jgrc.20111. URL `http://dx.doi.org/10.1002/jgrc.20111`.

S. G. Warren. Optical properties of snow. *Reviews of Geophysics*, 20(1):67–89, 1982. doi: 10.1029/RG020i001p00067.

B. G. Webber, K. J. Heywood, D. P. Stevens, P. Dutrieux, E. P. Abrahamsen, A. Jenkins, S. S. Jacobs, H. K. Ha, S. H. Lee, and T. W. Kim. Mechanisms driving variability in the ocean forcing of Pine Island Glacier. *Nature Communications*, 8, 2017. doi: 10.1038/ncomms14507. URL `http://dx.doi.org/10.1038/ncomms14507`.

J. Weertman. Stability of the junction of an ice sheet and an ice shelf. *Journal of Glaciology*, 13(67):3–11, 1974. doi: 10.3198/1974JoG13-67-3-11.

P. Wessel and W. H. Smith. Free software helps map and display data. *Eos, Transactions American Geophysical Union*, 72(41):441–446, 1991.

P. Wessel, W. H. Smith, R. Scharroo, J. Luis, and F. Wobbe. Generic Mapping Tools: Improved version released. *Eos, Transactions American Geophysical Union*, 94(45):409–410, 2013.

R. L. Wildey. Generalized photoclinometry for Mariner 9. *Icarus*, 25(4):613–626, 1975.

G. Williams, A. Meijers, A. Poole, P. Mathiot, T. Tamura, and A. Klocker. Late winter oceanography off the Sabrina and BANZARE coast (117–128 E), East Antarctica. *Deep Sea Research Part II: Topical Studies in Oceanography*, 58 (9):1194–1210, 2011. doi: 10.1016/j.dsr2.2010.10.035. URL `http://dx.doi.org/10.1016/j.dsr2.2010.10.035`.

W. Williams, E. Carmack, and R. Ingram. Physical oceanography of polynyas. *Elsevier Oceanography Series*, 74:55–85, 2007.

M. J. Willis, B. G. Herried, M. G. Bevis, and R. E. Bell. Recharge of a subglacial lake by surface meltwater in northeast Greenland. *Nature*, 518(7538):223–227, 2015. doi: 10.1038/nature14116.

C. J. Wilson, P. S. Wilson, C. A. Greene, and K. H. Dunton. Seagrass leaves in 3-D: Using computed tomography and low-frequency acoustics to investigate the material properties of seagrass tissue. *Journal of Experimental Marine Biology and Ecology*, 395(1):128–134, 2010.

C. J. Wilson, P. S. Wilson, C. A. Greene, and K. H. Dunton. Seagrass meadows provide an acoustic refuge for estuarine fish. *Marine Ecology Progress Series*, 472:117–127, 2013.

A. Wright and M. Siegert. A fourth inventory of Antarctic subglacial lakes. *Antarctic Science*, 24(06):659–664, 2012. doi: 10.1017/S095410201200048X.

D. A. Young, A. P. Wright, J. L. Roberts, R. C. Warner, N. W. Young, J. S. Greenbaum, D. M. Schroeder, J. W. Holt, D. E. Sugden, D. D. Blankenship, et al. A dynamic early East Antarctic Ice Sheet suggested by ice-covered fjord landscapes. *Nature*, 474(7349):72–75, 2011. doi: 10.1038/nature10114.

D. A. Young, L. E. Lindzey, D. D. Blankenship, J. S. Greenbaum, A. Garcia De Gorordo, S. D. Kempf, J. L. Roberts, R. C. Warner, T. Van Ommen, M. J. Siegert, et al. Land-ice elevation changes from photon-counting swath altimetry: first applications over the Antarctic ice sheet. *Journal of Glaciology*, 61(225): 17–28, 2015. doi: 10.3189/2015JoG14J048.

H. J. Zwally, M. B. Giovinetto, M. A. Beckley, and J. L. Saba. Antarctic and Greenland Drainage Systems. URL `http://icesat4.gsfc.nasa.gov/cryo_data/ant_grn_drainage_systems.php`.

H. J. Zwally, W. Abdalati, T. Herring, K. Larson, J. Saba, and K. Steffen. Surface melt-induced acceleration of Greenland ice-sheet flow. *Science*, 297(5579):218–222, 2002.

H. J. Zwally, R. Schutz, D. Hancock, and J. Dimarzio. GLAS/ICESat L2 Antarctic and Greenland Ice Sheet Altimetry Data (HDF5), Version 34. GLAH12, 2014.

Vita

Chad Allen Greene spent his youth roaming the forests and fields of central Virginia, United States. He attended Virginia Commonwealth University, where he received a Bachelor of Science degree in Mechanical Engineering with a minor in Mathematics in 2007. His research career began in the field of underwater acoustics, where he investigated the acoustic properties of methane hydrates (Greene, 2010; Greene and Wilson, 2012) and the acoustic environments of dolphin habitats in the Gulf of Mexico (Wilson et al., 2010, 2013). Chad received a Master of Science degree in Mechanical Engineering from the University of Texas at Austin in 2010. While conducting research for this dissertation, Chad performed field work in Marie Byrd Land, West Antarctica, and taught undergraduate courses in climate science and geology in the Department of Geological Sciences at the University of Texas at Austin.

Permanent address: 814 Keasbey St.
Austin, Texas 78751

This dissertation was typeset with LaTeX[†] by the author.

[†] LaTeX is a document preparation system developed by Leslie Lamport as a special version of Donald Knuth's TeX Program.